

UC Irvine

UC Irvine Electronic Theses and Dissertations

Title

Understanding the Mechanisms of Salt Formation in New Particle Formation and Growth

Permalink

<https://escholarship.org/uc/item/0ws7419z>

Author

Chee, Sabrina

Publication Date

2021

Copyright Information

This work is made available under the terms of a Creative Commons Attribution License, available at <https://creativecommons.org/licenses/by/4.0/>

Peer reviewed|Thesis/dissertation

UNIVERSITY OF CALIFORNIA,
IRVINE

Understanding the Mechanisms of Salt Formation in New Particle Formation and Growth

DISSERTATION

submitted in partial satisfaction of the requirements
for the degree of

DOCTOR OF PHILOSOPHY

in Chemistry

by

Sabrina Chee

Dissertation Committee:
Professor James N. Smith, Chair
Professor Barbara Finlayson-Pitts
Professor Sergey Nizkorodov

2021

Chapter 2 © 2018 Taylor & Francis
Chapter 3 © 2019 American Chemical Society
All other materials © 2021 Sabrina Chee

DEDICATION

To my mom
words cannot express how you have shaped my life

To my family
you give me a home so that I can move forward

“Time that you enjoyed wasting, was not wasted.”

- John Lennon

“Find your strength in love”

- Whitney Houston

TABLE OF CONTENTS

	Page
LIST OF FIGURES	vi
LIST OF TABLES	ix
ACKNOWLEDGMENTS	x
CURRICULUM VITAE	xii
ABSTRACT OF THE DISSERTATION	xvii
1 Introduction	1
1.1 List of Research Articles	1
1.2 Background	2
1.2.1 Impact of Atmospheric Nanoparticles for Health and Climate	2
1.2.2 Known mechanisms of nanoparticle formation and growth	4
1.2.3 Acid-base reactions in the atmosphere	5
1.2.4 Lab studies of salt particle behavior	9
1.2.5 Measurement and Modeling Gap	12
1.3 Nanoparticle Production and Measurement Methods Used	12
1.3.1 Nucleation Flow Reactor	13
1.3.2 Spray Atomizer	15
1.3.3 Measurement Methods	16
1.3.4 Challenges Working with Salt Systems	20
1.3.5 Systems Measured	23
1.4 Dissertation Goals and Chapter Descriptions	23
2 Size Resolved Chemical Composition of Nanoparticles from Reactions of Sulfuric Acid with Ammonia and Dimethylamine	26
2.1 Abstract	26
2.2 Introduction	27
2.3 Experimental	29
2.3.1 Experimental Setup	29
2.3.2 Nanoparticle Composition Measurements	31
2.3.3 Model Description	33
2.4 Results and Discussion	34

2.4.1	Size Distributions of H ₂ SO ₄ -DMA and H ₂ SO ₄ -NH ₃ Nanoparticles . . .	34
2.4.2	Ions Detected by TDCIMS and Their Desorption Profiles	35
2.4.3	Acid:base Ratio H ₂ SO ₄ -NH ₃ and H ₂ SO ₄ -DMA Nanoparticles	37
2.4.4	Thermodynamic Modeling of H ₂ SO ₄ -NH ₃ and H ₂ SO ₄ -DMA Nanoparticles	42
2.5	Conclusions	44
3	An Experimental and Modeling Study of Nanoparticle Formation and Growth from Dimethylamine and Nitric Acid	46
3.1	Abstract	46
3.2	Introduction	47
3.3	Experimental and Theoretical Methods	49
3.3.1	Particle Generation	49
3.3.2	Nanoparticle Composition Measurements	51
3.3.3	Computational Methods	52
3.4	Results and Discussion	53
3.4.1	Size distributions of nanoparticles generated in dry or humid conditions	53
3.4.2	Desorption thermograms of HNO ₃ -DMA particles under dry and humid conditions	55
3.4.3	Size-resolved composition measurements	56
3.4.4	Cluster modelling	58
3.4.5	Comparison to sulfuric acid-dimethylamine system	62
3.5	Conclusions	64
4	A Predictive Model for Salt Nanoparticle Formation Using Heterodimer Stability Calculations	65
4.1	Abstract	65
4.2	Introduction	66
4.3	Computational methods	69
4.3.1	Cluster thermodynamics	70
4.3.2	Particle formation simulations	71
4.4	Results and discussion	72
4.4.1	Heterodimer stability results	72
4.4.2	Molecular properties that affect heterodimer stability ($\Delta G_{\text{heterodimer}}$) .	74
4.4.3	Heterodimer stability versus $J_{1.5}$	80
4.4.4	System-specific parameterization for weak bases using normalized heterodimer concentration (Φ)	87
4.5	Conclusions	89
5	Conclusions and Future Perspectives	92
5.1	Conclusions	92
5.2	Future Work	94
	Bibliography	96

Appendix A Chapter 2 Supporting Information	117
Appendix B Chapter 3 Supporting Information	120
Appendix C Chapter 4 Supporting Information	126

LIST OF FIGURES

	Page
1.1 Formation and removal pathways of atmospheric aerosol sorted by size, reproduced from Whitby (1978).	3
1.2 Residence times of particles according to size, as well as their main loss pathways, reproduced from Smith et al. (2004).	5
1.3 Relative contributions of compounds to nanoparticle growth as a function of size. Reproduced from Ehn et al. (2014).	6
1.4 Illustration of the measurement size ranges of state-of-the-art instruments. Instruments that are starred (**) measure physical properties of their size range, while other instruments can probe the composition of nanoparticles to some degree. Solid lines indicate size ranges that the instrument has measured in the field, while dotted lines indicate size ranges the instrument has measured in the lab. Figure reproduced from Paper VI	10
1.5 Schematic of the TI-CIMS inlet used in Paper II	19
1.6 Mass spectrum of particulate signal from size-selected dimethylammonium sulfate particles. Signals in red are contaminants from previous experiments that partitioned from within the TDCIMS inlet. All upstream tubing and surfaces had been cleaned, including UPCs and nDMAs.	21
2.1 Schematic of the flow tube reactor.	29
2.2 Size distributions of particles measured by SMPS from the reactions of (a) $2.5 * 10^{10} \text{ cm}^{-3} \text{ H}_2\text{SO}_4$ with $8.9 * 10^{10} \text{ cm}^{-3} \text{ DMA}$, and (b) $2.5 * 10^{10} \text{ cm}^{-3} \text{ H}_2\text{SO}_4$ with $1.3 * 10^{12} \text{ cm}^{-3} \text{ NH}_3$ under dry conditions and at 60% RH.	34
2.3 Typical desorption profiles of ions formed by heating H_2SO_4 -DMA (a, c) and H_2SO_4 - NH_3 (b, d) particles collected on the Pt filament. The top panels show ions collected in the negative ion mode. The lower panels show ions collected in the positive ion mode. The dashed lines show the evolution of the filament temperature.	36
2.4 Size resolved acid:base ratio of newly formed particles in the H_2SO_4 -DMA system under dry conditions and at 60% RH. The concentrations of H_2SO_4 and DMA introduced into the flow tube reactor were $2.5 * 10^{10} \text{ cm}^{-3}$ and $8.9 * 10^{10} \text{ cm}^{-3}$, respectively, for both the dry conditions and at 60% RH. The error bars represent standard deviations of at least three repeated measurements. The horizontal black line represents the acid:base ratio of fully neutralized H_2SO_4 -DMA particles.	38

2.5	Ratios of $\text{SO}_5^-:\text{SO}_3^-$ and $\text{HSO}_4^-:\text{SO}_3^-$ as a function of particle size for newly formed particles in the H_2SO_4 -DMA system under dry conditions. The concentrations of H_2SO_4 and DMA introduced into the flow reactor were $2.5 * 10^{10} \text{ cm}^{-3}$ and $8.9 * 10^{10} \text{ cm}^{-3}$, respectively. The error bars represent standard deviations of at least three repeated measurements. The horizontal black line represents a $\text{SO}_5^-:\text{SO}_3^-$ ratio of 0.44.	39
2.6	Size resolved acid:base ratio of newly formed particles formed in the H_2SO_4 - NH_3 system under dry conditions and at 60% RH. The concentrations of H_2SO_4 and NH_3 introduced into the flow tube reactor were $2.5 * 10^{10} \text{ cm}^{-3}$ and $1.3 * 10^{12} \text{ cm}^{-3}$, respectively, for both the dry conditions and 60% RH. The error bars represent standard deviations of at least three repeated measurements. The horizontal black line represents the acid:base ratio of fully neutralized H_2SO_4 - NH_3 particles.	40
3.1	Particle generation flow tube setup.	49
3.2	Size distribution of particles generated in dry (5% RH) and humid (55% RH) conditions.	54
3.3	Representative desorption profiles of (a) NO_3^- ion (m/z 62), $\text{HNO}_3(\text{NO}_3)$ ion (m/z 125), and (b) $(\text{CH}_3)_2\text{NH}_2^+$ ion (m/z 46). Wire current is a proxy for the temperature of the wire.	55
3.4	Size-resolved acid/base ratios of HNO_3 -DMA particles. Red triangles represent particles formed in dry conditions, while blue squares represent particles formed in humid conditions. The black line is to guide the eye to a neutral 1:1 acid/base ratio.	57
3.5	Clusters of (a) 1NA1D, (b) 2NA1D, (c) 1NA2D, and (d) 2NA2D. Color coding: carbon atoms are brown, oxygen atoms are red, nitrogen atoms are blue, and hydrogen atoms are gray. Dotted lines indicate hydrogen bonding between molecules.	58
3.6	Overall evaporation rates for clusters of 1-4 nitric acid and 1-4 dimethylamine molecules at 298.15 K. Cells are colored from purple (lowest evaporation rates) to yellow (highest evaporation rates).	60
3.7	Overall evaporation rates for clusters of 1-4 sulfuric acid and 1-4 dimethylamine molecules at 298.15 K. Cells are colored from purple (lowest evaporation rates) to yellow (highest evaporation rates).	62
3.8	Molecular structures of 1SA1D (left) and 2SA1D (right). Color coding: sulfur atoms are yellow, oxygen atoms are red, nitrogen atoms are blue, and hydrogen atoms are gray. Dotted lines indicate hydrogen bonding interactions.	63
4.1	Heterodimers of sa with amm, ma, dma, tma, tmao, gua, mea, put and pz, respectively.	73
4.2	Calculated GA vs literature $\text{p}K_a$ values from Haynes (2014).	74
4.3	Cyclic and acyclic configurations of protonated put. The lowest energy acyclic structure is 14.6 kcal/mol higher in free energy than the cyclic, global minimum structure.	75

4.4	Calculated ΔG_A and ΔpK_a plotted against $\Delta G_{\text{heterodimer}}$. Each data point represents an acid–base pair between either sa, na, or msa with either amm, ma, dma, tma, tmao, gua, mea, put, or pz. Blue text represent ΔG_A values, while red text represent ΔpK_a values. Text markers are centered over the data point.	76
4.5	ΔG_A and ΔpK_a values separated based on whether the heterodimer structure exhibits proton transfer. The grey dashed line on the ΔG_A graph at 103 kcal/mol shows the cutoff point for proton transfer.	77
4.6	Deprotonated (left) and protonated (right) conformers of pz for the na–pz salt showing the ring strain necessary to form another intermolecular hydrogen bond.	78
4.7	Base vapor pressure plotted against $\Delta G_{\text{heterodimer}}$ for sa, msa, and na salts.	80
4.8	Heterodimer stability ($\Delta G_{\text{heterodimer}}$) plotted against NPF rate (J_{theory}) in varied conditions. a) Vapor concentrations are constant: $[\text{acid}]=[\text{base}]=10^6$ molec cm^{-3} at varying temperature: $T=248, 273, 298, 323,$ and 348 K. b) Temperature is constant: $T=298$ K at varying vapor concentrations: $[\text{acid}]=[\text{base}]=10^5, 10^6, 10^7, 10^8,$ and 10^9 molec cm^{-3} . Text markers are centered over the data point.	81
4.9	Individual data points and trendlines from Figure 4.8a colored according to the number of remaining hydrogen bond donors (HBD) on the heterodimer. The left is data from the 298 K case, and the right is data from the 348 K case, at $[\text{acid}]=[\text{base}]=10^6$ molec cm^{-3}	82
4.10	Heterodimer concentration plotted against $J_{1.5}$ for sa–amm across 25 computational conditions (filled diamonds) from 248–348 K and monomer concentrations from 10^5 – 10^9 cm^{-3} , where a) shows the full set of conditions calculated for sa–amm, and b) shows a magnification of how CLOUD data compares to the computational dataset. Colored lines correlate to temperature trendlines that were drawn through all data points calculated at the same temperature. Dashed lines represent data points calculated at the same monomer concentrations. We calculated heterodimer concentrations for CLOUD data whose acid and base concentrations were within 50% of each other according to Equation 4.3. All CLOUD data points were collected at temperatures of either 248 or 273 K (colored circles corresponding to color scale) and with monomer concentrations between approx. 10^8 – 10^9 cm^{-3}	84
4.11	Heterodimer concentration plotted against $J_{1.5}$, wherein a) all data are represented with black dots, and b) data points are colored according to temperature and sized to reflect monomer concentrations (10^5 – 10^9 cm^{-3}). Data were fitted to an exponential function, which can be found in Equation 4.4.	85
4.12	A) Amm and b) gua sa salts’ $J_{1.5}$ plotted against Φ , where triangles are colored according the temperature of that point’s calculation. CLOUD data are shown as black dots, and their Φ values were calculated according to Equation 4.5. All trendlines used an exponential fit.	87
4.13	All sa salts plotted with a) base names as markers and b) markers colored according to their ΔG_A values. CLOUD observations are shown as filled circles.	88

LIST OF TABLES

	Page
1.1 Experiments conducted, their conditions, particle formation results, and their chapter, if applicable.	23
2.1 Thermodynamic modeling of H ₂ SO ₄ -NH ₃ and H ₂ SO ₄ -DMA particles.	43
4.1 Acid and base compounds in this study. Abbreviations are as follows: ammonia (amm), methylamine (ma), dimethylamine (dma), trimethylamine (tma), trimethylamine N-oxide (tmao), guanidine (gua), monoethanolamine (mea), piperazine (pz), putrescine (put), sulfuric acid (sa), methanesulfonic acid (msa), and nitric acid (na).	69
4.2 Experimental and calculated properties examined in this study.	70
4.3 Calculated enthalpy ($\Delta H_{\text{heterodimer}}$ in kcal/mol), entropy ($\Delta S_{\text{heterodimer}}$ in cal/(mol·K)) and Gibbs free energy ($\Delta G_{\text{heterodimer}}$ in kcal/mol) for sa-base heterodimer formation at 298 K.	73

ACKNOWLEDGMENTS

In many ways, I started the PhD as an experiment to see if I was smart enough, hardworking enough to do it. Now that I'm nearing the end of the program, rather than any of those things, I think I have instead characterized just how dumb I can be, and just how much this PhD is a culmination of all of the support I have been so lucky to have.

First, I'd like to thank my advisor, Jim Smith. You took me in when I was looking for a lab to call my own, and your passion for instrumentation sparked a passion within me that I never knew I could have. Your mentorship in the first year of my PhD, where I must have said "Jim, I think I broke the instrument..." countless times, has been invaluable to me. You taught me how to overcome gremlins that exist in any instrument by understanding them on a fundamental, first-principles perspective (and of course their quota of blood, sweat, and tears!). Your support of scientific meandering gave me the chance to do fun, wacky experimental setups without fear of backlash. Your unconditional support of my professional development allowed me to pursue opportunities that I would have otherwise passed up in favor of focusing solely on science. Thank you, Jim, and I am so grateful to you as both my advisor and as a human being.

I would like to thank Nanna Myllys for all of her mentorship and guidance, as well as her force-of-nature approach to doing science. Having you on this project has made not only my PhD a supremely better experience, but also elevated our science to another level. The speed at which you work, your candid perspective, your targeted science questions, and your unending positivity (with some excellent sarcasm) have provided a bastion of hope during my hardest times in this project. I have said this to you over and over again, but it deserves repeating: I am so grateful it was you who joined this project, and I don't want to know where the project would have been without you.

To my group – you all know how much I have enjoyed our time together. Mike, you were my go-to person after Jim for instrumentation, and your thoughtful approach to science has always inspired me. Danielle, you helped me temper my impulse to solve everything through labwork and focus on the "why" of my experiments. Hayley, our coffee breaks (and teeny dance breaks!) and camaraderie were highlights to many workdays. Deanna, your clarity in purpose and willingness to take the lead on the internal seminars and the AAAR student chapter gave me relief that these programs were in great hands. Lia, my homie, my dude, you reminded me of the joy of reading and brought nostalgic vibes of the Bay to our lab. Adam, it has been really fun mentoring you and I will miss our chats. To everyone – I could write so much about how grateful I am to all of you, but I'll keep it short and say you all have been the best labmates a girl could ask for.

Dr. Amy Christiansen, I am eternally grateful for our coffee chats and your excitement for all of my endeavors. Your maturity and grace and Midwestern-ness always inspired me to act with more of those qualities, and gave me valuable perspective in grad school, where perspective is sometimes hard to find.

I want to thank the heads of AirUCI and also the two other members of my committee, Professor Barbara Finlayson-Pitts and Professor Sergey Nizkorodov. Without the both of you, I would not have been able to have had the opportunity to take many of the leadership positions I have taken during my PhD. Professor Finlayson-Pitts, thank you so much for your outspoken support for my proposals in AirUCI. I am constantly reminded of how lucky I am, as a part of AirUCI, to have you champion and organize professional development for students. Sergey, your offer to take me in back when I was looking for a group cemented in my mind that you were an incredibly generous person, and I haven't been disappointed in the four years since. Thank you for your part in coordinating AirUCI activities and your support during my PhD, and I have always enjoyed your self-aware long introductions of guest speakers!

I want to thank AirUCI as a community as a whole, and specifically Veronique Perraud and Lisa Wingen, the two people who arguably are the scientific glue that keeps AirUCI running. Vero, your deep knowledge and passion for atmospheric chemistry always awed and inspired me to dig deeper into the science. Lisa, when I hear you laugh it instantly puts a smile on my face, and I still remember us taking the picture for a "Genius in the Box"! You both are so humble and hardworking – thank you for all of your time. I would also like to thank Melissa Sweet and Victoria Stewart-Goss for their administrative duties and unending positivity while dealing with my paperwork. You all are rock stars!

I want to thank Katie Forsman and Katie Androsky, both of whom are my best friends. Both of you have helped me through so much. Katie Forsman, you are my childhood friend and I know you always have my back but are ready to kick me into gear if needed. Katie Androsky, you kept me ready to keep taking care of myself physically and mentally because of our exercise challenges. Both of you are incredibly inspiring women and continuously showed up when I needed you. Thank you.

Of course, Rumble, my cat and my cuddle bug, thank you for being the reason for me to get out of bed some days and being my crazy, loving companion.

Last but not least, I would like to thank my family who have been my anchor throughout these hard six years. Dad, thank you for your continuous logistical support in navigating being an adult. Kenny, thank you for all of the good times playing board games and picking me up from the airport every time I would come to visit. Mom, thank you for simultaneously always keeping me grounded and being my number one fan. I am who I am because of all of you, and I would not have been able to be where I am today without knowing that you all will catch me if I fail. Thank you for being my home base and my true north.

I am grateful to the National Science Foundation for funding (CHE-1710580) my project for the last four years, and the Chemistry Department for funding my last quarter through the Graduate Dissertation Fellowship. I also acknowledge that the Taylor and Francis group and ACS Publications have granted permission to incorporate my published work into this dissertation.

VITA

Sabrina Chee

EDUCATION

Doctor of Philosophy in Chemistry University of California, Irvine	2015–2021 <i>Irvine, CA</i>
Bachelor of Science in Chemistry University of California, Davis	2010–2014 <i>Davis, CA</i>

RESEARCH EXPERIENCE

Graduate Research Assistant University of California, Irvine	2016–2021 <i>Irvine, California</i>
--	---

Principal Investigator: James N. Smith

- Studied the mechanism of nanoparticle formation in the atmosphere from acid-base reactions. Generated nanoparticles (20 nm) and correlated the H-bonding sites, pKa/pKb, and volatility of acids/bases with nucleation events and particle composition. Measured particle acid:base ratio down to 8 nm for the first time.
- Discovered that for particle sizes 15 nm in diameter, acid:base ratio of particles made from sulfuric acid and dimethylamine will deviate from stoichiometric neutrality. Collaborated with a theoretical/computational chemist to model the molecular level acid-base reaction, which showed that more acidic particles were as stable, if not more stable than neutral.
- Measured other combinations of acid/base and found that particles were fully neutralized for the sizes studied (8-30 nm). Theoretical estimations of particle cluster stability correlated well with these results, and these studies are among the first to indicate modeling techniques can be reasonably extrapolated to actual systems.
- Analyzed theoretical data of 27 acid-base systems to devise a model to predict particle formation rates based on calculated cluster stabilities. Determined that cluster stability is the most important factor in determining particle formation rates, and that the H-bonding ability of the clusters are crucial to growth.
- Found that particle composition correlates strongly with acid/base volatility: for a nonvolatile acid/nonvolatile base and volatile acid/volatile base, the acid:base ratio remains neutral; however, for a nonvolatile acid/volatile base, acid:base ratio tend to be more acidic. These results explain on a fundamental level why real-world measurements find particles to be more acidic, because sulfuric acid is the most abundant acid incorporated into particles in most areas.

Undergraduate Research Assistant

University of California, Davis

2012–2014

Davis, California

Principal Investigator: Carlito Lebrilla

- Isolated human milk peptides, digested them with naturally-occurring enzymes in breast-milk, and measured the products with mass spectrometry to form a baseline for the human milk peptidome.
- Streamlined the sample preparation process, which was then used to study the peptide concentrations present in bovine milk from mastitic cows in comparison to healthy cows.

WORK EXPERIENCE

Process Engineer Intern

Lam Research

2014–2015

Fremont, California

Supplier Engineering

- Learned and acquired expertise in anodized processes and parts testing metrology: Keyence optical-laser microscope, corrosion resistance, breakdown voltage, colorimetry, and roughness. Documented Lam procedures for measuring anodization quality with these instruments for the first time
- Supplier auditor for precision cleaners to ensure compliance with Lam specifications
- Won People's Choice Award at the Intern Poster Session in 2014

TEACHING EXPERIENCE

Chemistry Teaching Assistant

University of California, Irvine

Irvine, CA

H2LA/M2LA General Chemistry Lab

F2015, F2016

- Taught general lab skills and graded lab work using online grading tools, like Sapling, Electronic Lab Notebook (ELN), and Turnitin.com

H2LB/M2LB General Chemistry Lab

W2016

- Continuation of H2LA/M2LA

51C Organic Chemistry Lecture

S2016

- Taught discussions and review sessions; proofed, printed, and graded exams for a class of 250 students

H2B General Chemistry Lecture

W2019

- Taught discussion sections, made exam questions, printed exams, and graded using AI-assisted software, Gradescope

LEADERSHIP EXPERIENCE

Internal AirUCI Symposium Organizer **2018–2020**

- Proposed and founded a new seminar series in the environmental sciences to promote interdisciplinary discussion and collaboration among graduate students, postdoctoral researchers, and project scientists

Treasurer for the UCI AAAR Student Chapter **2018–2021**

- Applied for funding, organized fundraisers, and managed spending to enable professional development, outreach, and mentoring opportunities for graduate students

Teaching Assistant Mentor **2018–2019**

- Led a 2-day classroom lecture on teaching chemistry at UCI
- Mentored 5 chemistry graduate students on classroom management and teaching skills during their first year

Chemistry Outreach Club at UCI **2016**

- Performed chemistry demonstrations to local elementary and high school students to excite them about science. Designed and printed 4th of July cards depicting flame-test elements and their corresponding colors.

Tech Trek Lab Lead (held by the AAUW) **2016**

- Led an experiment as part of a camp to inspire young girls to pursue STEM-related fields

AWARDS

Graduate Dissertation Fellowship (UCI) **2021**

Michael E. Gebel Award **2019**

NSF Graduate Research Fellowship Honorable Mention **2016**

SKILLS

Mass Spectrometry (MS): setup of a homemade MS, quadrupole and TOF analyzers, TDCIMS, nitrate-CIMS, LC-MS

Other Instrumentation: Particle sizing and counting (APS, SMPS, DMA, CPC), collection (S3, MOUDI), and analysis (GC-FID, IC, CIMS)

Maintenance Skills: CEM/MCP detectors, pumps, ionization inlet characterization, soldering, circuit troubleshooting

Hardware: Soldering, machine shop tooling, basic circuit diagrams

Software: Igor Pro, Labview, OriginLab, ChemDraw, Microsoft Office

PUBLICATIONS

1. Myllys, N.; Myers, D.; Chee, S.; Smith, J. N. "Molecular properties affecting the hydration of acid-base clusters." *PCCP*. In review. 2021.
2. Chee, S.; Barsanti, K.; Smith, J. N.; Myllys, N. "A Predictive Model for Salt Nanoparticle Formation Using Heterodimer Stability Calculations." *Atmos. Chem. Phys.* In review. 2021.
3. Smith, J.N.; Draper, D.C.; Chee, S.; Dam, M.; Glicker, H.; Myers, D.; Thomas, A.; Lawler, M.J.; Myllys, N. "Atmospheric clusters to nanoparticles: Recent progress and challenges in closing the gap in chemical composition." *Journal of Aerosol Science*. 2020. 153.
4. Myllys, N.; Ponkkonen, T.; Chee, S.; Smith, J.N. "Enhancing Potential of Trimethylamine Oxide on Atmospheric Particles." *Atmosphere*. 2020. 11(1), 35.
5. Chee, S.; Myllys, N.; Barsanti, K.B.; Wong, B.; Smith, J.N. "An Experimental and Modeling Study of Nanoparticle Formation and Growth from Dimethylamine and Nitric Acid." *J. Phys. Chem. A*. 2019. 123, 26, 5640-5648.
6. Myllys, N.; Chee, S.; Olenius, T.; Lawler, M.J.; Smith, J.N. "Molecular-Level Understanding of Synergistic Effects in Sulfuric Acid-Amine-Ammonia Mixed Clusters." *J. Phys. Chem. A*. 2019. 123, 12, 2420-2425.
7. Li, X.; Chee, S.; Hao, J.; Abbatt, J.P.D.; Jiang, J.; Smith, J.N. "Relative humidity effect on the formation of highly oxidized molecules and new particles during monoterpene oxidation." *Atmos. Chem. Phys.* 2019. 19, 1555-1570.
8. Chen, H.; Chee, S.; Lawler, M.J.; Barsanti, K.C.; Wong, B.M.; Smith, J.N. "Size-resolved chemical composition of nanoparticles from reactions of sulfuric acid with ammonia and dimethylamine." *Aerosol Science and Technology*. 2018. 52(10), 1120-1133.
9. Guerrero, A.; Dallas, D.C.; Contreras, S.; Chee, S.; Parker, E.A.; Sun, X.; Dimpasoc, L.; Barile, D.; German, B.; Lebrilla, C.B. "Mechanistic Peptidomics: Factors that Dictate the Specificity on the Formation of Endogeneous Peptides in Human Milk." *Mol. Cell. Proteomics*. 2014. 13(12), 3343-51.
10. Guerrero, A.; Dallas, D.C.; Contreras, S.; Bhandari, A.; Canovas, A.; Islas-Trejo, A.; Medrano, J.F.; Parker, E.A.; Wang, M.; Hettinga, K.; Chee, S.; German, B.J.; Barile, D.; Lebrilla, C.B. "Peptidomic analysis of healthy and subclinically mastitic bovine milk." *Int. Dairy J.* 2015. 46, 46-52.

PRESENTATIONS * indicates presenter

1. *Chee, S.; Myllys, N.; Smith, J.N. "Predicting Salt NPF Rates from Heterodimer Stability." Internal AirUCI Seminar, February 2021.
2. *Smith, J.N.; Lawler, M.J.; Draper, D.C.; Chee, S.; Glicker, H.; Li, X. "Indoor New Particle Formation: An 'Outsider's' Perspective." American Association for Aerosol Research Conference, 2019.
3. *Myllys, N.; Olenius, T.; Chee, S.; Smith, J.N. "Mechanisms and Compounds in Atmospheric Acid-Base Particle Formation." American Association for Aerosol Research Conference, 2019.
4. *Smith, J.N.; Chee, S.; Myllys, N.; Li, X.; Jiang, J. "It's the water: Exploring impacts of water vapor on new particle formation mechanisms." American Chemical Society Conference, August 2019.
5. *Chee, S.; Myllys, N.; Barsanti, K.C.; Wong, B.M.; Smith, J.N. "Determining nanoparticle acid to base ratio: an experimental and modelling case study of DMA-HNO₃ nanoparticles." Internal AirUCI Symposium, January 2019.
6. *Li, X.; Chee, S.; Jiang, J.; Smith, J.N. "RH Effect on the Oxidation of α -pinene and the Influence on New Particle Formation." International Aerosol Conference, August 2018.
7. *Chen, H.; Lawler, M.J.; Chee, S.; Smith, J.N. "Size-resolved chemical composition of nanoparticles from reactions of sulfuric acid with ammonia and dimethylamine." American Association for Aerosol Research Conference, October 2017.
8. Guerrero, A.; *Chee, S.; Lebrilla, C.B. "Unraveling the proteolytic resistance of lactotransferrin in human milk." Larock Conference at UC Davis, May 2013.

POSTERS * indicates presenter

1. *Smith, J.N.; Li, X.; Chee, S.; Myllys, N.; Jiang, J.; Pierce, J.R. "Exploring the impacts of water vapor on new particle formation mechanisms." American Geophysical Union Conference, 2019.
2. *Chee, S.; Myllys, N.; Barsanti, K.C.; Wong, B.M.; Smith, J.N. "Acid-base reactive uptake of dimethylamine and nitric acid for the formation and growth of nanoparticles: cluster simulations and nanoparticle composition measurements." American Association for Aerosol Research Conference, 2019.
3. *Li, X.; Li, Y.; Chao, Y.; Chee, S.; Hao, J.; Smith, J.N.; Jiang, J. "Size-resolved Chemical Composition of Sub-40 nm Particles during New Particle Formation and Growth Events in Beijing." American Association for Aerosol Research Conference, Oct 2019.
4. *Wu, J.; Glicker, H.; Chee, S.; Smith, J.N. Long-Term Observations of Ultrafine Particle Size Distributions in the Colorado Desert of Southern California. Undergraduate Research Opportunities Program Conference, 2019.
5. Li, X.; Chee, S.; Jiang, J.; *Smith, J.N. "RH Effect on the Oxidation of α -pinene and the Influence on New Particle Formation." Atmospheric Chemical Mechanisms Conference, 2018.
6. Chee, S.; Lawler, M.J.; Barsanti, K.C.; Wong, B.M.; *Smith, J.N. "Size-Resolved Physicochemical Properties of Organic Salt Nanoparticles." International Aerosol Conference, 2018.
7. *Chee, S.; Chen, H.; Lawler, M.J.; Smith, J.N. "Size-resolved acid:base ratio of atomized nanoparticles from salt solutions." American Association for Aerosol Research Conference, 2017.

ABSTRACT OF THE DISSERTATION

Understanding the Mechanisms of Salt Formation in New Particle Formation and Growth

By

Sabrina Chee

Doctor of Philosophy in Chemistry

University of California, Irvine, 2021

Professor James N. Smith, Chair

Atmospheric nanoparticle formation and growth processes are major sources of uncertainty in our understanding of global climate. However, nanoparticle composition is notoriously difficult to measure below 30 nm due to their incredibly low mass, and so a full understanding of the compounds that contribute to nanoparticle growth still remains elusive. In addition, nanoparticle physical and chemical properties are continuously changing at different sizes. To date, nanoparticles have been known to form from either the condensation of extremely low volatility organic compounds or the reactions of acids and bases in the atmosphere. For the latter, sulfuric acid has been observed to be the predictor of new particle formation events and, recently, amines and ammonia have been shown to stabilize sulfuric acid-containing clusters and contribute to nanoparticle formation and growth. However, size-resolved composition of nanoparticles resulting from these acid-base pairs, as well as the extent to which other atmospherically relevant acids and bases contribute to new particle formation, are both still unknown. This dissertation uses both modeling and experimental methods to understand different acid-base systems' nanoparticle formation and growth processes.

In Chapter 2, we generated particles made from sulfuric acid with either dimethylamine and ammonia under dry and humid conditions to measure their size-resolved composition using Thermal Desorption Chemical Ionization Mass Spectrometry. Sulfuric acid-ammonia experiments were conducted with 100x higher concentrations of ammonia compared to sulfuric acid to mimic atmospheric conditions, while sulfuric acid-dimethylamine experiments were conducted with concentrations on

the same order of magnitude. In all cases, the particles that were formed deviated from stoichiometric neutrality. In both humid and dry cases, sulfuric acid and ammonia formed particles that contained more acid than base, despite the starting concentration differences. In humid conditions, sulfuric acid and dimethylamine formed particles that also had a higher concentration of sulfuric acid compared to dimethylamine for particles smaller than 12 nm. However, under dry conditions, these particles seemed to have more dimethylamine than sulfuric acid. Thermodynamic models using different pK_a values to describe the acid and base behavior in these systems are discussed.

Next, in Chapter 3, we probed the composition of particles formed from nitric acid and dimethylamine using the same methods. In this case, under all conditions, nitric acid and dimethylamine formed particles in a 1:1 acid:base ratio at all sizes measured (9–30 nm). Here we also applied quantum chemical methods to calculate cluster stabilities for clusters containing up to 4 acid and 4 base molecules to discern if the initial growth pathways were reflected in composition measurements. Results show that cluster simulations predicted the behavior of nitric acid and dimethylamine particles, because both nitric acid and dimethylamine are too volatile to remain in the particle phase without salt formation.

In order to better understand the very first steps of new particle formation, we used the same computational theory to model and calculate the stabilities of acid-base heterodimers (1 acid and 1 base clusters) formed from 3 different acid and 9 different base molecules in Chapter 4. We compared these values to aqueous-phase acidity, gas-phase acidity, base vapor pressure, dipole moment, and polarizability to find out which was the strongest predictor of heterodimer stability, the first step in forming a cluster. Then, we compared heterodimer stability of just the sulfuric acid salts with calculated new particle formation rates. From this, we developed a model that parametrizes heterodimer stability to predict new particle formation rates, which were found to be in good agreement with experimental values for the sulfuric acid-ammonia system.

Chapter 1

Introduction

1.1 List of Research Articles

This thesis consists of an introduction and three research articles. These papers are outlined below and are referenced throughout the introduction by their roman numeral (e.g., **Paper II**).

- I.** Chen, H.; **Chee, S.**; Lawler, M.J.; Barsanti, K.C.; Wong, B.M.; Smith, J.N. “Size-resolved chemical composition of nanoparticles from reactions of sulfuric acid with ammonia and dimethylamine.” *Aerosol Science and Technology*. **2018**. 52(10), 1120-1133. DOI: <https://doi.org/10.1080/02786826.2018.1490005>
- II.** **Chee, S.**; Myllys, N.; Barsanti, K.B.; Wong, B.; Smith, J.N. “An Experimental and Modeling Study of Nanoparticle Formation and Growth from Dimethylamine and Nitric Acid.” *J. Phys. Chem. A*. **2019**. 123, 26, 5640-5648. DOI: <https://doi.org/10.1021/acs.jpca.9b03326>
- III.** **Chee, S.**; Barsanti, K.; Smith, J. N.; Myllys, N. “A Predictive Model for Salt Nanoparticle Formation Using Heterodimer Stability Calculations.” *Atmos. Chem. Phys.* In review. **2021**. DOI: <https://doi.org/10.5194/acp-2021-84>

Other papers related to the project but were not incorporated into the thesis are outlined below and are also referenced throughout the text by their roman numerals.

- IV.** Myllys, N.; **Chee, S.**; Olenius, T.; Lawler, M.J.; Smith, J.N. “Molecular-Level Understanding of Synergistic Effects in Sulfuric Acid-Amine-Ammonia Mixed Clusters.” *J. Phys. Chem. A*. **2019**. 123, 12, 2420-2425. DOI: <https://doi.org/10.1021/acs.jpca.9b00909>
- V.** Myllys, N.; Ponkkonen, T.; **Chee, S.**; Smith, J.N. “Enhancing Potential of Trimethylamine Oxide on Atmospheric Particles.” *Atmosphere*. **2020**. 11(1), 35. DOI: <https://doi.org/10.3390/atmos11010035>
- VI.** Smith, J.N.; Draper, D.C.; **Chee, S.**; Dam, M.; Glicker, H.; Myers, D.; Thomas, A.; Lawler, M.J.; Myllys, N. “Atmospheric clusters to nanoparticles: Recent progress and challenges in closing the gap in chemical composition.” *Journal of Aerosol Science*. **2020**. 153. DOI: <https://doi.org/10.1016/j.jaerosci.2020.105733>

1.2 Background

1.2.1 Impact of Atmospheric Nanoparticles for Health and Climate

Atmospheric aerosols, suspensions of gases and particles in air, have effects on human health and global climate that are not yet fully understood. Aerosol particles can be broken down into the following size ranges: the nucleation or Aitken mode ($\sim 1-100$ nm), the accumulation mode ($\sim 100 - 2000$ nm), and the coarse mode ($\sim 2 - 10$ microns) (Finlayson-Pitts and Pitts, 2000; Whitby, 1978). These size ranges are broken down largely as a distinction between each size range’s formation pathways, which are depicted in Figure 1.1. Nucleation or Aitken mode particles are made primarily from the formation of a nucleus from low volatility vapors in the atmosphere, while accumulation mode particles (as the name suggests) is the mode that forms from the coagulation of the smaller mode’s particles. In contrast to these two modes, the coarse size range of particles are typically

produced from more mechanical methods, like dust, volcanic eruptions, and combustion emissions. In this dissertation, we will be focusing on understanding the formation and growth processes of nucleation or Aitken mode particles, with diameters smaller than 100 nm, and will refer to these as “atmospheric nanoparticles.”

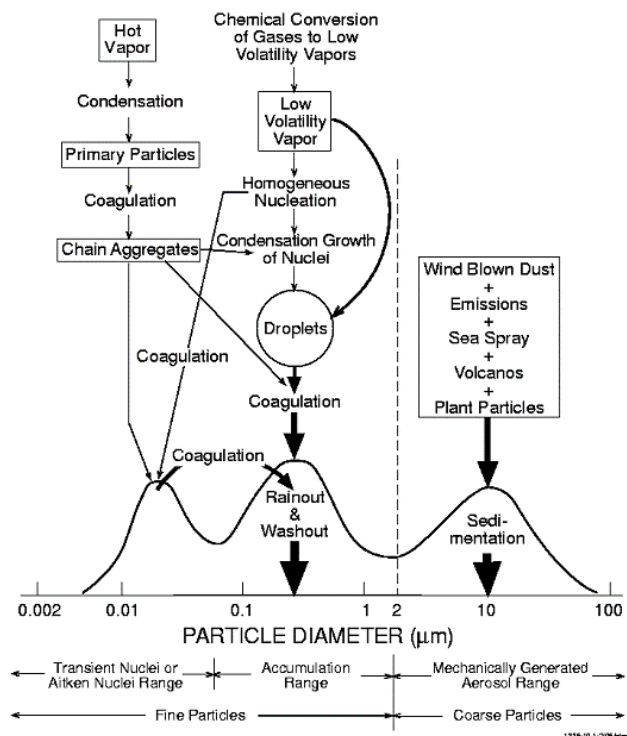


Figure 1.1: Formation and removal pathways of atmospheric aerosol sorted by size, reproduced from Whitby (1978).

In general, nanoparticles are too small to scatter significant amounts of light; however, they are crucial precursors to larger accumulation mode particles which are more effective light scatterers. In addition, they have the potential to form cloud condensation nuclei (CCN), which govern the formation of clouds by providing the nucleus for water condensation (Merikanto et al., 2009; Pierce and Adams, 2009; Westervelt et al., 2013). In 2014, the IPCC reported the indirect forcing effect from aerosols was the single largest uncertainty in global radiation models (IPCC, 2014). Nanoparticle formation, growth, and in-particle chemical processes still remain mysterious and exacerbate this uncertainty in climate models (Pierce and Adams, 2009), which in turn emphasizes the need for a mechanistic understanding of how nanoparticles form and grow.

In addition, nanoparticles have been shown to affect human health in an emerging field coined as nanotoxicology by Oberdörster et al. (2005). In contrast to larger particles which are deposited on the walls of the respiratory system prior to the deepest part of the lungs, nanoparticles can travel all the way to the alveoli where oxygen exchange occurs (Allen et al., 2017; Oberdörster et al., 2004). Because nanoparticles are so small, they are able to more easily translocate into the bloodstream through endocytosis, phagocytosis, and other cell transport processes, where they can then cause adverse health effects. Studies have also shown that nanoparticles are able to translocate to the brain and increase the likelihood of contracting neurological illnesses (Allen et al., 2017; Jew et al., 2019; Oberdörster et al., 2004). In addition, nanoparticles are the precursor to fine particles, which have been correlated with adverse health effects like asthma and heart disease (Arden Pope III and Dockery, 2012; Dockery et al., 1993; Turner et al., 2008). Understanding how nanoparticles are formed and what components lead to negative health effects is crucial in reducing their impact on human health, and on top of nanoparticle climate effects, is what motivates this thesis.

1.2.2 Known mechanisms of nanoparticle formation and growth

In general, particles are formed through either primary or secondary processes, where primary particles are emitted directly into the atmosphere from a mechanical process (e.g., dust, sea spray, pollen, etc.), and secondary particles are formed through gas-to-particle conversion processes to nucleate new particles (Finlayson-Pitts and Pitts, 2000; Whitby, 1978). Nanoparticles are typically formed through secondary processes in new particle formation (NPF) events, which has been observed in both remote and polluted environments (Baccarini et al., 2020; Lee et al., 2019; Weber et al., 1996). While nanoparticles have also been observed to come from primary processes, like sea spray and combustion, studies have shown that NPF, as we will discuss below, is still the dominant contributor to CCN populations globally (Kulmala et al., 2004, 2017).

NPF is the secondary process by which gas molecules collide and form clusters of molecules held together by intermolecular bonds (Kirkby et al., 2011; Pichelstorfer et al., 2018; Weber et al., 1996; Zhang et al., 2012; Whitby, 1978). These clusters must quickly grow to larger sizes to avoid removal

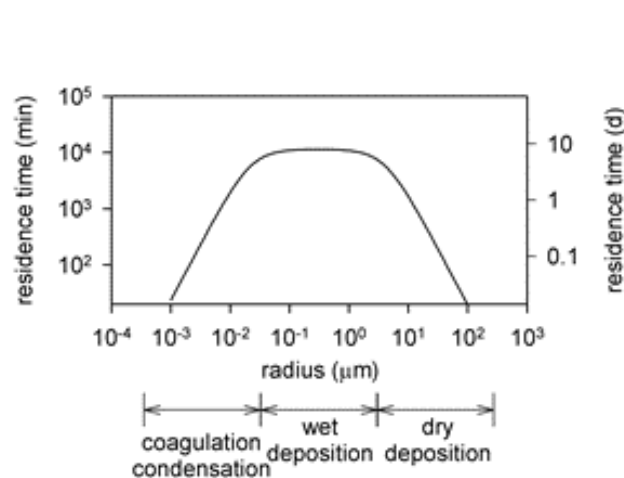
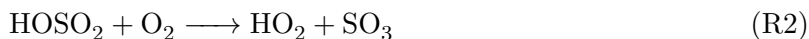


Figure 1.2: Residence times of particles according to size, as well as their main loss pathways, reproduced from Smith et al. (2004).

by coagulation with other particles (Cai and Jiang, 2017; Kuang et al., 2010), as shown by Figure 1.2, which illustrates the residence time of particles in the atmosphere. Nanoparticles between the sizes of 1–10 nm have residence times on the order of minutes. However, despite their need for fast uptake, the growth pathways for these clusters are restricted due to the Kelvin effect, which is the phenomenon in which the condensation of molecules onto a curved surface requires a supersaturation of the condensing species (Finlayson-Pitts and Pitts, 2000). For small particles, condensational growth is only possible through either an irreversible condensation of a very low volatility species or the reaction of a volatile molecule at the surface of the particle to form a nonvolatile product (reactive uptake).

1.2.3 Acid-base reactions in the atmosphere

Historically, sulfuric acid concentrations have been one of the most reliable predictors of NPF events, and therefore, nanoparticle production, in the atmosphere (Almeida et al., 2013a; Kirkby et al., 2011; Sipilä et al., 2010; Weber et al., 1995). This makes sense in urban environments where there are many sources of sulfur dioxide (SO_2), which can be chemically converted to sulfuric acid in ambient air by the mechanism shown in Scheme 1:



However, with the exception of SO_2 plumes downwind of major sources such as coal-fired power plants and volcanoes, sulfuric acid concentrations alone cannot account for all nanoparticle formation and growth. This is especially true when considering growth to sizes where species more volatile than sulfuric acid can contribute. Measurements of ambient atmospheric clusters and sub-20 nm nanoparticles have shown that ammonia, amines, and oxidized organics are important participants in NPF in most locales (Ehn et al., 2014; Junninen et al., 2010; Smith et al., 2008b, 2010b; Wang et al., 2006).

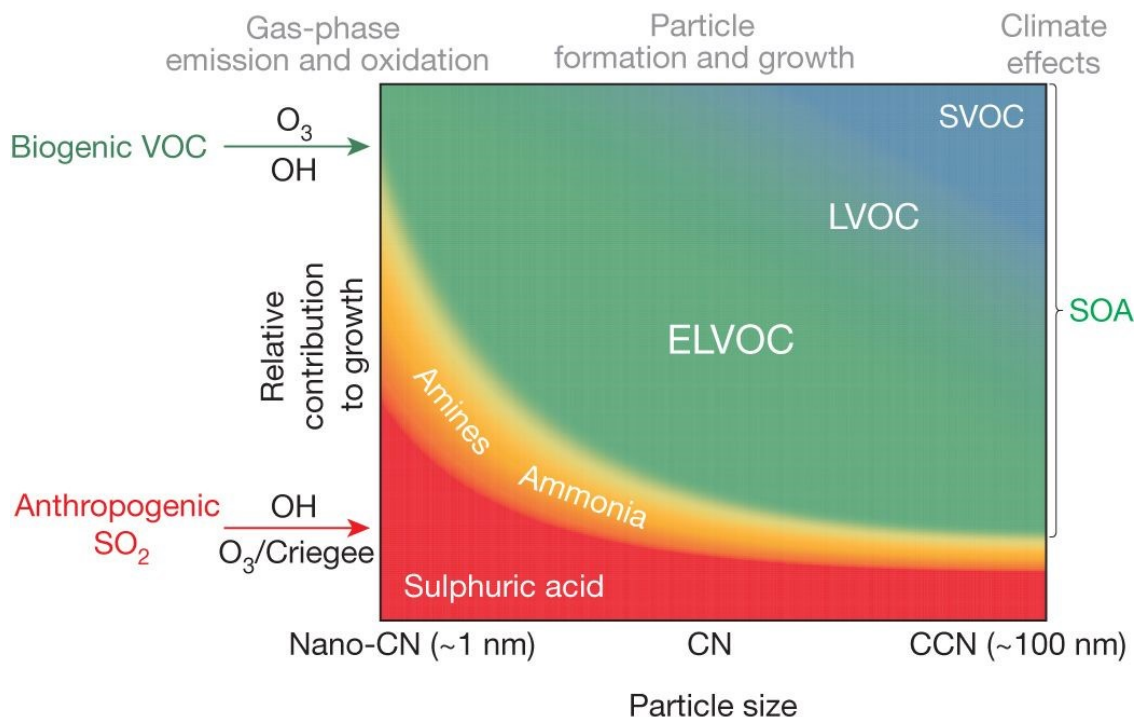


Figure 1.3: Relative contributions of compounds to nanoparticle growth as a function of size. Reproduced from Ehn et al. (2014).

Indeed, these NPF precursors are illustrated in Figure 1.3 from Ehn et al. (2014), which depicts the known contributors and mechanisms to atmospheric particle growth as a function of size. From the smallest size (~ 1 nm), the main species that contribute to growth are sulfuric acid, amines/ammonia, and extremely low volatility organic compounds (ELVOCs), and as particles become bigger, more low volatility and semi-volatile organic compounds (LVOC and SVOC, respectively) are able to partition into the particle as the Kelvin effect becomes less important. In the case of sulfuric acid and ELVOCs, they both have low enough volatilities to overcome the Kelvin effect, and thus their collision with a particle will result in irreversible condensation. However, amines and ammonia, both semivolatile compounds, can only stay in the particle by undergoing an acid-base reaction to form their protonated counterparts, which are essentially nonvolatile ions (Barsanti et al., 2009; Lavi et al., 2015; Smith et al., 2010b). This has been further discussed in **Paper I**. Acid-base reactions enable relatively volatile species to contribute to nanoparticle growth and further reduce the vapor pressure of the participating acid by forming the anion. We discuss the acids and bases relevant to this thesis and their sources below.

Sulfuric acid, as previously discussed, is formed through the photochemical processing of SO_2 in the atmosphere (Dada et al., 2020; Finlayson-Pitts and Pitts, 2000). SO_2 is formed from the combustion of sulfur-containing fossil fuels and volcanic activity (Finlayson-Pitts and Pitts, 2000; Whitby, 1978), and so concentrations of sulfuric acid are most abundant in urban areas where fuel burning is commonplace and directly downwind of volcanoes. Sulfuric acid is a strong acid with a first acid dissociation constant (pK_a) of -3 for its first proton transfer (Slater, 2014). Concentrations of sulfuric acid can range from approximately 10^3 – 10^8 molec cm^{-3} depending on the relevant sources and sinks in the area (Dada et al., 2020).

In contrast, nitric acid is relatively abundant in the atmosphere with concentrations on the order of parts-per-billion (ppb), or approximately 10^{10} molec cm^{-3} (Afpel et al., 1979; Finlayson-Pitts and Pitts, 2000; Huang et al., 2002). Nitric acid is primarily formed from the reaction of nitrogen dioxide (NO_2) with OH radical, but can also result from the interfacial hydrolysis of N_2O_5 on a particle surface, or the abstraction of a hydrogen by nitrate radical (NO_3) from an organic compound (Finlayson-Pitts and Pitts, 2000; Huang et al., 2002). Nitric acid is also a strong acid, with a pK_a of

-1.3 (Slater, 2014). Nitrate (NO_3^-) has been measured in sub-50 nm particles, despite ammonium nitrate being too volatile to remain in particles of that size (Lawler et al., 2014; Smith et al., 2004, 2008b) (see **Paper II**).

Both of these acids have been found to be stabilized in the particle-phase because of reactions with atmospheric bases, namely, ammonia and amines (Angelino et al., 2001; Bzdek et al., 2010; Glasoe et al., 2015; Kurt et al., 2008; Smith et al., 2010b). Ammonia is the most abundant base in the atmosphere and is derived from numerous sources, most notably from agricultural uses like animal husbandry or fertilizers (Behera et al., 2013; Finlayson-Pitts and Pitts, 2000; Nair and Yu, 2020). Ammonia concentrations can range from a few ppt in remote areas to tens of ppb near emission sources (Nair and Yu, 2020). However, ammonia is a relatively weak base with a conjugate acid pK_a value of 9.25 (Slater, 2014).

In contrast, methyl-, dimethyl-, and trimethyl-amine conjugate pK_a values are 10.66, 10.73, and 11.09, respectively (Slater, 2014), almost two orders of magnitude more basic than ammonia. These relatively stronger basicities have been used to explain why amines are present in atmospheric nanoparticles, despite their smaller overall ambient concentrations. The methyl-substituted amines (methyl, dimethyl, and trimethylamines) come from similar sources to ammonia, like animal husbandry and farming, and are typically found in concentrations ranging from ppq to tens of ppt depending on distance from their emissions source (Ge et al., 2011; Qiu and Zhang, 2013). Despite ammonia being present in the atmosphere at, on average, 3 orders of magnitude larger concentrations than amines, amines are consistently detected in atmospheric nanoparticles (Qiu and Zhang, 2013; Smith et al., 2010b). The interaction between amines or ammonia with atmospheric acids in enhancing nanoparticle formation and growth is not well understood and has been studied in **Papers IV and V**.

1.2.4 Lab studies of salt particle behavior

Laboratory studies have recently set out to understand salt formation’s effects on nucleation and size-dependent particle composition. For nucleation, numerous studies have catalogued the enhancing effect of bases on sulfuric acid nucleation rates. In flow tube experiments (Ball et al., 1999) and those performed at the Cosmics Leaving OUtdoor Droplets (CLOUD) chamber (Duplissy et al., 2016), sulfuric acid was reacted with ammonia and showed up to orders of magnitude enhancement in nucleation rates compared to homogeneous nucleation with sulfuric acid alone. Studies of sulfuric acid and dimethylamine (with 10 pptv contaminant ammonia) at CLOUD showed larger enhancement at lower concentrations (Almeida et al., 2013a). Glasoe et al. (2015) studied the effect of relative humidity and the stabilization of different seven different bases on the enhancement of NPF rates in flow tube experiments and found that the order of enhancement is $\text{NH}_3 < \text{MA} < \text{TMA} < \text{DMA}$, and that other amines studied (TEA, amides, urea, and acetamide) were less effective at increasing NPF rates, and suggest the reason is that the less effective bases were less basic and hampered salt formation. They also found that mixing ammonia and amines yield increased NPF rates, and reasons for that base synergy has been studied on a molecular level in **Paper IV**.

Fewer laboratory studies focused on NPF of systems not involving sulfuric acid and ammonia or amines. Chen and Finlayson-Pitts (2017) observed the reactions of methanesulfonic acid with ammonia or amines as a function of temperature (21–28°C) and found that for the lower end of those temperatures, NPF rates are greatly increased and become atmospherically relevant. Wang et al. (2020) recently studied the nucleation and growth of particles made from nitric acid and ammonia at wintertime temperatures (-15°C). In that study, they demonstrated that at this colder temperature, atmospherically relevant concentrations of nitric acid and ammonia can nucleate and grow particles sufficiently fast to escape the so-called “valley of death,” a size range for which loss rates to of nanoparticles to surfaces due to diffusion often out-competes growth rates.

While its importance is undeniable, measuring the size-dependent composition of nanoparticles is extremely difficult. Figure 1.4 shows the measurement methods available for studying nanoparticle composition. While the figure focuses on measurement methods that may be able to measure ambi-

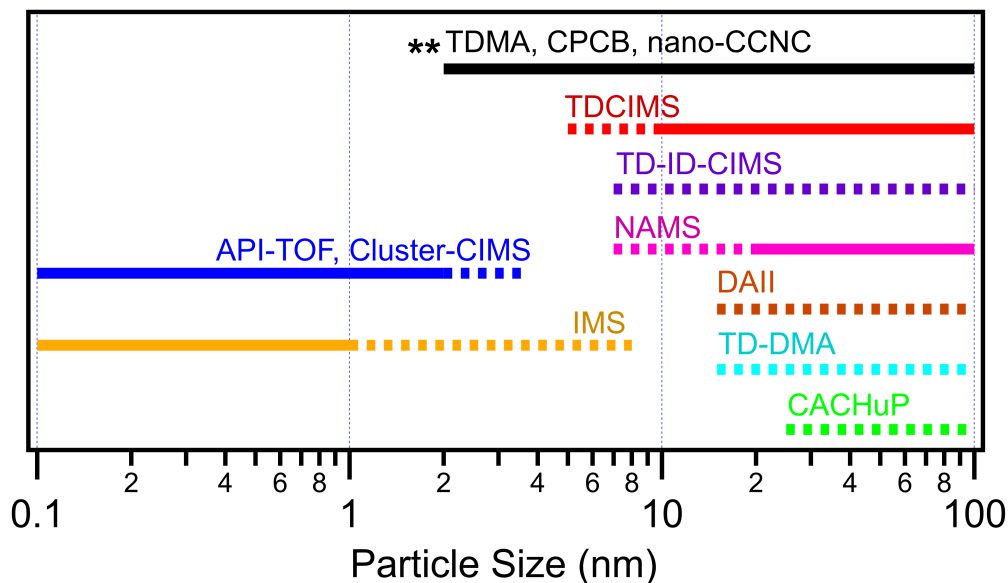


Figure 1.4: Illustration of the measurement size ranges of state-of-the-art instruments. Instruments that are starred (**) measure physical properties of their size range, while other instruments can probe the composition of nanoparticles to some degree. Solid lines indicate size ranges that the instrument has measured in the field, while dotted lines indicate size ranges the instrument has measured in the lab. Figure reproduced from **Paper VI**.

ent concentrations of nanoparticles, it highlights the gap in compositional measurement techniques for particles between 3–10 nm. In essence, once particles are nucleated and grow past 3 nm, particle compositional changes remain a mystery. We present key papers below that look at the composition and behaviors of nanoparticles from either the perspective of clusters (sub 3-nm particles) or larger particles (>10 nm particles).

In a study of cluster composition, Schobesberger et al. (2015a) produced clusters with ammonia and sulfuric acid and found that the acid:base ratios of clusters ranged from ~ 0.7 –1, and are not fully neutralized despite up to 500x more ammonia than sulfuric acid. Bzdek et al. (2017) measured the stability of clusters formed from sulfuric acid and ammonia in an FT-ICR-MS and found that the rate-limiting step in the acid-base reaction to be the addition of sulfuric acid, while the addition of ammonia was collision-limited.

Because amines were shown to also enhance NPF rates, several studies have focused on understanding how they might also interact with a growing particle. Bzdek et al. (2010) conducted a study

of the displacement reaction of dimethylamine on ammonium sulfate clusters. Dimethylamine is more basic than ammonia (Slater, 2014), which makes the proton transfer reaction between sulfuric acid and dimethylamine more favorable than between sulfuric acid and ammonia. In this study, the authors showed that for a cluster of up to 8 ammonium bisulfate molecules, displacement was complete. However, in larger ammonium bisulfate clusters, only the ammonia molecules on the surface of the particle were displaced by dimethylamine. In each of these experiments, ammonium sulfate clusters were charged and trapped in a vacuum while they were exposed to dimethylamine gas, so water was not a factor in uptake.

On the other end of the size spectrum, the studies conducted by Chan and Chan (2012) measured the displacement of ammonia by triethylamine onto large droplets (15–35 μm in diameter) for various ammonium salts (sulfate, bisulfate, nitrate, chloride, and oxalate). At higher RH (50–75%), triethylamine displaced all ammonia, but when RH was low and the salt systems formed crystalline solids, displacement only occurred for a small fraction of ammonia molecules. More experiments have shown that reactive uptake and displacement of bases is nuanced, dependent on particle size, particle phase-state, and base structure (Chan and Chan, 2013; Qiu and Zhang, 2013; Sauerwein et al., 2017; Shen et al., 2020).

Lawler et al. (2016) showed that nanoparticles (10–50 nm) formed in a reaction chamber with 2 orders of magnitude more dimethylamine than sulfuric acid, particles still remained mostly composed of sulfuric acid, with an astounding acid:base ratio of 10:1. In addition, the experiment was conducted in the presence of contaminant ammonia (approx. half the concentration of dimethylamine). These acid:base ratios and compositional measurements were confirmed by measurements of size-resolved nanoparticle hygroscopicity using a Hygroscopicity Tandem Differential Mobility Analyzer (HTDMA). In the context of the above studies that show that the more basic amines displace ammonia, we would expect that ammonia would be a small to nonexistent fraction of particle signal; however, Lawler et al. showed that particulate ammonia signal was on the same order of magnitude as particulate dimethylamine. These seeming contradictions beg the questions: Why do nanoparticles contain more acid under conditions that favor neutralization? What physicochemical factors govern the competitive uptake of bases?

1.2.5 Measurement and Modeling Gap

Because it is extremely difficult to probe the molecular dynamics that govern these reactions through laboratory studies alone, thermodynamic and quantum chemical modelling are crucial to providing context to our experimental observations. This is especially the case for nanoparticles smaller than 10 nm, which contain environments that are drastically different from larger particles or bulk systems (e.g., increased ionic strength, increased dielectric constant, and changes in molecular behavior due to varying amounts of water).

To date, quantum chemical calculations have been used to explain the very first steps of acid-base particle nucleation, from precursors to a cluster containing ten molecules (5 acid 5 base), which is equivalent to approximately a 1.5 nm particle. Modelled systems reflect measured cluster data and NPF rates moderately well in many cases (Almeida et al., 2013a; Myllys et al., 2016a; Olenius and Riipinen, 2017; Schobesberger et al., 2015a). Thermodynamic data obtained by quantum chemical calculations can be used as an input in cluster dynamics simulations, which allow step-by-step cluster growth modeling, as done in **Papers II, IV, and V**. For those systems studied, cluster dynamics simulations have helped to explain cluster growth behaviors, which has been discussed in **Paper IV**. However, calculations larger than 1.5 nm take exponentially more computational time and quickly become infeasible (Elm et al., 2020). In many cases for nanoparticle measurements, like in Lawler et al. (2016) as well as in **Paper I**, without a molecular-level picture, we are unable to fully explain the measured behavior, and are restricted to discussion of its implications.

1.3 Nanoparticle Production and Measurement Methods Used

Each thesis chapter will discuss the specific methods used for the experimental results and conclusions. This section will discuss overarching experimental ideas and challenges associated with nanoparticle production and analysis in the lab.

The production of particles in the nanoparticle size range (1–50 nm) in a controllable and tunable way is crucial to setting up size-resolved composition experiments. In this thesis, the production of nanoparticles in the lab has been generally confined to three methods: nucleation, atomization, and electrospray aerosol generation (EAG). All experimental studies discussed in this thesis use either atomization or nucleation for nanoparticle composition analysis. Although EAG is an incredibly useful tool that can produce nanoparticles for laboratory studies, its operation is often not stable enough for the timescales needed for our nanoparticle composition measurements for sizes sub-10 nm (>2 hr depending on particle mass concentrations). In addition, EAG-produced nanoparticle composition has been shown to be affected by the highly charged surface. MacMillan et al. (2012) showed that nanoparticles tended to have higher concentrations of more surface-active molecules that were more able to hold charge compared to the bulk solution because of nanoparticles' increased surface area-to-volume ratio. Additionally, EAG-produced clusters were shown to be directly affected by the polarity of the electrospray, where the clusters contained more electronegative molecules if the polarity was negative, with the opposite being true for clusters generated with a positive electrospray (Bzdek et al., 2011). Because of these reasons, we instead explored the composition of particles nucleated from gas phase acids and bases and showed how their composition changes as they grow, and used atomized particles as a benchmark for understanding the sensitivity of our measurements to different molecules.

1.3.1 Nucleation Flow Reactor

A nucleation flow reactor, as the name suggests, involves the introduction of the gaseous precursors into a reaction vessel to induce the nucleation of particles, and is used in the studies described in **Papers I and II**. A common example of nucleation nanoparticle generation is the formation of ammonium sulfate particles through the introduction of sulfuric acid vapor and ammonia vapor into a flow tube (Glasoe et al., 2015). Sulfuric acid and ammonia will react to form clusters and then grow into particles through reactive uptake, which can then be sampled from the exit port of the flowtube. In order to make these particles repeatably, the precursor gases must be introduced

at variable and controllable concentrations. We accomplished this by either using a saturator or permeation tube.

The operating principle of a saturator is to hold a compound (either liquid or solid) at a stable temperature so that its vapor pressure will remain constant. The air volume above the compound is assumed to reach equilibrium with the compound’s saturation vapor pressure quickly (hence, saturator). We flowed typically between 0.1–1 liters per minute (LPM) of nitrogen (N_2) over the liquid within our saturators to our downstream reaction chamber. The saturator we used was temperature-controlled via the use of a water jacket with temperature varying from 0°C to 30°C. The saturators used were always cleaned and dried thoroughly prior to the experiment to avoid contamination.

Permeation tubes are typically comprised of a semi-volatile compound that is fully enclosed by a PTFE tube, sealed at both ends, with a small amount of dead volume inside. Because PTFE is inherently porous, the volatile compound slowly permeates through the confines of the permeation tube and produces a stable source of vapor. For our experiments, a permeation tube was placed inside of a glass vial that was continuously held at 30°C, wherein a constant flow of 0.1 LPM N_2 carried the permeated gases to the downstream reaction vessel. The emission rate was determined by weighing the permeation tube directly before use, and then measuring how much mass was lost after each month. Equation 1 demonstrates how mass can be translated to concentration in our flow:

$$\text{Vapor concentration} \left(\frac{\text{molecules}}{\text{cm}^3} \right) = \frac{\frac{\text{molecules lost (molecules)}}{\text{time since last weighing (minutes)}}}{N_2 \text{ flow rate} \left(\frac{\text{cm}^3}{\text{minute}} \right)} \quad (1)$$

Because permeation tubes rely on molecules diffusing through a porous PTFE wall, the concentrations produced by permeation tubes are generally much lower than those produced by a saturator, which directly samples the headspace above a compound. In general, saturators are great for use with low volatility compounds like sulfuric acid, whereas permeation tubes are good in combination with higher volatility compounds, like ammonia or dimethylamine.

Downstream of either the saturator(s) or permeation tube(s) lies the reaction chamber, which provides a volume for the gases to react and form particles. The reaction chamber can be designed to provide more or less turbulence, which would affect the mixing and reaction times within the chamber. The result of a longer reaction time, given enough precursor concentration, would be larger, older particles. However, due to turbulence and a lack of plug flow, particles will almost always be produced in a polydisperse distribution of sizes, rather than a narrow distribution. Often in these experiments, we think of the particle size akin to the relative “age” of the particle – in other words, the larger the particle, the older. This is useful because we can then take snapshots of the growth process of these particles with size-resolved measurements, where we can see the composition of 10 nm particles, then the composition of 12 nm particles, and so on, where differences between the 10 nm particle and the 12 nm particle can be attributed to the 2 nm growth. Indeed, if the reaction vessel is able to be controlled for relative humidity, temperature, and light, these snapshots of composition can be very informative as to how a particle is affected by the interaction between its precursors and the environment it grew in.

1.3.2 Spray Atomizer

Spray atomization produces particles mechanically by a high-velocity gas jet that passes over the tip of capillary containing a sample solution. The gas jet shears the liquid at the tip of the capillary creating droplets. The jet also reduces the pressure at the tip, causing additional sample to be drawn through the capillary to sustain droplet production. This produces particles usually ranging in size from tens of nanometers to microns, depending on the geometry of the atomizer, the pressure applied, and the amount of drying applied to the droplets. For the atomizer used in our studies (TSI Constant Output Atomizer Model 3076), particles are produced between 15–3000 nm in size. The larger droplets can be dried to nanoparticle sizes by drying the aerosol flow through the use of a desiccant, NafionTM dryer, dry dilution flow, or some other water vapor removal method. For small particles, droplets that are initially sprayed by the atomizer must have low enough solute concentrations to have a dry sub-15 nm diameter. However, the smaller the concentration of the solute, the more likely contamination of the bulk solution will have an effect on particle composition.

Because of this, atomization is a method ill-suited to produce particles smaller than 15 nm in diameter. Regardless, atomization is an easy, consistent, and relatively inexpensive way to produce particles of a known composition and has been used to observe partitioning (Stangl et al., 2017), hygroscopicity (Braban et al., 2001), calibrate aerosol analysis equipment (Eiguren-Fernandez et al., 2014; Liu and Deshler, 2010; Voisin et al., 2003), particle phase measurements (Brooks et al., 2002), as well as provide seed particles for particle growth studies (Murphy et al., 2007), and was used in both **Papers I and II** to calibrate the sensitivity of the mass spectrometer.

1.3.3 Measurement Methods

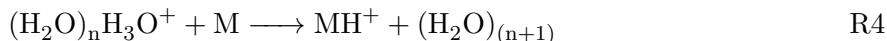
Thermal Desorption Chemical Ionization Mass Spectrometer (TDCIMS)

The Thermal Desorption Chemical Ionization Mass Spectrometer (TDCIMS) was developed by Smith and colleagues at the National Center for Aerosol Research (NCAR) in Boulder, Colorado (Voisin et al., 2003). The TDCIMS is unique in that it is one of a few instruments in the world that can measure ambient nanoparticle composition below 50 nm in size. Since 2003, the TDCIMS has measured nanoparticle composition in both urban and remote field studies, as well as in the lab to measure particles down to 5 nm in size (Lawler et al., 2014, 2016; Perraud et al., 2020; Smith et al., 2004, 2008b) (also used in **Papers I and II**).

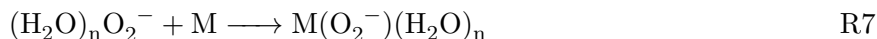
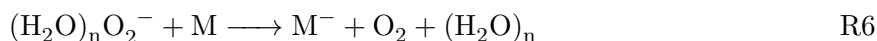
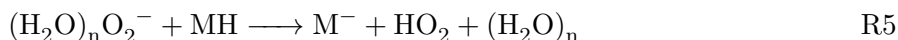
The principle of operation of the TDCIMS is as follows: charged nanoparticles are optionally size-segregated using a nanometer differential mobility analyzer (nDMA) and then electrostatically deposited onto a platinum wire, which after collecting sufficient particle mass, then moves to an ionization region that is located in front of the inlet orifice of the mass spectrometer. The ionization region is equipped with a ^{210}Po radioactive source and held under clean nitrogen flow that contains trace amounts of O_2 and H_2O , which are ionized to produce the reagent ions O_2^- and H_3O^+ . These reagent ions inevitably cluster with trace amounts of water molecules, which in the case of H_3O^+ makes them more selective for ions with higher proton affinity. The wire is resistively heated by applying an alternating current, the latter of which can be stepped or ramped to approximately

650°C. This causes the deposited particles to desorb into the gas phase, where constituents are then chemically ionized and measured by a mass spectrometer. The chemical ionization schemes for species R are shown in Scheme 2 for both positive and negative ion modes, where $n = 0-2$.

Positive Ion Mode:



Negative Ion Mode:



In positive ion mode, compounds with sufficient proton affinity are ionized by H_3O^+ donating an H^+ (R4). In negative ion mode, ionization can occur through three separate pathways, where O_2^- can either react and remove a proton from the target molecule (R5), donate its electron to an electronegative molecule (R6), or cluster with the molecule (R7). In these acid-base experiments, the base will be measured in the positive ion mode and have an m/z of $M+1$ as it accepts a proton from H_3O^+ , and in general, the acid will be measured in the negative ion mode as $M-1$ as it gives up its proton to O_2^- .

The design of the TDCIMS is complex, but each component is designed to overcome the aforementioned challenges of measuring nanoparticle composition: namely, nanoparticle charging and the collection of sufficient sample mass to differentiate from background contamination. In order to charge enough particles, a unipolar charger (UPC) is used in place of a bipolar charger (BPC) to increase the charging efficiency of particles smaller than 20 nm by exposing particles to ions of a single polarity (Chen and Pui, 1999). In the case of the TDCIMS, positive ions are removed from a cylindrical cell by applying an electric field across a region irradiated by three ^{210}Po radioactive sealed sources). A second electric field is applied downstream of the sources to expose nanoparticles to generated negative ions, which increases nanoparticle charging efficiency by up to an order of magnitude (Smith et al., 2004). This increase in charging efficiency helps alleviate the challenge of collecting sufficient sample mass by increasing the number of particles collected. After the nanopar-

ticles are charged, size-selection can occur using a nDMA, which separates particles according to their surface area-to-charge ratio. In both the charging and size-selection process, diffusional losses can be large. In addition, ions detected from particles are differentiated from background ions by turning off the collection voltage and repeating the collection and analysis cycle. This results in a background spectrum that is subtracted from the spectrum obtained from sampled particles. This subtraction effectively minimizes the effect of gas-phase contamination and gas desorption from inlet surfaces, and ensures that the resulting subtracted spectrum contains only signal from particulate matter (Lawler et al., 2016).

Due to the unavoidable impacts of diffusional losses, the main challenge for all TDCIMS measurements is the collection of sufficient sample mass for analysis, which is a function of the chemical complexity of the particles, ionization efficiency, thermal degradation, and other complications in the sampling process. Despite the progress in the design of the inlet with the addition of the UPC and in the increases in mass spectrometer sensitivity, overcoming the exponential decrease in sample mass as we push for the measurement of smaller and smaller diameters of nanoparticles is extremely difficult. It is for these reasons that the TDCIMS measurements in **Papers I and II** are limited to particles larger than 8 nm in diameter.

Other Measurements

In order to characterize the reaction conditions and particle physical properties, particle size distributions (scanning mobility particle sizer, SMPS), temperature, relative humidity, gas-phase concentrations (transverse ionization chemical ionization mass spectrometry, TI-CIMS), and offline particle chemical analysis measurements (sequential spot sampler coupled with ion chromatography) were performed. Temperature and relative humidity measurements were performed using a homemade probe that was inserted into the exhaust outlet’s aerosol flow.

Particle size distributions using SMPS are ubiquitous in the atmospheric chemistry field (Finlayson-Pitts and Pitts, 2000; Kulkarni et al., 2011). For these studies, the nDMAs were operated using clean “zero air” as sheath flow instead of recirculated air. Recirculating the sheath air causes it to

be contaminated by any semivolatile gases from the upstream reaction vessel and causes the nDMA and any components associated with the sheath and excess flows, such as the filters and blower, to become contaminated. Many of these parts are almost impossible to clean. Most importantly, these contaminated parts can desorb vapors into the sheath air, thus exposing sampled particles to contaminated gas and impacting particle composition.

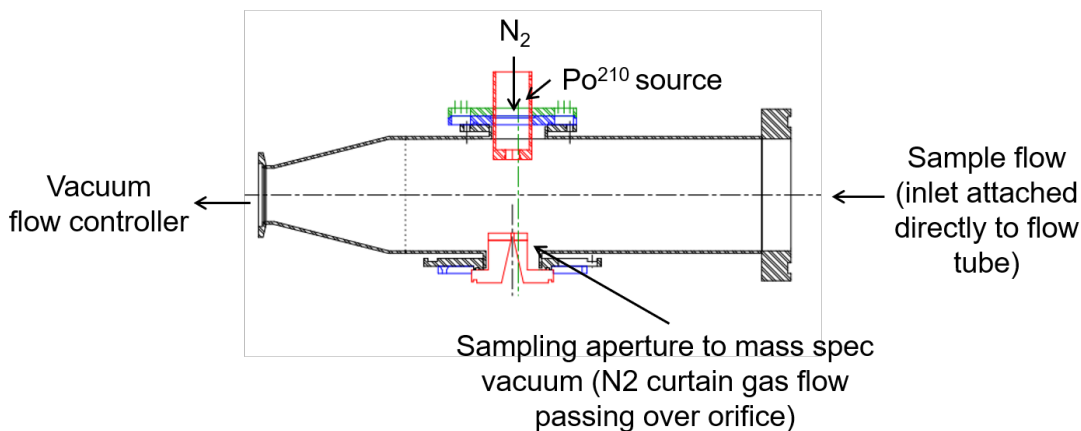


Figure 1.5: Schematic of the TI-CIMS inlet used in **Paper II**.

The Transverse-Ionization Chemical Ionization Mass Spectrometer (TI-CIMS) is an inlet whose design was inspired by the cluster-CIMS inlet by Zhao and Eisele and is discussed in depth in (Li et al., 2019). The inlet design used in this dissertation is shown in Figure 1.5. The design is unique in that it minimizes wall surface area between the inlet, the reaction zone between the reagent ion and analytes of interest, and the critical orifice of the mass spectrometer. This in turn minimizes wall losses of semi-volatile compounds inside of the inlet of the instrument, which lends itself to more accurate gas-phase measurements of low- and semi-volatile compounds like amines. The inlet in our studies uses the same ionization chemistry as the TDCIMS, with H_3O^+ and O_2^- as reagent ions. The TI-CIMS inlet was used in experiments in Chapter 3 to characterize the concentrations of dimethylamine under different relative humidity conditions. In addition, for experiments with oxalic acid and dimethylamine, we used it to confirm oxalic acid, introduced via saturator, was reaching the flow tube reactor.

The Sequential Spot Sampler (S3, Aerosol Devices, Inc.) was used to collect 20–30 nm particles into a small spot that was then extracted and analyzed on an ion chromatograph (IC, Metrohm) to

confirm that 20–30 nm particles made from either nucleation or atomization are stoichiometrically neutral (Eiguren-Fernandez et al., 2014). The S3 was used in these experiments instead of filter collection because of its ability to grow nanoparticles as small as 8 nm in diameter into water droplets, which could then be focused and impacted into a 1 mm diameter “spot” onto a chemically inert well plate. This well plate could be extracted with less than 100 μL of water, which is not feasible for filter sample extraction. This smaller extraction volume was crucial for making sufficient sample concentrations for analysis with IC. Once neutral acid:base ratios were confirmed for these particles, atomized particles larger than 20 nm were used to calibrate TDCIMS ion sensitivity.

1.3.4 Challenges Working with Salt Systems

Pervasiveness of Semivolatile Compounds

It is important to note that all of the chemical systems that were explored in these studies contained at least one semi-volatile compound. We emphasize here the necessity of thorough cleaning of the entire experimental apparatus, including the TDCIMS inlet, when changing chemical systems. For example, if the reaction chamber was not cleaned after being used for reactions between nitric acid and dimethylamine, particles could be produced by only flowing nitric acid vapor through it, since dimethylamine is incredibly sticky and very slowly desorbs off surfaces. Or, if the TDCIMS inlet was not cleaned, dimethylamine desorbing off the walls could repartition into sampled particles during collection (especially if they were ammonium salt particles) and appear in the mass spectrum. One example of this occurred after measuring particles generated from reactions of trimethylamine-N-oxide (TMAO) and sulfuric acid. Following this, we sampled dimethylaminium sulfate nanoparticles generated from an atomizer. We found trimethylamine peaks in the mass spectrum of these particles, as shown in Figure 1.6. This remained true even after cleaning all equipment and tubing upstream of the TDCIMS. This was most likely because TMAO, a very low volatility compound, deposited on the walls of the inlet, decomposed in the presence of water and oxygen to break the N – O zwitterionic bond and slowly formed trimethylamine, which began to desorb and partition into the particles. This behavior persisted for over two weeks with heated, clean air passing through the

inlet before we decided to remove the entire inlet and clean it thoroughly with ultrapure water. This emphasizes the need for other experiments dealing with semivolatile compounds to perform cleaning of not only the reaction apparatus, but also the inlets to any instruments used to determine chemical composition.

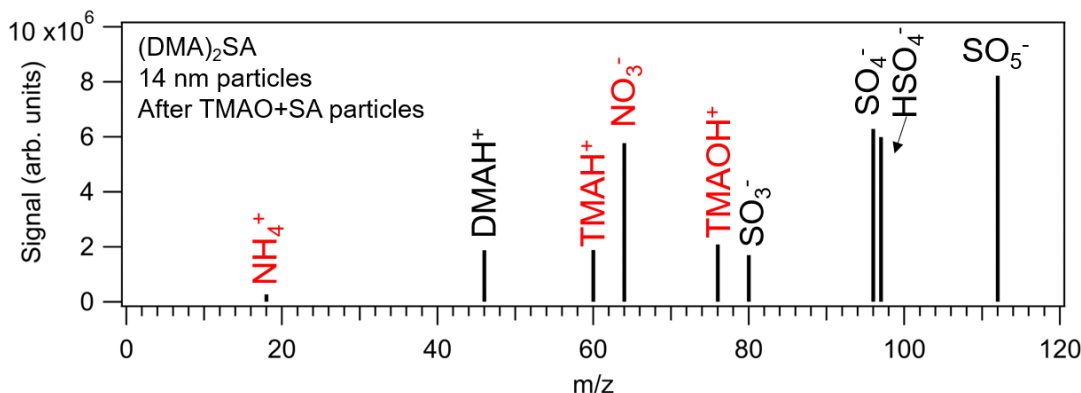


Figure 1.6: Mass spectrum of particulate signal from size-selected dimethylammonium sulfate particles. Signals in red are contaminants from previous experiments that partitioned from within the TDCIMS inlet. All upstream tubing and surfaces had been cleaned, including UPCs and nDMAs.

Nanoparticle Generation of the Size of Interest

As stated previously, nanoparticles must grow quickly enough to overcome the so-called “valley of death,” where small clusters are competitively scavenged by either the walls of the reaction chamber or by coagulation with other particles compared to nanoparticle growth. This makes the study of particles smaller than 10 nm in diameter very difficult, because the lifetime of these particles is extremely short. In experiments conducted by Perraud et al. (2020), the reaction time between methanesulfonic acid and dimethylamine was varied from 0.6 s to 9 s, which showed a very small shift in the mode diameter (6 nm and 7 nm, respectively). In Chapter 2 we produced particles from sulfuric acid and ammonia and were unable to broaden the size distribution to include particles above 12 nm despite lengthening the reaction time in a similar fashion. In these experiments, the systems’ mode diameters seem almost insensitive to changes in reaction time. On the other hand, during our experiments with nitric acid and dimethylamine in Chapter 3, when attempting to reduce the reaction time from 60 s to less than 40 s (with a mode diameter of 14 nm), the measured size

distributions were unstable from scan to scan. It seems that in the methanesulfonic acid and sulfuric acid experiments, there was a “maximum” stable diameter for the system conditions (precursor concentrations, relative humidity, temperature, etc.) with respect to reaction time, whereas for the nitric acid experiments, there was a “minimum” stable diameter. This observation is supported by Arquero et al. (2017a), where they observed the changes in geometric mean diameter between reactions of oxalic acid, methanesulfonic acid, and methylamine at varying relative humidities, where the smallest reaction time measured was at 0.8 s. For each of the studies, very few of the size distributions had a geometric mean diameter of less than 5 nm, despite the fact that the mean diameter would increase given a few more seconds of reaction time. It would be interesting to see studies that probed the dependence of particle mode diameter on precursor gas concentrations, precursor identities, and other reaction conditions to produce tunable acid-base particle diameter systems – given, of course, extremely thorough cleanings of the entire reaction apparatus between experiments.

Unfavorable Nanoparticle Systems

Certainly, the most difficult aspect of this project was attempting to make nanoparticles that were simply not thermodynamically stable. Two systems that did not make sufficiently stable nanoparticles for measurement were acetic acid with dimethylamine, and oxalic acid with dimethylamine. In both cases, they produced particles after the reaction chamber, but after size-selection with a nDMA, wherein the vapors were diluted by the zero-air sheath flow, particles evaporated before reaching the TDCIMS wire. In the case of acetic acid and dimethylamine, the TDCIMS showed no difference between the background and collection scans, which implies that particles were evaporating on the wire during collection. We hypothesize particles were able to form prior to size selection because of the high concentration of acetic acid in the flow tube, but once inside the TDCIMS inlet, sampled particles are bathed in a pure nitrogen sheath gas used to reduce gas phase contamination. Under this condition, the particles evaporated. In the case of oxalic acid and dimethylamine, size distributions actually became smaller after size selection (e.g., after size selecting for 15 nm particles, the resulting size distribution was centered on 13 nm), which implied a similar evaporation was

Table 1.1: Experiments conducted, their conditions, particle formation results, and their chapter, if applicable.

Acid	Base	RH conditions	Nanoparticle formation	Chapter Discussed
H ₂ SO ₄	NH ₃	0, 60	Yes	2
H ₂ SO ₄	DMA	0, 60	Yes	2
HNO ₃	DMA	<5, 55	Yes	3
CH ₃ COOH	DMA	0	Yes, but not stable enough for analysis	N/A
HOOC ₂ COOH	DMA	0	Yes, but not stable enough for analysis	N/A
H ₂ SO ₄	TMAO	0	Yes	See Paper V

occurring in the nDMA and TDCIMS inlet. As a sanity check, ammonium sulfate particles were atomized and size selected with the same equipment and the size selection showed a 15 nm selection and a 15 nm-centered size distribution. The two systems mentioned here did not form stable nanoparticles, and thus could not be studied for their composition. As these compounds have been observed in ambient ultrafine particles (Smith et al., 2010b, 2008a), an additional stabilizing process must be occurring such as hydrogen bonding with trace amounts of particulate-phase water. The species and mechanisms responsible for this stabilization is an important subject for future studies.

1.3.5 Systems Measured

The systems that were experimentally measured in this thesis are as shown in Table 1.1, a summary of their particle formation result, and their corresponding chapter (if any).

1.4 Dissertation Goals and Chapter Descriptions

This dissertation has multiple goals all relating to understanding how acid-base reactions contribute to new particle formation and growth in the atmosphere. The questions being asked in this dissertation are detailed below, with their corresponding chapters shown:

Goals:

1. For 2-component acid-base systems, how does nanoparticle acid:base ratio change as a function of size, if at all? Does relative humidity affect composition? [Chapters 2 and 3]

2. What physical properties of the participating acid and base molecules affect nanoparticle composition? [Chapters 2 and 3]
3. Similarly, what properties affect new particle formation? [Chapter 4]
4. How accurately can modeling approaches approximate new particle formation or nanoparticle composition? [Chapter 4]

In Chapter 2, we produced particles in a flow tube made from reaction of sulfuric acid with either dimethylamine or ammonia and measured their size-resolved composition using TDCIMS (see **Paper I**). In each system, relative humidity in the reaction chamber was either held at dry conditions or 60% RH. Sulfuric acid concentrations were 100x less than ammonia during the reaction, and on the same order of magnitude of concentration as dimethylamine, so particles produced would be expected to be fully neutralized. However, size-resolved composition measurements revealed that acid:base ratio never reached stoichiometric neutrality (1 acid, 2 base) for any of the systems for particles below 12 nm in diameter. Thermodynamic modeling was used to describe the effect of nanoparticle size on acid and base behavior in these systems, wherein aqueous pK_a values were adjusted to fit the acid:base ratios measured. The results of this chapter emphasize the importance of size-resolved measurements to reflect compositional changes as nanoparticles grow, and how nanoparticle behavior below 12 nm may be different than larger particles or bulk systems.

Chapter 3 used the same experimental design wherein we reacted nitric acid with dimethylamine under dry and humid conditions and measured the resulting size-resolved composition of the nanoparticles produced (see **Paper II**). However, the size-resolved acid:base ratio stayed stoichiometrically neutral (1 acid, 1 base) for all sizes measured (9–30 nm). Quantum mechanical calculations combined with a cluster dynamics model were used to calculate the stability of nitric acid-dimethylamine clusters containing up to 4 acid and 4 base molecules. These calculations showed that the only stable clusters were those that were neutralized, with evaporation rates for non-neutralized clusters being over ten orders of magnitude greater than neutralized clusters. The same modelling method was applied to the results of Chapter 2, and show that clusters that contained more sulfuric acid than base could be stabilized by the plethora of H-bonding opportunities on sulfuric acid. How-

ever, the acid:base ratio seen in Chapter 2 still was not fully explained with this method. These results show that in some cases, modelling can reflect nanoparticle composition when the acid-base reaction is crucial to retaining molecules in the particle (i.e., both nitric acid and dimethylamine are semi-volatile compounds), but still cannot fully explain the behavior of sulfuric acid and base systems.

Chapter 4 is a purely computational study, where we applied the computational methods used in Chapter 3 to different acid-base systems in order to understand the key factors in new particle formation and predict nucleation rates (see **Paper III**). First, we compared the gas-phase acidities, volatilities, dipole moment, and polarizability of 3 acid and 9 base molecules to their corresponding heterodimer stability (defined here as the Gibbs free formation energy of a cluster of 1 acid and 1 base molecule) to find which physical properties were predictors of heterodimer formation. Gas-phase acidity was the most accurate predictor, followed by aqueous-phase acidity, while volatility, dipole moment, and polarizability did not correlate at all to heterodimer stability. We then compared heterodimer stability of just the sulfuric acid salts to modelled new particle formation rates ($J_{1.5}$), which had been previously shown to match well with experimental NPF rates. From these comparisons, we were able to parametrize heterodimer stability to predict NPF rates within a few orders of magnitude, which were then verified for sulfuric acid-ammonia with experimental values from CLOUD chamber studies.

Chapter 2

Size Resolved Chemical Composition of Nanoparticles from Reactions of Sulfuric Acid with Ammonia and Dimethylamine

2.1 Abstract

Nanoparticle formation and growth driven by acid-base chemistry was investigated by introducing gas-phase sulfuric acid (H_2SO_4) with ammonia (NH_3) or dimethylamine (DMA) into a flow tube reactor. A thermal desorption chemical Ionization mass spectrometer was used to measure the size-resolved chemical composition of H_2SO_4 -DMA and H_2SO_4 - NH_3 nanoparticles formed under dry conditions and at 60% relative humidity. In contrast with predictions for bulk aqueous systems, nanoparticles showed a strong size-dependent composition gradient and did not always reach a fully

This is an Accepted Manuscript of an article published by Taylor & Francis in Aerosol Science and Technology on June 8, 2018, available online: <http://www.tandfonline.com/10.1080/02786826.2018.1490005>.

neutralized state in excess of gas-phase base. Smaller particles were more acidic, with an acid:base ratio of 0.7 ± 0.1 and 1.3 ± 0.3 for 8.6 and 9.5 nm H_2SO_4 -DMA particles formed under dry and humid conditions, respectively, and 3.1 ± 0.6 and 3.4 ± 0.3 for 7.5nm H_2SO_4 - NH_3 particles formed under dry and humid conditions, respectively. The acidity of particles generally decreased as particles grew. H_2SO_4 -DMA particles became fully neutralized as they grew to 14 nm, but H_2SO_4 - NH_3 particles at 12 nm were still acidic and were never observed to reach bulk sample thermodynamic equilibrium for the experimental conditions in this study. Thermodynamic modeling demonstrated that the observed trends can be reproduced by modifying acid dissociation constants to minimize acid-base chemistry, which may be caused by steric or mixing effects, and by considering volatilization of the neutral base.

2.2 Introduction

Particle nucleation from gaseous precursors represents a significant source of aerosols in the atmosphere (Finlayson-Pitts and Pitts, 2000; Kulmala et al., 2004; Zhang et al., 2012; Seinfeld and Pandis, 2006). Newly formed particles can continue growing in the atmosphere to ~ 100 nm, at which size they may act as cloud condensation nuclei and thereby impact cloud properties and lifetimes with implications for the global radiative energy balance (Kerminen et al., 2005; Spracklen et al., 2008; Kuang et al., 2009; Merikanto et al., 2009). Nucleation and subsequent growth are collectively known as new particle formation (NPF). The species involved in NPF, and the underlying mechanisms, have been the subjects of many studies over the past two decades. Sulfuric acid (H_2SO_4) is well-recognized to be critical in many NPF events (Weber et al., 1996, 1997; Sipilä et al., 2010; Kulmala et al., 2006; McMurry et al., 2000; Weber et al., 2001). Amines and ammonia (NH_3) can bond strongly with H_2SO_4 , and greatly enhance NPF (Ball et al., 1999; Korhonen et al., 1999; Yu, 2006; Kurtén et al., 2008; Benson et al., 2009; Berndt et al., 2010; Erupe et al., 2011; Kirkby et al., 2011; Zollner et al., 2012; Almeida et al., 2013a; Glasoe et al., 2015). Recent studies suggest that organic acids such as methanesulfonic acid (Kreidenweis et al., 1989; Wyslouzil et al., 1991; Dawson et al., 2012; Chen and Finlayson-Pitts, 2017), and highly oxidized, low-volatility organic

compounds (Donahue et al., 2013; Schobesberger et al., 2013; Bianchi et al., 2014; Ehn et al., 2014; Riccobono et al., 2014; Bianchi et al., 2016; Tröstl et al., 2016) also play an important role in NPF.

While both amines and NH_3 can enhance NPF in the presence of H_2SO_4 , laboratory studies and theoretical calculations have shown that amines are more effective compared to NH_3 due to their higher basicity (Kurtén et al., 2008; Barsanti et al., 2009; Berndt et al., 2010; Erupe et al., 2011; Yu et al., 2012b; Zollner et al., 2012; Almeida et al., 2013a; Glasoe et al., 2015). Field studies have also reported the presence of aminium salts in ambient particles (Facchini et al., 2008; Pratt et al., 2009; Sorooshian et al., 2009; Smith et al., 2010a), and the strong correlation between NPF and the presence of amines (Freshour et al., 2014; Jen et al., 2014a; Hemmilä et al., 2018). Displacement of NH_3 with amines in H_2SO_4 - NH_3 clusters and particles has been observed in laboratory studies (Bzdek et al., 2010; Qiu et al., 2011; Liu et al., 2012), with a close-to-collision-limited rate for small clusters (Bzdek et al., 2010). Given that the concentration of NH_3 in the atmosphere is at least one order of magnitude higher than that of amines (Ge et al., 2011), both amines and NH_3 are expected to be important in NPF, depending on the proximity of their emission sources. Water vapor has also been reported to be critical during the initial steps of NPF (Berndt et al., 2010; Erupe et al., 2011; Loukonen et al., 2010; Zollner et al., 2012; Henschel et al., 2014; Yu et al., 2017).

After clusters form in the H_2SO_4 -base system, they can continue to grow by the formation of particle-phase ionic (and thus non-volatile) dissociated acids and bases, condensation of H_2SO_4 due to its very low saturation vapor pressure, and coagulation with existing clusters and/or particles (Kurtén et al., 2008; Chen et al., 2012; Keskinen et al., 2013; Lawler et al., 2016; Lehtipalo et al., 2016). Although many studies have focused on NPF in the H_2SO_4 -base system, only a few studies focused on chemical composition of those newly formed clusters and particles due to the challenges associated with the determination of chemical composition of clusters and nanometer-size particles. Measurements of molecular clusters that have fewer than 20 molecules in the H_2SO_4 -base system (corresponding to a particle diameter of about 2 nm) made at the Cosmics Leaving OUtdoor Droplets (CLOUD) chamber at CERN show a formation process involving stepwise addition of H_2SO_4 and base, typically in a 1:1 ratio (Kirkby et al., 2011; Almeida et al., 2013a; Bianchi et al., 2014; Kürten et al., 2014; Schobesberger et al., 2015a). Strong acid-base interactions in these molecular clusters

drive cluster growth during the early stages of NPF. However, in a recent study at the CLOUD7 campaign, hygroscopicity measurements of H_2SO_4 -base particles formed in excess of dimethylamine (DMA) or NH_3 show that particles as small as 10 nm are much more hygroscopic than particles at 15 nm, suggesting that the smaller particles are more acidic in the acid-base system (Kim et al., 2016). The acidity of newly formed particles decreases as they grow (Kim et al., 2016). This is further confirmed by direct measurements of the chemical composition of those nanoparticles formed in the same experiments using Thermal Desorption Chemical Ionization Mass Spectrometry (TDCIMS) (Lawler et al., 2016). The formation of highly acidic particles in excess of base is not consistent with the theory for bulk aqueous systems, which predicts that bulk sample thermodynamic equilibrium between H_2SO_4 and base should be reached (Lehtipalo et al., 2016). These findings demonstrate that uncertainties remain in understanding particle growth in the H_2SO_4 -base system.

In this study, we present chemical composition measurements of newly formed particles in the diameter range of 8-21 nm in the H_2SO_4 -base system. We specifically focus on size-resolved acid:base ratios of newly formed H_2SO_4 -base nanoparticles. The effect of relative humidity (RH) on nanoparticle composition is also explored. Thermodynamic modeling studies were performed to provide possible explanations for the experimental observations. The work provides valuable insights into the growth of particles after nucleation from gaseous precursors.

2.3 Experimental

2.3.1 Experimental Setup

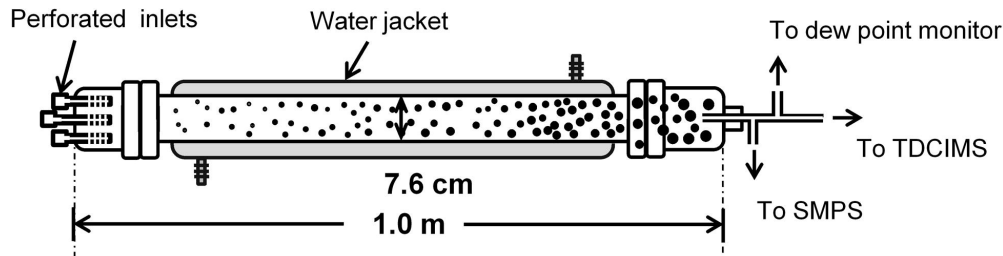


Figure 2.1: Schematic of the flow tube reactor.

Particles were formed by mixing gaseous H_2SO_4 and DMA or NH_3 in purified air using a flow tube reactor fabricated from borosilicate glass as shown in Figure 2.1. The flow tube measured 7.5 cm in diameter and 105 cm in length, with a total volume of 4.8 L. Three inlets were located at the upstream end for separately introducing reactants: gas-phase H_2SO_4 , DMA or NH_3 , and dry or humidified air. The inlets were perforated to enable rapid mixing of reactant gases in the upstream region. Particles were collected at the downstream end of the flow tube for analysis. The residence time of gases in the flow tube was ~ 1 min.

Gas flows were controlled and monitored with mass flow controllers. Gas-phase H_2SO_4 was generated by passing a 1 sLpm flow of gaseous N_2 , generated from the headspace of a liquid N_2 dewar, through a 30 cm long glass saturator filled with 5 ml of 96% liquid H_2SO_4 (Fisher Scientific). The saturator was water jacketed to control H_2SO_4 temperature at 30 °C. Concentrations of H_2SO_4 in the flow tube were calculated by assuming gas-phase H_2SO_4 reached its saturation vapor pressure before exiting the saturator. This assumption is supported by several experimental and theoretical studies (Brus et al., 2010; Herrmann et al., 2010; Panta et al., 2012; Zollner et al., 2012; Neitola et al., 2015). Our apparatus is identical to that described in Zollner et al. (2012), who measured the $[\text{H}_2\text{SO}_4]$ as it exited a 30 °C saturator as a function of carrier gas flow rate. They found that concentration varied linearly with flow rate over the range of 0.5 – 1.5 sLpm, and concluded that saturation conditions apply over this flow range. Neitola et al. (2015) employed a lower carrier gas flow (0.5 sLpm) and directly measured $[\text{H}_2\text{SO}_4]$ over a broader range of temperatures (0–40 °C), also concluding that the carrier gas is saturated with sulfuric acid under these conditions. Gas-phase NH_3 and DMA were generated with two permeation tube systems. Each consisted of a mass flow controller that passed $100 \text{ cm}^3 \text{ min}^{-1}$ of N_2 through a glass tube holding a permeation tube (VICI AG International) containing liquid NH_3 (Aldrich, 99.99%) or DMA (Aldrich, 99%). The permeation tubes were both kept at 30 °C to ensure constant permeation rates. The NH_3 and DMA flows were directed into an active dilution system that mixed the sample with purified air to achieve the desired concentration (?). Concentrations of DMA and NH_3 were determined from the dilution factor and permeation rates, the latter of which were gravimetrically calibrated over 3-6 months. Purified air (2.9 sLpm) was generated from compressed dry air with a zero air generator (Aadco, model 737-12). Water

vapor was introduced into the flow tube by passing the dry purified air through a flask containing 60 °C nanopure water ($> 18 \text{ M}\Omega$) followed by a saturator. The saturator was water jacketed and maintained at a constant temperature to control RH in the flow tube. A dew point monitor (General Eastern, model M3) was placed downstream of the flow tube to measure RH.

For the DMA + H₂SO₄ experiments, initial concentrations of H₂SO₄ and DMA were estimated to be 2.5×10^{10} and $8.9 \times 10^{10} \text{ cm}^{-3}$, respectively, under both dry and humid conditions. For the NH₃ + H₂SO₄ experiments, initial concentrations of H₂SO₄ and NH₃ were estimated to be 1.3×10^{10} and $2.5 \times 10^{12} \text{ cm}^{-3}$, respectively, under both dry and humid conditions. The initial gas phase acid:base ratio was below bulk sample thermodynamic equilibrium values of 1:2 (i.e., excess base was always present) in both DMA + H₂SO₄ and NH₃ + H₂SO₄ experiments. The total flow rate through the flow tube was 4 sLpm, resulting in an average residence time of 82 sec. It should be noted that additional wall losses occur within the flow tube for both H₂SO₄ (most likely, irreversible) and base compounds (possibly irreversible due to reactive uptake by adsorbed H₂SO₄). Based on a prior study that employed a flow tube with a similar diameter but twice the length and twice the flow rate so therefore with similar residence time (Brus et al., 2010), we estimate total wall loss of H₂SO₄ to be 50 — 66% of the initial concentration over the entire length of the flow tube.

The size distribution of particles emerging from the flow tube was measured continually with a scanning mobility particle sizer (SMPS) consisting of a nano-differential mobility analyzer (nano-DMA; model 3085, TSI, Inc.) and a butanol-based ultrafine condensation particle counter (CPC; model 3025, TSI, Inc.). The minimum detectable diameter of the CPC, as reported by the manufacturer for 50% detection efficiency, is $\sim 2.5 \text{ nm}$.

2.3.2 Nanoparticle Composition Measurements

A Thermal Desorption Chemical Ionization Mass Spectrometer (TDCIMS) was used to measure the size resolved chemical composition of newly formed particles. The instrument has been previously described in detail (Voisin et al., 2003; Smith et al., 2004; Lawler et al., 2014). Briefly, aerosol par-

ticles were sampled continually from the flow tube reactor at 1.5 L min^{-1} . Particles in the sampled flow were charged by a unipolar charger (UPC) (Chen and Pui, 1999; McMurry et al., 2009). The charged particles were then size-selected by a nano-DMA and collected by electrostatic deposition onto a Pt filament. The collection potential of the filament was set to 4000 VDC. The collection time ranged from 30–120 min, depending on particle concentration and collection efficiency. After collection, the Pt filament was translated into the ionization region of the mass spectrometer, where the filament was resistively heated under atmospheric pressure from room temperature to $\sim 550 \text{ }^\circ\text{C}$ to desorb and/or decompose particle-phase species. The volatilized molecules were ionized by chemical ionization and detected using a high-resolution time-of-flight mass spectrometer (HTOF; Tofwerk AG). The heating of the Pt filament was programmed to be at constant ambient temperature for the first 10 s, ramp up to $\sim 550 \text{ }^\circ\text{C}$ for the next 40 s, maintain at $\sim 550 \text{ }^\circ\text{C}$ for 15 s, and then return to ambient temperature for 5 s. The timespan of the heating cycle was 70 s for each collected sample. The filament and the ionization region were continually purged with N_2 to minimize contamination. Instrument background was assessed after each collection by performing the same procedure but without applying a collection potential to the Pt filament. The TDCIMS can operate in either positive or negative ion mode, and only one polarity can be monitored for each collection. Base-related species were detected in positive ion mode, and H_2SO_4 -related species in negative ion mode. Chemical ionization reagent ions were generated directly in the ion source using a ^{210}Po source. Trace amounts of H_2O and O_2 in the N_2 flow formed $(\text{H}_2\text{O})_n\text{H}^+$ and $(\text{H}_2\text{O})_n\text{O}_2^-$, which served as reagent ions in positive and negative ion modes (with $n = 1 - 3$), respectively. All ion signals reported were corrected for the background and normalized to reagent ion abundance. The TDCIMS data are presented as sums of background-corrected, detected ions integrated over the whole desorption period for each collected sample. The TDCIMS was periodically calibrated using laboratory generated, 20 nm diameter dimethylammonium sulfate (DMAS) and ammonium sulfate (AS) particles. The DMAS and AS particles were generated by atomizing dilute DMAS and AS solutions, respectively, using a constant output atomizer (model 3076; TSI, Inc.). The DMAS solution was made by stoichiometrically mixing DMA (Aldrich, 40 wt. % in water) and H_2SO_4 (Fisher Scientific, 96.2%) in nanopure water. The AS solution was made by dissolving ammonium sulfate (Alfa Aesar, 99%) powder in nanopure water. Acid:base ratios for particles generated dur-

ing the flow tube experiments were determined by comparing the measured ion ratios with those of atomized DMAS and AS particles. For the atomized particles, we assign TDCIMS-measured acid:base ratio to the ratio corresponding to fully neutralized salts (0.5). We have confirmed that 20 nm diameter AS particles were close to fully neutralized with an acid:base ratio of $\sim 0.60 \pm 0.05$ by performing ion chromatography on particle samples that were atomized and then collected on aluminum foil disks using a sequential spot sampler (model SSS110, Aerosol Devices, Inc.).

2.3.3 Model Description

A series of calculations were performed to provide a mechanistic explanation for the TDCIMS-based observations. Neutral and ionized fractions of acid and base at thermodynamic equilibrium were estimated by numerically solving a system of non-linear equations including: mass balance, electroneutrality, and acid dissociation (K_a). Activity coefficients of both the ionic and neutral species were neglected. While consideration of activity coefficients would change the absolute pH values and ratios presented, it would not change the conclusions regarding the likely mechanisms responsible for the observed acid:base ratios. Further, realistic consideration of activity coefficients requires knowledge of the dielectric constant of the solvent, which is arguably unknown in these particles. A bulk aqueous solution was assumed for the base case calculations, thus pK_a values for H_2SO_4 , NH_3 , and DMA in water were used (Barsanti et al. (2009) and references therein). For the H_2SO_4 - NH_3 base case, a comparison of our results with those obtained using the online Extended Aerosol Inorganics model (Clegg et al.; Wexler and Clegg, 2002), the latter of which includes activity coefficient corrections, demonstrates $<1\%$ difference in calculated moles of the major ions (SO_4^{2-} , NH_4^+). The activity coefficients of the neutral species were close to unity in the aqueous solution, while the activity coefficients of the ionic species were <1 . Sensitivity cases were also explored for both H_2SO_4 - NH_3 and H_2SO_4 -DMA, in which the pK_a values and acid:base ratios were varied to represent deviations in acid dissociation equilibria from a bulk aqueous solution.

2.4 Results and Discussion

2.4.1 Size Distributions of H₂SO₄-DMA and H₂SO₄-NH₃ Nanoparticles

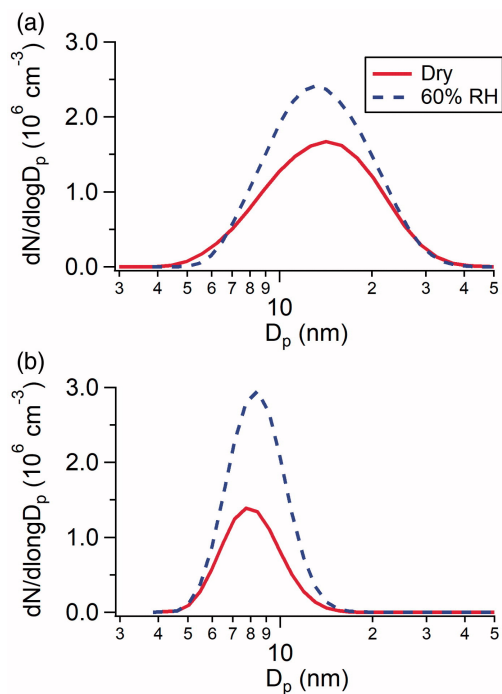


Figure 2.2: Size distributions of particles measured by SMPS from the reactions of (a) $2.5 \times 10^{10} \text{ cm}^{-3}$ H₂SO₄ with $8.9 \times 10^{10} \text{ cm}^{-3}$ DMA, and (b) $2.5 \times 10^{10} \text{ cm}^{-3}$ H₂SO₄ with $1.3 \times 10^{12} \text{ cm}^{-3}$ NH₃ under dry conditions and at 60% RH.

Figure 2.2 shows size distributions of H₂SO₄-DMA (Fig. 2.2a) and H₂SO₄-NH₃ (Fig. 2.2b) particles generated in the flow tube. The reactions of H₂SO₄ with DMA or NH₃ effectively formed particles under both dry conditions and at 60% RH. Particles were formed in the diameter range of 4-40 nm with a geometric mean mobility diameter of 13.5 nm in the H₂SO₄-DMA system, and in the diameter range of 3-18 nm with a geometric mean mobility diameter of 8.5 nm in the H₂SO₄-NH₃ system. Compared to the dry conditions, the presence of water vapor enhances particle number concentration by a factor of 1.3 and 2.1 for the H₂SO₄-DMA and H₂SO₄-NH₃ systems, respectively, suggesting that water plays an important role in particle nucleation. Although H₂SO₄-base particles are highly hygroscopic, the diameters of particles generated under humid conditions do not show significant

increases compared with those formed under dry conditions. The similarity in the measured particle size distributions under dry and humid conditions most likely represents the competition of gas-phase precursors between nucleation and nanoparticle growth. Higher levels of H_2SO_4 and base participating in nucleation under humid conditions resulted in fewer precursors available in the flow tube for nanoparticle growth.

The enhancing effect of water on nucleation has previously been observed in laboratory experiments in the H_2SO_4 -base systems (Berndt et al., 2010; Erupe et al., 2011; Zollner et al., 2012; Yu et al., 2017). Theoretical calculations showed that some clusters in the H_2SO_4 - NH_3 and H_2SO_4 -DMA systems are stabilized by water, and could be more important in cluster growth pathways (Loukonen et al., 2010; Henschel et al., 2014). However, an inhibiting effect of water vapor on NPF has been postulated to explain field observations (Sihto et al., 2006; Laaksonen et al., 2008), presumably caused by other indirect effects. For example, combining field measurements and aerosol dynamics model simulations, Hamed et al. (2011) attributed the inhibiting effect of water on NPF to the fact that solar radiation, which drives photochemistry and leads to H_2SO_4 formation, usually peaks at noon when RH is low.

The formation and growth of particles in the flow tube were very stable (see Appendix A, Figure A.1). This enabled us to continually collect particles to explore their size-resolved chemical composition over a long period of time. The results of these size-resolved composition measurements are presented next.

2.4.2 Ions Detected by TDCIMS and Their Desorption Profiles

Particles collected onto the Pt filament started to desorb as the temperature of the filament was ramped from ambient temperature to $\sim 550^\circ\text{C}$. Figure 2.3 shows desorption profiles of ions in negative and positive ion modes during typical heating cycles for particle samples collected from the H_2SO_4 -DMA (Fig. 2.3a) and H_2SO_4 - NH_3 (Fig. 2.3b) systems. For both systems, ions including SO_3^- , HSO_4^- , and SO_5^- appeared in the negative ion mode as the temperature of the Pt filament increased.

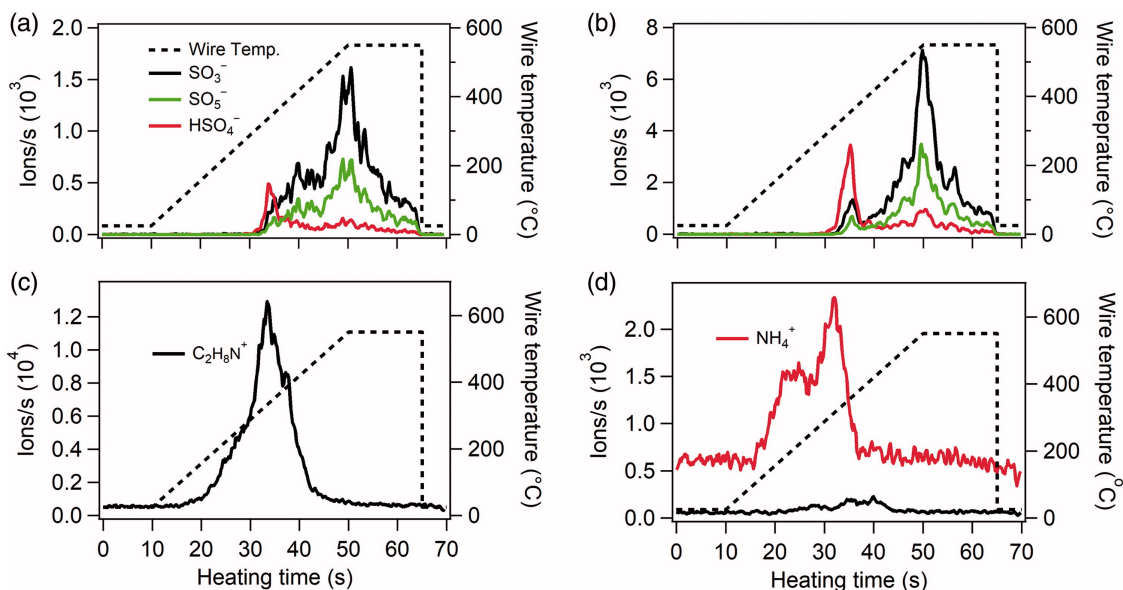


Figure 2.3: Typical desorption profiles of ions formed by heating H_2SO_4 -DMA (a, c) and H_2SO_4 - NH_3 (b, d) particles collected on the Pt filament. The top panels show ions collected in the negative ion mode. The lower panels show ions collected in the positive ion mode. The dashed lines show the evolution of the filament temperature.

Ion intensities increased with time due to the increasing temperature of the Pt filament, and then decreased due to the sample depletion. All of the detected negative ions show multiple peaks throughout the thermal evolution of the collected samples. The HSO_4^- ions first appeared at lower temperature, and this early peak is likely attributable to sulfuric acid. Detected HSO_4^- ions later in the desorption arise from a combination of H_2SO_4 re-volatilization from the ion source walls and further decomposition of salts on the wire, the latter of which is described in detail by Kiyoura and Urano (1970). Overall, HSO_4^- was a minor component of the late desorption products. The SO_3^- ion dominated the later generated ions as the Pt filament was ramped to a higher temperature, followed by SO_5^- formed from the reaction of SO_3 with the reagent ion O_2^- . Later generated ions of SO_3^- and SO_5^- showed similar desorption patterns, and they are attributed to the thermal decomposition of sulfate salts. Desorption profiles of atomized DMAS and AS particles in the calibration experiments are shown in Figure A.2 for comparison. Ions including SO_3^- , SO_5^- , and HSO_4^- were observed in the negative ion mode in the calibration TDCIMS spectra. Their desorption profiles are similar to particles generated in the flow tube.

Dimethylammonium ($\text{C}_2\text{H}_6\text{NH}_2^+$ or DMAH^+) and ammonium (NH_4^+) ions were detected as the main ions in the positive ion mode in the H_2SO_4 -DMA (Fig. 2.2a) and H_2SO_4 - NH_3 (Fig. 2.2b) systems, respectively. An elevated level of NH_4^+ was observed even before heating the Pt filament, suggesting that NH_4^+ started to desorb from particle samples immediately after the Pt filament was moved into the ionization region, whose surfaces were kept at 60°C to reduce partitioning of semivolatile compounds. While NH_4^+ was observed before heating the Pt filament for particles formed in the H_2SO_4 - NH_3 system, atomized AS particles used for calibration showed a similar trend (Figure A.2a). Since both experiment and calibration analyses were conducted under identical operating conditions, we omitted NH_4^+ ions produced prior to the heating of the Pt filament in our calculation of total ion signal.

Trace amounts of DMAH^+ were observed as a contaminant in H_2SO_4 - NH_3 particles, and did not disappear even after the TDCIMS inlet system was thoroughly cleaned. Atomized AS particles (Figure A.2b) showed no significant DMAH^+ , indicating that the contaminant was not from the TDCIMS inlet system, but from gas-phase DMA residue adsorbed on walls of the flow tube from earlier H_2SO_4 -DMA experiments. The DMAH^+ signal was $\sim 10\%$ of the NH_4^+ signal, and did not show a clear dependence on particle size. Given that the TDCIMS has higher sensitivity to DMAH^+ than to NH_4^+ (Figure A.2c), the lower intensity of the DMAH^+ signal indicates that the presence of this ion does not significantly impact the interpretation of our measurements.

2.4.3 Acid:base Ratio H_2SO_4 - NH_3 and H_2SO_4 -DMA Nanoparticles

Figure 2.4 shows size-resolved acid:base ratio of H_2SO_4 -DMA particles formed under dry conditions and at 60% RH in excess of DMA. The acid:base ratio of H_2SO_4 -DMA particles at 8.6 nm formed under dry conditions is 0.7 ± 0.1 ; all ratios presented here are averages and the uncertainties are represented by the standard deviation obtained from repeated experiments. The ratio decreases as size increases, reaching a minimum of ~ 0.2 at 10.6 nm, and then increases again with increasing particle size until the neutralized state is reached (acid:base ratio = 0.5). An acid:base ratio of 0.2 suggests that excess DMAH^+ was present in the 10.6 nm H_2SO_4 -DMA particles. The acid:base

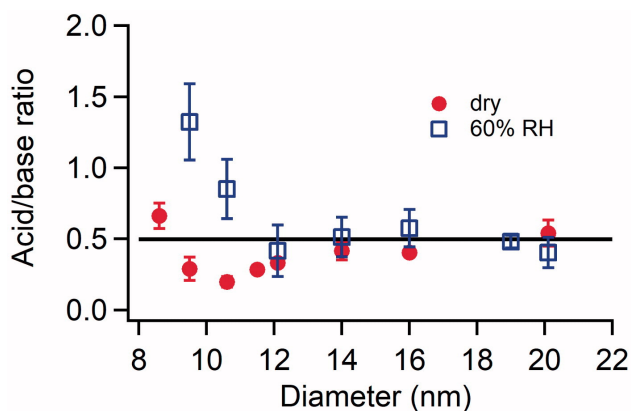


Figure 2.4: Size resolved acid:base ratio of newly formed particles in the H_2SO_4 -DMA system under dry conditions and at 60% RH. The concentrations of H_2SO_4 and DMA introduced into the flow tube reactor were $2.5 \times 10^{10} \text{ cm}^{-3}$ and $8.9 \times 10^{10} \text{ cm}^{-3}$, respectively, for both the dry conditions and at 60% RH. The error bars represent standard deviations of at least three repeated measurements. The horizontal black line represents the acid:base ratio of fully neutralized H_2SO_4 -DMA particles.

ratio for 20 nm particles was 0.5 ± 0.1 , indicating that particles became fully neutralized once they grew to 20 nm under dry conditions. Particles formed at 60% RH show a different trend compared to those formed under dry conditions. Smaller particles at 9.5 nm were acidic, showing an acid:base ratio of 1.3 ± 0.3 . The ratio rapidly decreases with size, and reaches ~ 0.5 at 12 nm. Particles larger than 12 nm were fully neutralized by DMA.

To further explore the size-dependent acid:base ratio of H_2SO_4 -DMA particles, the ratios of different negative ions integrated over the desorption period were compared as shown in Figure 2.5. Total ions of SO_3^- and SO_5^- are linearly correlated, showing a $\text{SO}_3^-:\text{SO}_5^-$ ratio of ~ 0.44 regardless of particle size. The good linear correlation of SO_3^- and SO_5^- suggests their common sources, i.e. the thermal decomposition of sulfate salts as discussed earlier. The $\text{HSO}_4^-:\text{SO}_3^-$ ratio, however, shows a strong dependence on size. The ratio decreases with size in the size range of 8.6-14 nm, and increases with size in the size range of 14-21 nm. While HSO_4^- was mainly from particle-phase H_2SO_4 and/or bisulfate salts, the higher $\text{HSO}_4^-:\text{SO}_3^-$ ratio indicates that the smallest particles contain more H_2SO_4 and/or bisulfate salts, which decrease and then increase as particles grow. The trend is qualitatively similar to the size-dependent acid:base ratio shown in Figure 2.4 and provides a possible explanation for the observed variability.

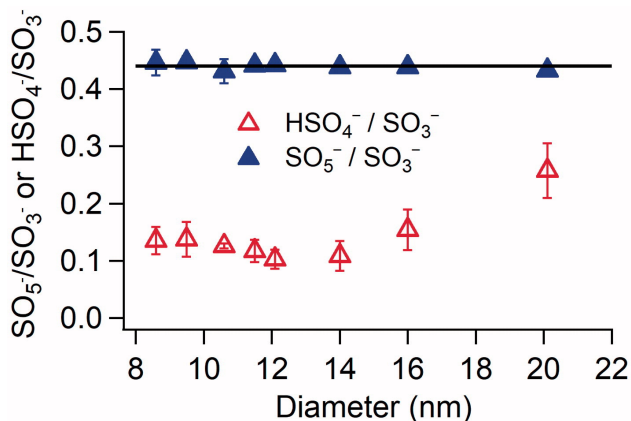


Figure 2.5: Ratios of $\text{SO}_5^-:\text{SO}_3^-$ and $\text{HSO}_4^-:\text{SO}_3^-$ as a function of particle size for newly formed particles in the H_2SO_4 -DMA system under dry conditions. The concentrations of H_2SO_4 and DMA introduced into the flow reactor were $2.5 \times 10^{10} \text{ cm}^{-3}$ and $8.9 \times 10^{10} \text{ cm}^{-3}$, respectively. The error bars represent standard deviations of at least three repeated measurements. The horizontal black line represents a $\text{SO}_5^-:\text{SO}_3^-$ ratio of 0.44.

The size-resolved acid:base ratio of $\text{H}_2\text{SO}_4\text{-NH}_3$ particles generated under dry conditions and at 60% RH are shown in Figure 2.6. For both the dry conditions and 60% RH, 7 nm diameter $\text{H}_2\text{SO}_4\text{-NH}_3$ particles were highly acidic, showing an acid:base ratio that ranged from 3.1 ± 0.6 to 3.4 ± 0.3 . The ratio gradually decreased as particles grew from 7 nm to 12 nm, reaching ~ 2 and ~ 1 for 12 nm particles generated under dry conditions and at 60% RH, respectively. Unlike $\text{H}_2\text{SO}_4\text{-DMA}$ particles shown in Figure 4, $\text{H}_2\text{SO}_4\text{-NH}_3$ particles did not reach bulk sample thermodynamic equilibrium even for particles at the largest size collected in the experiment. Particles generated in the $\text{H}_2\text{SO}_4\text{-NH}_3$ system were much smaller than those generated in the $\text{H}_2\text{SO}_4\text{-DMA}$ system (Fig. 2.2), and may not have grown enough to reach bulk sample thermodynamic equilibrium for the experimental conditions that were employed in this study.

For both $\text{H}_2\text{SO}_4\text{-DMA}$ and $\text{H}_2\text{SO}_4\text{-NH}_3$ systems, the TDCIMS results indicate that smallest particles generated either under dry conditions or at 60% RH were acidic and did not reach a fully neutralized state even in excess of base. The base fraction in particles increased with size, but incorporation of base into particles shows different trends among individual experiments under different conditions.

It is important to consider the potential role that particulate water may play in these experiments. At 60% RH, $\text{H}_2\text{SO}_4\text{-NH}_3$ nanoparticles always contain liquid water since their measured acid:base

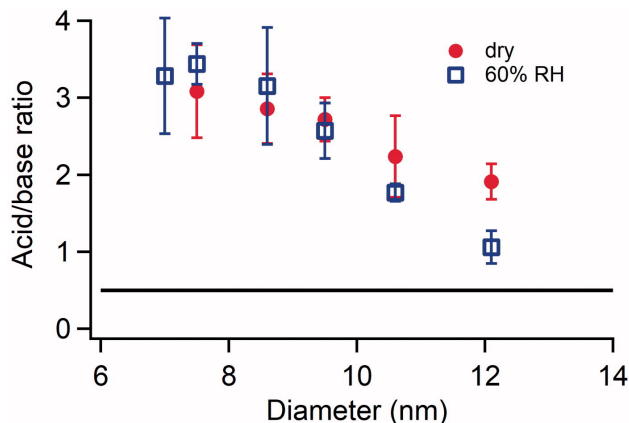


Figure 2.6: Size resolved acid:base ratio of newly formed particles formed in the $\text{H}_2\text{SO}_4\text{-NH}_3$ system under dry conditions and at 60% RH. The concentrations of H_2SO_4 and NH_3 introduced into the flow tube reactor were $2.5 \times 10^{10} \text{ cm}^{-3}$ and $1.3 \times 10^{12} \text{ cm}^{-3}$, respectively, for both the dry conditions and 60% RH. The error bars represent standard deviations of at least three repeated measurements. The horizontal black line represents the acid:base ratio of fully neutralized $\text{H}_2\text{SO}_4\text{-NH}_3$ particles.

ratio is greater than that of ammonium bisulfate, the latter of which has a deliquescence RH of 40% (Tang and Munkelwitz 1977). As $\text{H}_2\text{SO}_4\text{-NH}_3$ particles become more acidic, they increase in hygroscopicity and the deliquescence point eventually disappears completely. It is therefore possible that some $\text{H}_2\text{SO}_4\text{-NH}_3$ particles may contain residual water even under “dry” conditions. In contrast, experiments with $\text{H}_2\text{SO}_4\text{-DMA}$ particles show no clear deliquescence point over all observed acid:base ratios. Micron-sized particles with acid:base of 1:2 show a 50 - 75% increase in mass when exposed to 60% RH, and particles may contain some residual water at sub-3% RH (Chan and Chan, 2013; Rovelli et al., 2017). Unlike the $\text{H}_2\text{SO}_4\text{-NH}_3$ system, an ammonium bisulfate particle is slightly less hygroscopic than its sulfate counterpart (Sauerwein et al., 2015). In summary, under “dry” conditions particles from both systems may contain some residual water that may depend on acid:base ratio, whereas at 60% RH they likely contain significant water over all observed acid:base ratios.

During particle collection, particle-phase bases may be preferentially lost from the Pt filament compared to particle-phase H_2SO_4 . This would lead to artificially high acid:base ratios. To investigate this possible artifact, a control experiment was carried out in which the collection time of particles was varied for the same size of $\text{H}_2\text{SO}_4\text{-DMA}$ particles. This method was used previously to de-

termine particulate compounds that were of intermediate volatility for nanoparticles generated by α -pinene ozonolysis (Winkler et al., 2012). The TDCIMS signals for both negative and positive ions showed a linear correlation with collection time (Fig. A.3), suggesting that losses of particle-phase H_2SO_4 and base from the Pt filament are minimal. Previous studies on ammonium or dimethylammonium sulfate aerosols also showed that the TDCIMS does not exhibit a strong tendency to lose bases prior to analysis (Lawler et al., 2016).

Another potential artifact that would affect observed acid:base ratios is that particles collected on the Pt filament were contaminated by H_2SO_4 that desorbed from the walls of the TDCIMS inlet system. However, the H_2SO_4 signal did not significantly change even after the TDCIMS inlet system was thoroughly cleaned. TDCIMS data for the calibration aerosol particles did not show any indication of H_2SO_4 contamination. We therefore conclude that contamination of H_2SO_4 was not an issue in the TDCIMS analysis.

The experimental evidence presented above supports the observation that the growth of nanoparticles above 3 nm differs from that of H_2SO_4 -base clusters, which were proposed to grow through a stepwise addition of H_2SO_4 and base molecules (Kirkby et al., 2011; Almeida et al., 2013a; Bianchi et al., 2014; Schobesberger et al., 2013; Kürten et al., 2014; Schobesberger et al., 2015b). The size-dependent acid:base ratio of particles is consistent with previous observations in the CLOUD7 experiments (Kim et al., 2016; Lawler et al., 2016). The heterogeneous oxidation of SO_2 (the H_2SO_4 precursor introduced into the CLOUD chamber) was offered as a possible explanation for the high H_2SO_4 in small particles in previous CLOUD7 experiments (Lawler et al., 2016). In this study however, gas-phase H_2SO_4 was directly introduced into the flow tube, ruling out such a source of aerosol mass.

If oxidative kinetics is not the reason for the unexpected acid:base ratios, other factors must explain the deviations of the newly formed nanoparticles from bulk solution chemistry. One possibility is a kinetic limitation for the uptake of ammonia or amine. There is some evidence for the presence of an activation barrier to ammonia incorporation in charged clusters of ammonium and sulfate (Bzdek et al., 2013). While such a barrier for nanoparticles may explain their high acidity, it

does not explain the size dependence of the acid:base ratio. In addition, thermodynamic modeling presented below suggests that a mere reduction in particulate base cannot explain the size-dependent behavior of the $\text{HSO}_4^-:\text{SO}_3^-$ ratio. Finally, the effect of an activation barrier to uptake would be most apparent when concentrations of base and sulfuric acid were of similar magnitude, whereas for our experiments with ammonia and sulfuric acid the ammonia concentrations exceeded sulfuric acid levels by two orders of magnitude.

Aerosol phase state is known to play a major role in the equilibrium particle composition reached in systems of amines, ammonia, and sulfuric acid, due to the much more facile exchange for liquid particles compared with solid particles. In a study of micron-sized dimethylammonium sulfate particles, the experimental study by Chan and Chan (2013) found that these particles were in a liquid phase, even at sub-3% RH. Cheng et al. (2015) highlighted the challenge of predicting the phase of aerosol nanoparticles, and concluded that below some threshold size (dependent on material, temperature, and water content) nanoparticles will be liquid. Specifically, their measurements of particle hygroscopicity suggested that ammonium sulfate nanoparticles are “molten” in the diameter range of 4–10 nm, depending on assumptions regarding the amount of residual particulate water. Lawler et al. (2016) applied the assumption that nanoparticles formed in the ammonia-dimethylamine-sulfuric acid system were liquid and presented arguments for why a liquid phase may result in the measurement of more acidic nanoparticles. In the following section we similarly assume the present particles are “aqueous,” a term that we interpret as meaning a liquid state with varied amounts of residual water. With this assumption, we explore the possible roles of deviations of acid dissociation constants from bulk behavior using theoretical modeling.

2.4.4 Thermodynamic Modeling of $\text{H}_2\text{SO}_4\text{-NH}_3$ and $\text{H}_2\text{SO}_4\text{-DMA}$ Nanoparticles

The use of aqueous acid dissociation constants to describe thermodynamic equilibrium in the experimental systems may be insufficient, leading to the deviation between the observed size-dependent acid:base ratio and predictions based on bulk aqueous theory. It is known that individual pK_a

values vary with ionic strength and solvent dielectric constant (Reijenga et al., 2013; Farrokhpour and Manassir, 2014; Hartono et al., 2014). Both ionic strength and solvent dielectric constant likely are size-dependent, as they depend on the amount of condensed-phase water and other components present in particles. Changes in electrostatic interactions, polarization, charge delocalization, and mixing state in nanoparticles may also lead to deviations in effective pK_a values from bulk aqueous values.

Table 2.1: Thermodynamic modeling of $\text{H}_2\text{SO}_4\text{-NH}_3$ and $\text{H}_2\text{SO}_4\text{-DMA}$ particles.

	Model settings					Model results			
	Acid:Base ^a	Base	$\text{pK}_{a1}, \text{H}_2\text{SO}_4$	$\text{pK}_{a2}, \text{H}_2\text{SO}_4$	pK_a, base	pH	$[\text{HSO}_4^-] + [\text{SO}_4^{2-}] / [\text{BH}^+]$ ^b	$[\text{SO}_4^{2-}] / [\text{HSO}_4^-]$	$[\text{BH}^+] / C_B$ ^c
Base Case	1:2	NH_3	-3	2	9.25	4	0.5	99	1
		DMA	-3	2	10.73	4.58	0.5	335	1
Sensitivity Case I	1:2	NH_3	0.5	5.5	5.75	5.36	0.7	0.73	0.71
		DMA	0.5	5.5	7.23	6.23	0.55	5.4	0.91
Sensitivity Case II	2:1	NH_3	0.5	5.5	5.75	0.78	1.3	< 1	< 1
		DMA	0.5	5.5	7.23	0.79	1.3	< 1	< 1

^aRatio of acid:base in particle phase

^b BH^+ represents the protonated form of the corresponding base B

^c C_B represents total bulk concentration of the base in particles

Descriptions of the thermodynamic modeling cases and the results are shown in Table 2.1. In the Base Case and Sensitivity Case I, the acid:base ratio was assumed to be 0.5 to allow a fully neutralized solution and gas/particle partitioning was neglected. Relative to the Base Case, the pK_a values were modified by 3.5 units in Sensitivity Case I, such that the H_2SO_4 becomes less acidic (pK_a value increases by 3.5) and the bases become less basic (pK_a value decreases by 3.5). Changing the pK_a values accounts for the possibility of strongly inhibited proton transfer in nanoparticles due to steric or mixing effects. Compared to the Base Case, modifying the pK_a values of the acid and the bases by 3.5 units results in an increase in the ratio of acidic to basic ions ($([\text{HSO}_4^-] + [\text{SO}_4^{2-}]) : [\text{BH}^+]$), and a decrease in the ratio of $\text{SO}_4^{2-}:\text{HSO}_4^-$ (Sensitivity Case I, Table 1). The deviation in the ratio of $([\text{HSO}_4^-] + [\text{SO}_4^{2-}])$ to $[\text{BH}^+]$ is greater in $\text{H}_2\text{SO}_4\text{-NH}_3$ particles than $\text{H}_2\text{SO}_4\text{-DMA}$ particles. These modeling results reflect the observed trends in the laboratory measurements.

The ratio of protonated form of base to the total base ($[\text{BH}^+] : C_B$) in Sensitivity Case I (Table 1) were less than 1, indicating the presence of neutral bases in the condensed phase. However, the relatively high Kelvin-corrected vapor pressures of NH_3 and DMA preclude their presence as neutral compounds in nanoparticles. Thus, in Sensitivity Case II, the relative concentration of acid:base was assumed to be 2:1 to reflect the decreased availability of base that partitions from

the particle phase to the gas phase. In Sensitivity Case II, the ratio of $([\text{HSO}_4^-] + [\text{SO}_4^{2-}]) : [\text{B}^+]$ further increases, and the ratio of $\text{SO}_4^{2-}:\text{HSO}_4^-$ decreases, moving towards better agreement with laboratory measurements.

In summary, the model best represents the laboratory measurements when: (1) the acid and the bases are assumed to be less efficient at acid-base chemistry (represented by a change in pK_a values of 3.5 units); and (2) the fraction of the base in its neutral form is allowed to partition back to the gas phase and is no longer available to participate in acid-base chemistry. These could be the reasons for the strong size-dependent composition gradient of H_2SO_4 -base nanoparticles observed in the experiments.

2.5 Conclusions

In summary, we measured size-resolved chemical composition of newly formed particles in H_2SO_4 - NH_3 and H_2SO_4 -DMA systems using Thermal Desorption Chemical Ionization Mass Spectrometry. A strong size-dependent acid:base ratio in these particles was found, consistent with previous observations in the CLOUD7 experiments (Kim et al., 2016; Lawler et al., 2016). Smaller particles were generally more acidic and did not reach bulk sample thermodynamic equilibrium even in excess of gas-phase base. The acidity of particles decreased as particles grew to larger size, but the incorporation of base into particles varied with base species, relative humidity and particle size. Particles reached a fully neutralized state as they grew to 12 nm in the case of DMA. In contrast, 12 nm particles from generated from H_2SO_4 - NH_3 were still highly acidic. Model results suggest that acid-base chemistry may be less efficient in nanoparticles than in bulk aqueous solutions. Modifying pK_a values of H_2SO_4 and base by 3.5 units resulted in more acidic particles, leading to results consistent with observations. Due to the less efficient acid-base chemistry, a larger fraction of particle-phase base species are present relatively volatile neutral molecules, allowing them to partition into the gas phase and resulting in acidic particles.

Our results suggest that small newly formed particles whose growth are driven by acid-base chemistry are acidic, which in turn affects physicochemical properties of particles like hygroscopicity and mixing states. These acidic particles can enhance acid-catalyzed uptake of organics (Jang et al., 2002), oligomerization of organics within particles (Holmes and Petrucci, 2006), and other gas uptake pathways that contribute to particle growth. The size-dependent acidity together with the Kelvin effect and the potential phase transition of nanoparticles complicates the growth process of particles. While bulk phase solution thermodynamics provides insights into the underlying causes of the observed size-dependence of acid:base ratios of H_2SO_4 -DMA and H_2SO_4 - NH_3 particles, it does not allow us to determine the underlying causes of the interesting local minimum in the size-dependent acid:base ratio of particles generated by the DMA- H_2SO_4 system under dry conditions. This will be the subject of future experimental and modeling work.

Chapter 3

An Experimental and Modeling Study of Nanoparticle Formation and Growth from Dimethylamine and Nitric Acid

3.1 Abstract

The size-resolved composition of nanoparticles formed and grown through acid-base reactive uptake has been studied in the laboratory by reacting gas-phase nitric acid (HNO_3) and dimethylamine (DMA) in a flow tube under dry ($< 5\%$ RH) and humid ($\sim 55\%$ RH) conditions. Size-resolved nanoparticle composition was measured by a Thermal Desorption Chemical Ionization Mass Spectrometer (TDCIMS) over the diameter range of 9–30 nm. Nanoparticle geometric mean diameter

Reproduced with permission from Chee, S., Myllys, N., Barsanti, K. C., Wong, B. M., and Smith, J. N.: An Experimental and Modeling Study of Nanoparticle Formation and Growth from Dimethylamine and Nitric Acid, *J. Phys. Chem. A*, 123, 5640–5648, <https://doi.org/10.1021/acs.jpca.9b03326>, 2019. Copyright 2019 by the American Chemical Society.

grew in the presence of water compared to dry conditions. Acid:base ratios of HNO₃-DMA particles at all measured sizes did not strongly deviate from neutral (1:1) in either RH condition, which contrasts with prior laboratory studies of nanoparticles made from sulfuric acid (H₂SO₄) and base. Theoretical methods were used to investigate the underlying chemical processes that explain observed differences in the composition of HNO₃-DMA and H₂SO₄-DMA particles. Calculations of HNO₃-DMA cluster stability indicated that a 1:1 acid:base ratio has $>10^7$ smaller evaporation rates than any other acid:base ratio in this system, and measured nanoparticle composition confirm this to be the most stable pathway for growth up to 30 nm particles. This study demonstrates that nanoparticle formation and growth via acid-base reactive uptake of HNO₃ and DMA follows thermodynamic theory, likely because of both components' volatility.

3.2 Introduction

New particle formation (NPF) events are a large contributor to the global population of cloud condensation nuclei (CCN) (Kuang et al., 2009; Zhang et al., 2012), which can affect climate and precipitation by influencing cloud formation. However, the growth processes for nanoparticles (< 100 nm in diameter) formed from these NPF events are not well understood (Zhang et al., 2012). At these sizes, the Kelvin effect reduces the number of gases that can contribute to nanoparticle growth by condensation (Finlayson-Pitts and Pitts, 2000). Sulfuric acid is the most studied contributor to nanoparticle growth (Chan and Mozurkewich, 2001; Schobesberger et al., 2015a; Elm, 2017a; Zollner et al., 2012; Bzdek et al., 2012; Sipilä et al., 2010; Weber et al., 1995; Kuang et al., 2008; Kirkby et al., 2011; Almeida et al., 2013a; Weber et al., 1996) because of its extremely low volatility and high acidity; however, it has been observed that concentrations of sulfuric acid alone cannot explain all nanoparticle formation and growth alone (Weber et al., 1995; Kirkby et al., 2011; Weber et al., 1996). Measurements of nanoparticle composition at several field studies supports this observation, where organic species, nitrate, and ammonium ions have been detected in coexistence with sulfate in nanoparticles (Smith et al., 2008a, 2010a; Lawler et al., 2014).

Acid-base chemistry as a mechanism of reactive uptake into particles, while conceptually simple,¹⁸ is still poorly understood when applied to the formation and growth of clusters and nanoparticles. Clusters of sulfuric acid and ammonia/amines have been measured, and have been observed to grow stepwise with sulfuric acid adding first, followed by the addition of base (Kirkby et al., 2011; Bzdek et al., 2017; Schobesberger et al., 2013). This neutralization process implies either a 1:1 or 1:2 acid:base ratio for particles growing via acid-base reactive uptake. Recently, however, several studies have reported that particles composed of sulfuric acid and base have been observed to be more acidic in particle diameters smaller than 15 nm (Kim et al., 2016; Lawler et al., 2016), and in the specific case of H₂SO₄-DMA particles, even become more basic under dry conditions at some sizes (Chen et al., 2018). This disparity between the composition of clusters and nanoparticles in such acid-base systems warrants additional investigation. These prior studies examined trends in nanoparticle composition from reactions of bases with sulfuric acid, a low volatility, diprotic acid. This study supplements these observations with experiments and modeling of reactions of these bases with a monoprotic acid with volatility five orders of magnitude higher than sulfuric acid.

Nitric acid (HNO₃) is ubiquitous throughout the atmosphere and is typically present in low ppbv concentrations (Afpel et al., 1979; Huang et al., 2002; Cass et al., 2000). Nitrate (NO₃⁻) has been observed to be present in atmospheric particles smaller than 50 nm in diameter (Smith et al., 2008a; Lawler et al., 2014) as well as in micron-sized particles (Pakkanen, 1996; Noble and Prather, 1996). Typically, nitrate present in particles larger than 100 nm in diameter has been attributed to salt formation of primarily ammonium nitrate, and in marine areas, sodium nitrate (Finlayson-Pitts and Pitts, 2000). However, experimental studies have shown that ammonium nitrate salts are too volatile to be present in particles smaller than ~50 nm in diameter (Smith et al., 2004). It has been suggested that for these ambient particles in which the Kelvin effect is strong the detected nitrates are associated with strong bases like amines (Smith et al., 2004).

Amines have been observed both in laboratory studies and in ambient air to contribute to nanoparticle growth (Tröstl et al., 2016; Cheng et al., 2018; Chan and Chan, 2013; Chen and Finlayson-Pitts, 2017; Olenius and Riipinen, 2017; Bzdek et al., 2010). Dimethylamine (DMA) has been measured in particles down to the critical cluster size and is found to stabilize cluster formation with sulfuric

acid (H_2SO_4) molecules via salt formation (Bzdek et al., 2017; Berndt et al., 2013; Bzdek et al., 2010). However, only a few studies have investigated how nitric acid and amines may form salts to contribute to particle growth in the atmosphere (Cheng et al., 2018; Murphy et al., 2007; Sareen et al., 2017).

This study focuses on the composition and growth of dimethylammonium nitrate ($\text{HNO}_3\text{-DMA}$) nanoparticles from gas-phase reactions of dimethylamine and nitric acid. The observations and theoretical understanding obtained from this study provide insights into the potential role of these compounds in the growth of atmospheric nanoparticles. Additionally, since it has been shown previously that the composition of aerosol particles can be affected by ambient relative humidity (Sareen et al., 2017), particles were formed under both dry ($\sim 5\%$ RH) and humid ($\sim 55\%$ RH) conditions and the corresponding impact on nanoparticle composition was explored. Finally, we supplemented our experimental observations with studies of the initial steps of nitric acid and dimethylamine particle formation with and without the presence of water vapor using theoretical methods.

3.3 Experimental and Theoretical Methods

3.3.1 Particle Generation

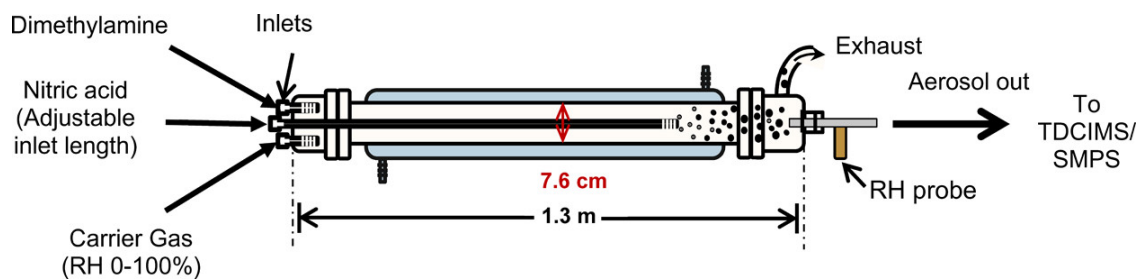


Figure 3.1: Particle generation flow tube setup.

The flow tube setup is similar to that used by Chen et al. (2018) except for changes to the nitric acid inlet. Briefly, $\text{HNO}_3\text{-DMA}$ particles were formed and grown in a 4.8 L flow tube reactor (7.5 cm diameter, 105 cm length) in a temperature-controlled room (Figure 3.1). Gas-phase nitric acid

was introduced to the reactor by flowing N_2 through a 30 cm long saturator containing aqueous nitric acid (Macron Fine Chemicals, aqueous 70%, ACS certified) and then serially diluted. The concentration of HNO_3 vapor was estimated by assuming that it achieves its saturation vapor pressure prior to exiting the saturator. The inlet for this study was altered from the Chen et al. study by the addition of a movable, 1/8" OD stainless steel tube inserted into the inlet end of the flow tube (Figure 3.1). The stainless-steel tube was capped and the gaseous nitric acid-containing N_2 entered the flow tube through slits cut out of the cap to promote mixing. Gas-phase dimethylamine (DMA) was introduced into the flow tube by flowing nitrogen over a permeation tube (VICI AG International) holding liquid DMA (Sigma Aldrich, 99%). The permeation rate of DMA was determined gravimetrically by measurement of mass loss over time, measured once each month for six months. DMA was introduced through a separate inlet at the entrance to the flow tube at $100 \text{ cm}^3 \text{ min}^{-1}$, while $100 \text{ cm}^3 \text{ min}^{-1}$ of nitric acid was introduced through the moveable injector ~ 30 cm downstream. Dry or humidified N_2 was used as the carrier gas added at a third inlet. The mixing ratios for nitric acid and dimethylamine after introduction to the flow tube were ~ 63 ppm and ~ 10 ppb, respectively. Humidification was carried out by passing N_2 through a heated flask containing nanopure water ($> 18 \text{ M}\Omega$), followed by a temperature-controlled saturator. Relative humidity was monitored by a home-built temperature and humidity sensor located downstream of the flow tube. The residence time of both gases downstream of the nitric acid inlet was ~ 40 seconds prior to sampling. Particle measurements were only taken after gases had been introduced to the system for 24 h to ensure equilibration of vapors. No significant increase in wall loss of DMA was detected between the dry and humid conditions.

The particle size distribution was measured with a scanning mobility particle sizer (SMPS), which consisted of a nano-differential mobility analyzer (nano-DMA; model 3085, TSI, Inc.) and a butanol-based mixing condensation particle counter (mCPC; model 1720, Brechtel Mfg). The 50% detection efficiency diameter limit for the CPC used was 7.0 nm, as described by the manufacturer. The sheath and excess flows of the nano-DMA were run with mass-flow controlled (Alicat Scientific) purified zero air (model 737-13, Aadco Instruments) and a flow-controlled vacuum pump, respectively. Since these flows are not recirculated, particles made from the humid system will dry, and their measured

size distribution will be more representative of the particles sampled for chemical composition analysis.

3.3.2 Nanoparticle Composition Measurements

Particles were sampled directly from the flow tube to a Thermal Desorption Chemical Ionization Mass Spectrometer (TDCIMS), which has already been described in detail (Lawler et al., 2016; Smith et al., 2004; Voisin et al., 2003). Briefly, 2 LPM of aerosol were sampled continuously from the flow tube and into the TDCIMS inlet. Particles were charged by unipolar charger (UPC) (Chen and Pui, 1999; McMurry et al., 2009) and size-selected by nano-DMA, in which the sheath flow was run with zero air to minimize contamination of the TDCIMS inlet by DMA and HNO_3 . Monodisperse particles were collected by electrostatic deposition on a Pt filament held at 3500 V. The collection time ranged from 2-360 min, depending on particle size, concentration, and collection efficiency. Once sufficient particle mass was collected onto the filament, it traveled up to the ionization region, which was held at 40 °C and flushed continuously with N_2 to prevent contamination from sample air. The filament was resistively heated from 40 to ~ 600 °C in front of the sampling orifice to the mass spectrometer to thermally desorb particle components. These components were chemically ionized by negative and positive ion mode reagent ions $(\text{H}_2\text{O})_n\text{O}_2^-$ and $(\text{H}_2\text{O})_n\text{H}_3\text{O}^+$, respectively ($n = 1-3$), which are generated via ^{210}Po radioactive source that ionizes trace oxygen and water present in a nitrogen flow. The analyte ions are then detected by a quadrupole mass spectrometer (Extrel Corp.). The thermal desorption process consisted of the following: the wire maintained ambient temperature for 60 s, ramped to ~ 600 °C over 180 s, maintained ~ 600 °C for 90 s, and then returned to ambient temperature for 60 s. The total desorption cycle was 6.5 min for each collection. Backgrounds for each sample collection were determined by operating the collection/analysis cycle identically except that a high voltage was not applied to the filament during the collection period so that particles were not collected on the filament.

Ion signal was quantified by integrating the difference between collection and background desorption profiles. To improve signal-to-noise ratio, ion data associated with the desorbed products of DMA

and HNO_3 were integrated during the region of highest desorption during analysis, 60–180 s after the start of the analysis cycle (Figure B.2). Additionally, to establish signal-to-collected-mass linearity and to ensure that no loss of particulate components occurred during sample collection, 12 nm diameter particle composition was measured after 5, 7.5, 10, 20, and 30 min of collection time (Supplementary Information, Figure B.3). Calculations of the acid:base ratio were performed by integrating the ion intensity of the detected acid ions and then dividing that by the integrated ion intensity of the detected base ions.

The TDCIMS relative sensitivity to ions associated with dimethylamine and nitric acid was calibrated by measuring the composition of atomized particles. A solution of 2 mM 1:1 HNO_3 -DMA was made from concentrated nitric acid (Macron Fine Chemicals, aqueous 70%, ACS certified), dimethylamine (Acros Organics, 40 wt% in water) and water ($> 18 \text{ M}\Omega$). This bulk solution was aerosolized using an atomizer (model 3076, TSI, Inc.) and the resulting droplets were dried with a NafionTM dryer (Perma Pure, Inc.) to form dried particles. Particles were size-selected at 30 nm diameter to overlap with the particles produced via the flow tube and analyzed identically to the flow tube reactor experiments. The resulting acid:base ratio from the atomized particles were assumed to reflect a 1:1 ratio of DMA: HNO_3 based on offline measurements of atomized particle composition.²³ These measurements were used to calibrate the acid:base ratio from the flow tube experiments.

3.3.3 Computational Methods

We explored the potential energy surface of the clusters generated from $\text{HNO}_3 + \text{DMA}$ using the ABCcluster program (Zhang and Dolg, 2015, 2016). First, we created 1000 cluster structures and used the PM7 semiempirical method (Stewart, 2007) for initial optimization and vibrational frequency calculations. Based on the obtained Gibbs free energies and dipole moments, we separated potential lowest energy conformers, which were then optimized at the $\omega\text{B97X-D/6-31+G}^*$ level of theory (Chai and Head-Gordon, 2008). For 5–10 lowest energy conformers, the $\omega\text{B97X-D/6-31++G}^{**}$ level of theory was used for the final optimization and vibrational frequency calculation (Myllys et al.,

2016b). We calculated electronic energy corrections on top of the ω B97X-D/6-31++G** structures using linear-scaling coupled cluster level at the DLPNO-CCSD(T)/aug-cc-pVTZ level of theory with tight PNO criteria (Riplinger et al., 2016; Myllys et al., 2016a). Gibbs free energies were calculated at the DLPNO-CCSD(T)/aug-cc-pVTZ// ω B97X-D/6-31++G** level, and the global minimum energy structure for each cluster was identified. All geometries were optimized and vibrational frequencies were calculated using Gaussian16 RevA.03 (Frisch et al., 2016), and electronic energy corrections were performed in Orca version 4.0.1.2 (Neese, 2012).

To study cluster formation kinetics and the dynamics of cluster populations, the calculated Gibbs free energies are used as input in the Atmospheric Cluster Dynamic Code (ACDC) (Mcgrath et al., 2012). Briefly, ACDC calculates the rate coefficients for all collision and evaporation processes within a given set of clusters and vapor molecules, and then solves the birth-death equations that describe the dynamics of the cluster population. All the Gibbs free binding energies (in kcal/mol and at 298.15 K) for the minimum energy clusters as well as the structures in xyz format are available in the Appendix B. The ACDC code is available from the authors upon request.

3.4 Results and Discussion

3.4.1 Size distributions of nanoparticles generated in dry or humid conditions

The number-size distribution of the DMA-HNO₃ particles generated from the flow tube under dry (\sim 5% RH) and humid (\sim 55% RH) conditions are shown in Figure 3.2. In each case, flow rates, reaction time, and gas precursor concentrations remained the same; the only difference was in the humidification of N₂. Dimethylamine and nitric acid reacted to form particles readily under dry conditions, and particle sizes ranged from 7–30 nm with a volume mean diameter of 16.4 nm. Under humid conditions, water vapor enhanced particle growth, with particle sizes ranging from 7 to 40 nm and the volume mean diameter increasing to 23.6 nm. The total number concentration from

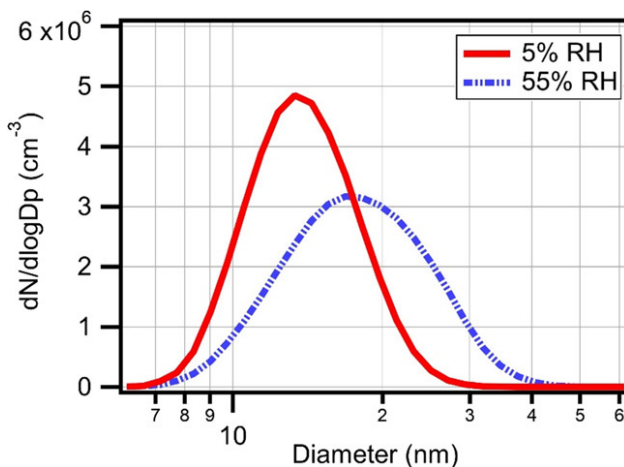


Figure 3.2: Size distribution of particles generated in dry (5% RH) and humid (55% RH) conditions.

the dry to humid case decreased by $\sim 10\%$, which has been shown in previous studies to be within error when deriving total number concentration from SMPS data (Lightstone et al., 2000). This suggests water does not enhance number concentration for these particles, despite participating in nanoparticle growth.

While the hygroscopicity of aminium nitrate salts is not well characterized in the literature, ammonium nitrate salts have been studied (Lightstone et al., 2000; Qiu and Zhang, 2012) and are observed to have a deliquescence point at 61.5% RH. Aminium sulfate and ammonium sulfate salts have been studied extensively and are found to exhibit different water uptake behaviors (Qiu and Zhang, 2012; Braban et al., 2001; Smith et al., 2008a). While ammonium sulfate deliquesces at $\sim 79\%$ RH, aminium sulfate salts experience monotonic water uptake (Qiu and Zhang, 2012). This behavior has been attributed to the possibility that aminium sulfate salts have an amorphous structure in contrast to crystalline ammonium sulfate. In the current study, RH was held at 55% and HNO_3 -DMA nanoparticles experienced growth. If aminium nitrate salts follow the trend of aminium sulfate with respect to their ammonium salt counterparts, it is likely that DMA- HNO_3 particles are amorphous and can uptake water at any RH. However, since SMPS scans were taken continuously with dry air, the size distribution is more reflective of the particle dry diameter, in which any water that contributed to growth has been evaporated. The observed growth must be then attributed to enhanced reactive uptake of HNO_3 and DMA into the particle in the presence of water.

Particle formation was stable at constant gas precursor concentrations and, therefore, measured size distributions did not change over time (Figure B.4). This allowed for long collection times of the smallest particle sizes for size-resolved studies of nanoparticle composition by TDCIMS.

3.4.2 Desorption thermograms of HNO₃-DMA particles under dry and humid conditions

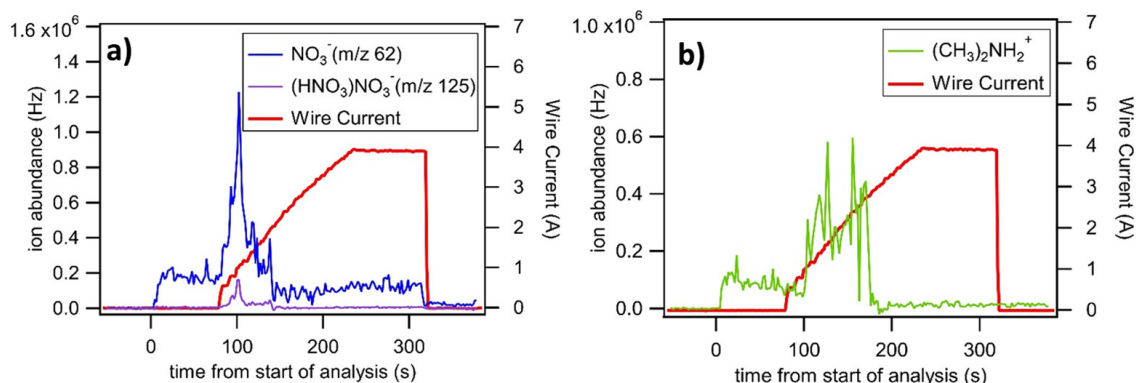


Figure 3.3: Representative desorption profiles of (a) NO₃⁻ ion (m/z 62), HNO₃(NO₃) ion (m/z 125), and (b) (CH₃)₂NH₂⁺ ion (m/z 46). Wire current is a proxy for the temperature of the wire.

Figure 3.3 shows representative TDCIMS desorption thermograms of relevant ions detected in this study. Profiles such as these provide qualitative information such as relative volatility and fragmentation pathways; particle adhesion to the metal surface of the collection filament has been shown to generally increase evaporation temperatures of constituents and this process likely also possesses some chemical specificity (Smith et al., 2008a; Chattopadhyay and Ziemann, 2007). Wire desorption temperatures were estimated by applying a power law correlation between the temperature and applied current and are uncertain to ± 50 °C. Dimethylaminium ((CH₃)₂NH₂⁺, m/z 46) and nitrate monomer (NO₃⁻, m/z 62) and dimer (HN₂O₆⁻, m/z 125) ions are detected as soon as the wire enters the heated ion source (40 °C, t=0 s). At t=60 s, the wire temperature ramp begins, and desorption is immediately observed for all relevant ions. Nitrate trimer (m/z 188) and water clusters of nitrate and dimethylaminium were not detected or contributed less than 0.1% to their respective total acid and base signal and were not incorporated into acid:base ratio calculations.

Desorption profiles of nitrate and ammonium ions in both the dry and humid systems were almost identical, with the only difference being that water cluster peaks of relevant ions appeared during the analysis of humid system particles but contributed to less than 0.5% of the total acid and base signal. The lack of water present in particles formed under humid conditions is most likely caused by the previously mentioned drying effects of the upstream size-selecting nano-DMA as well as the N_2 sheath gas that flows over the collection filament during sampling.

Atomized particles of dimethylamine and nitric acid have been studied for their thermal stability and have been shown to be more stable than ammonium nitrate (Salo et al., 2011), with approximately 50% volume fraction remaining at ~ 57 °C and complete loss of volume occurring at 77 °C. The thermograms of TDCIMS-detected ions align well with these observations, with desorption occurring as the wire enters the 40 °C ion source ($t=0$ s), and with increased desorption occurring immediately after the TDCIMS wire begins to heat. While the dependence of TDCIMS wire temperature to applied current is not easily characterized due to the complex conditions within the inlet, we estimate the endpoint wire temperature to be approximately 600 °C based on laboratory experiments of the evaporation of different salt samples. Using this information, we estimate the full desorption of particulate nitrate to occur by the time the wire reaches ~ 150 °C ($t = 145$ s, Figure 3.3a), and of particulate dimethylammonium to occur by ~ 250 °C ($t = 175$ s, Figure 3.3b). While these temperatures are higher than those reported by Salo et al, they are consistent with the adsorptive properties of the collection filament discussed above.

3.4.3 Size-resolved composition measurements

In the following discussion we use the term “neutral” to mean a fully neutralized acid:base ratio (i.e., 1:1 for the system studied here). Our use of this term applies to the relative concentration of particulate acid and base compounds only, and should not be extended to particle or bulk solution pH. Figure 3.4 shows the TDCIMS-measured, size-resolved acid:base ratio of particles formed from nitric acid and dimethylamine in both dry ($\sim 5\%$ RH) and humid ($\sim 55\%$ RH) conditions. The acid:base ratio was calculated by dividing the sum of the ion signals associated with nitrate by the

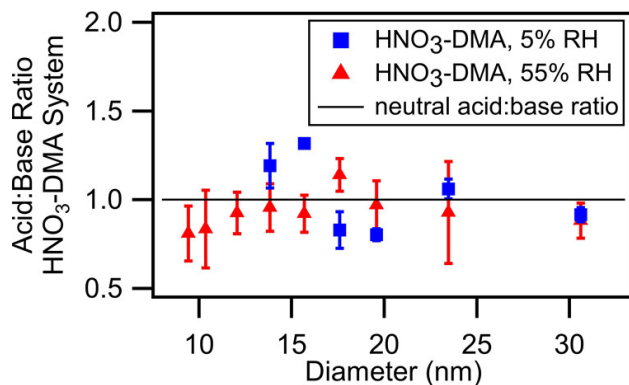


Figure 3.4: Size-resolved acid/base ratios of HNO₃-DMA particles. Red triangles represent particles formed in dry conditions, while blue squares represent particles formed in humid conditions. The black line is to guide the eye to a neutral 1:1 acid/base ratio.

sum of ion signals of associated with aminium. This ratio was normalized to the acid:base ratio measured from 30 nm atomized HNO₃-DMA salt particles to account for relative sensitivity of the TDCIMS to nitrate and aminium ions. For the humid system, the shifting of the size distribution to larger sizes (see Figure 3.2) meant that insufficient sample mass could be collected for particles smaller than 12 nm in diameter. In both the dry and humid case, the acid:base ratio does not deviate strongly from a neutral 1:1 ratio of HNO₃:DMA.

While these results confirm the notion that nitric acid and dimethylamine are too volatile to exist in the particle phase without neutralization, Chen et al. found in nanoparticles formed from sulfuric acid and ammonia/dimethylamine under both humid and dry conditions that particles smaller than 15 nm in diameter did not have a neutral acid:base ratio (Chen et al., 2018). In comparison, for the HNO₃-DMA particles produced in the absence of water, normalized acid:base ratios ranged from 0.81-1.14 over the size range of 9–30 nm. In the presence of water, acid:base ratios had a larger spread and ranged from 0.80–1.32. In both cases, the particle acid:base ratio did not have distinct trends toward more acidic or more basic particles at any size range. The fact that the measurements of acid:base ratio of HNO₃-DMA particles in this study exhibit trends so close to neutrality suggests fundamental chemical differences between salts of nitrate and those of sulfate. Some of these differences may include sulfuric acid’s greater number of hydrogen bonding sites, higher acidity, and lower volatility than those of nitric acid.

To more closely examine the particle growth process, clusters of nitric acid and dimethylamine were modeled to derive the most stable conformations. Results and their interpretation are presented in the next section. While the modeled clusters (max diameter ~ 1.5 nm) do not reflect the size regime of the nanoparticle measurements (9–30 nm), they do provide insights into initial growth pathways of these particles that lead to the formation of the nanoparticles that were measured by TDCIMS. Acid-base chemistry is the only possible way for particles to form and grow in this chemical system, and cluster calculations allows us to directly examine molecule-by-molecule addition to clusters.

3.4.4 Cluster modelling

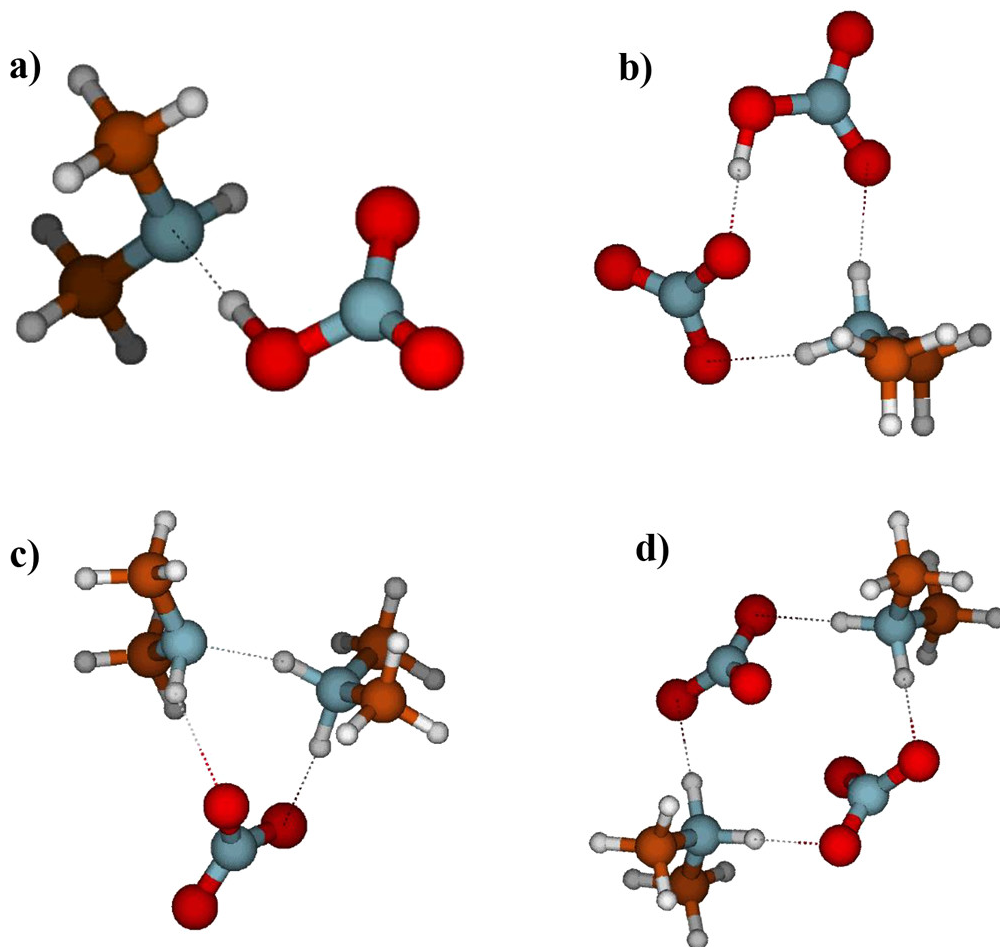


Figure 3.5: Clusters of (a) 1NA1D, (b) 2NA1D, (c) 1NA2D, and (d) 2NA2D. Color coding: carbon atoms are brown, oxygen atoms are red, nitrogen atoms are blue, and hydrogen atoms are gray. Dotted lines indicate hydrogen bonding between molecules.

In this section in which we present modeling results of cluster chemistry, we refer to nitric acid as NA, dimethylamine as D, and water as W. For example, a cluster of 2 nitric acid molecules, 1 dimethylamine molecule, and 1 water molecule will be referred to as 2NA1D1W. For many acid-base systems, the formation of a heterodimer, a cluster with one acid and one base molecule, has been demonstrated to be a crucial step in particle formation (Elm et al., 2017; Almeida et al., 2013a; Kürten et al., 2014; Petäjä et al., 2011). The Gibbs free energy of the reaction that produces the DMA-HNO₃ heterodimer from DMA + HNO₃ is -5.7 kcal/mol at 298.15 K, meaning that the intermolecular interaction between nitric acid and dimethylamine is very weak (compare, e.g., the Gibbs free energies of formation of heterodimers of sulfuric acid-dimethylamine (H₂SO₄-DMA) and sulfuric acid-ammonia (H₂SO₄-NH₃), which are -13.5 and -6.8 kcal/mol, respectively). As the calculated structure shown in Figure 3.5a shows, the reason for the weak interaction between nitric acid and dimethylamine is the absence of proton transfer in the heterodimer. Once the heterodimer is formed, additional cluster growth can occur via the addition of a second dimethylamine or nitric acid molecule, leading to the formation of 1NA2D or 2NA1D clusters. As Figures 3.5b and 3.5c show, in both clusters there is proton transfer from nitric acid to dimethylamine. The neutral molecule stabilizes the ion pair by forming hydrogen bonds with the anion and cation. The addition of nitric acid to the heterodimer is more thermodynamically favorable (-4.7 kcal/mol) than the addition of dimethylamine (-1.0 kcal/mol). This can be explained by referring to the cluster structures, which show that the 2NA1D and 1NA2D clusters both form 3 hydrogen bonding interactions. However, while the addition of a second dimethylamine molecule provides another hydrogen bond between a nitrogen atom and a hydrogen atom, the addition of a nitric acid molecule results in a stronger hydrogen bond between an oxygen atom and hydrogen atom.

The addition reaction of dimethylamine to the 2NA1D cluster, a neutralization step, is highly favorable with a Gibbs free energy for this reaction of -17.1 kcal/mol. This is because both nitric acid molecules have given their protons to the two dimethylamine molecules and a symmetric cluster is formed (Figure 3.5d). In each modeled cluster formation step, the addition of nitric acid to the neutral cluster ($x\text{NA}x\text{D}$) is thermodynamically more favorable than the addition of dimethylamine. A similar trend is also observed for other acid-base pairs, for instance, sulfuric acid cluster formation

with dimethylamine or ammonia (Bzdek et al., 2017). The neutralization steps are highly favorable since the number of proton transfer reactions are maximized, and thus the formed neutral clusters are most stable. It should be noted that even if the neutralization steps are thermodynamically highly favorable, there is likely to exist a kinetic barrier due to hydrogen-bond breaking and cluster rearrangement as shown in the study by DePalma et al. (2012).

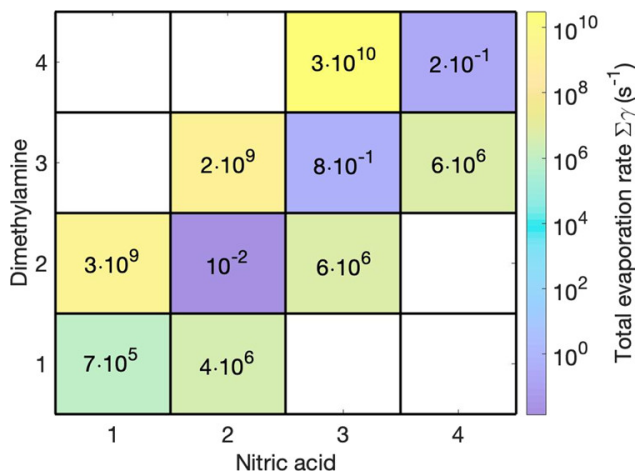


Figure 3.6: Overall evaporation rates for clusters of 1-4 nitric acid and 1-4 dimethylamine molecules at 298.15 K. Cells are colored from purple (lowest evaporation rates) to yellow (highest evaporation rates).

We have calculated the evaporation rates for each cluster from the Gibbs free formation energies (see Appendix B for details) for both clusters formed with and without water. Figure 3.6 shows the total evaporation rates of the cluster sizes studied, starting from 1NA1D and ending at 4NA4D, without the presence of water. As mentioned previously, the heterodimer 1NA1D is very weakly bound, which results in an evaporation rate as large as $7 * 10^5 \text{ s}^{-1}$. This volatility of the heterodimer cluster highlights the necessity for the high concentrations of gas-phase nitric acid and dimethylamine for nucleation to occur. The smallest stable cluster against evaporation is 2NA2D for which the evaporation rate is ~ 7 orders of magnitude lower than that of heterodimer. This dramatic decrease can be attributed for proton transfer reactions and cluster symmetry as discussed above. All large neutral clusters are relatively stable against evaporation, meaning that their total evaporation rate, defined as one or more molecules evaporating from the cluster, is smaller than 1 evaporation event per second. The clusters with non-equal numbers of acid and base molecules are unstable, since the additional acid or base molecules are likely to evaporate very fast because proton transfer has

not occurred. The clusters with compositions of $(x+1)\text{NA}x\text{D}$ have a ~ 3 order of magnitude lower evaporation rate than the clusters with a $x\text{NA}(x+1)\text{D}$ composition, which support the hypothesis that clusters grow by addition of nitric acid first, and then by neutralization by dimethylamine. Due to the significant difference in evaporation rates between neutral and acidic or basic clusters, we can assume that neutral clusters are the most stable ones independently of the particle size. This means that even though our computational and experimental methods leave a gap between 1–8 nm particle diameters, it is a reasonable assumption that particles are neutral also in that size regime.

In addition, we have studied HNO_3 -DMA clusters containing 1–4 water molecules. In general, water binds very weakly to these clusters and does not improve cluster stability significantly (Figure B.4). The interaction between nitric acid and water is very weak (-0.3 kcal/mol) and between dimethylamine and water it is even less favorable (0.7 kcal/mol). The Gibbs free formation energy of the 1NA1D1W cluster is -5.9 kcal/mol, meaning that the Gibbs free energy is lowered by 0.2 kcal/mol compared to the 1NA1D cluster. Although the presence of only one water molecule is able to promote the proton transfer from nitric acid to dimethylamine, the cluster is still very weakly bound and thus likely to evaporate. The Gibbs free energy of the addition of second water molecule to the 1NA1D1W cluster is -1.0 kcal/mol and the additions of the third and fourth water molecules are -0.3 and -0.2 kcal/mol, respectively. Since the water molecule addition reactions are thermodynamically only slightly favorable, the evaporation rates of the 1NA1D(1-4)W clusters are on the order of 10^{10} s^{-1} ; i.e., they have five orders of magnitude higher evaporation rates compared to the dry 1NA1D cluster due to the evaporation of water. Also, in the case of other clusters, water molecules are not capable of interacting with the cluster strongly enough, and indeed, all of the evaporation rates are very high, 10^8 - 10^{12} s^{-1} (Figure B.4). This implies that the role of hydration in the initial steps of HNO_3 -DMA particle formation is negligible, and the main clustering pathway goes via dry nitric acid-dimethylamine cluster formation (as explained above) leading to the acid:base ratio of 1:1 regardless of the level of relative humidity. This result is in excellent agreement with the experimental findings of this study. In addition, it has been previously shown for the H_2SO_4 -DMA system that water has only a minor effect in particle formation, reportedly due to a small number of available hydrogen bonds (Yang et al., 2018). Since nitric acid has a lower number of possibilities to

form hydrogen bonds than sulfuric acid, it is not surprising that water cannot enhance the formation of HNO_3 -DMA particles. In the Appendix B, we have demonstrated that the increased RH does not increase the particle formation rate at any laboratory or atmospherically relevant conditions. This is also apparent in the integrated number concentration for both the dry and humid systems, where no significant enhancement of particle number concentration was observed with increased RH. The instability of water molecules in DMA- HNO_3 particles suggests that our observations of enhanced particle growth in the presence of water was not necessarily because of water uptake, but rather water molecules facilitating the proton transfer reaction between nitric acid and dimethylamine to enhance reactive uptake. However, it is possible that at sizes larger than a 4NA4D cluster, water may be able to form enough hydrogen bonds to enhance particle growth.

3.4.5 Comparison to sulfuric acid-dimethylamine system

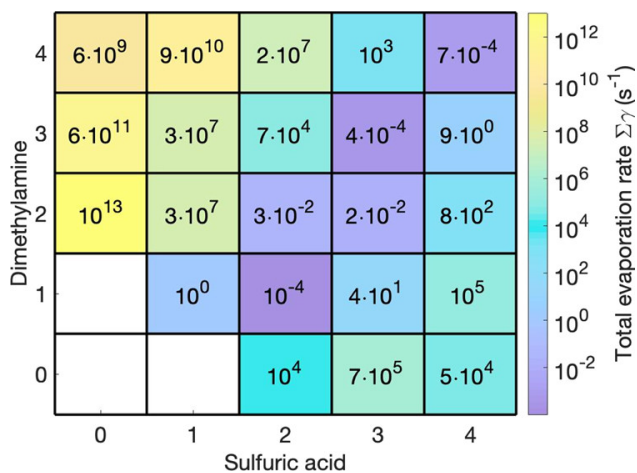


Figure 3.7: Overall evaporation rates for clusters of 1-4 sulfuric acid and 1-4 dimethylamine molecules at 298.15 K. Cells are colored from purple (lowest evaporation rates) to yellow (highest evaporation rates).

Given that these cluster calculations have provided a reasonable theoretical justification for the observed 1:1 acid:base ratios in DMA- HNO_3 nanoparticles, we also calculated the evaporation rates for clusters formed from sulfuric acid and dimethylamine under dry conditions. For this comparison, we refer to sulfuric acid as SA for cluster identification. The minimum energy structures and Gibbs free energies for clusters containing 0-4 H_2SO_4 molecules and 0-4 DMA molecules are taken from

our previous study (Myllys et al., 2019b). Figure 3.7 shows the calculated evaporation rates for H_2SO_4 -DMA clusters. Unlike for HNO_3 -DMA clusters, in which only stable clusters occur with an acid:base ratio of 1:1, H_2SO_4 -DMA clusters are stable in both the diagonal axis as well as below the diagonal, i.e., acidic clusters are also stable against evaporation.

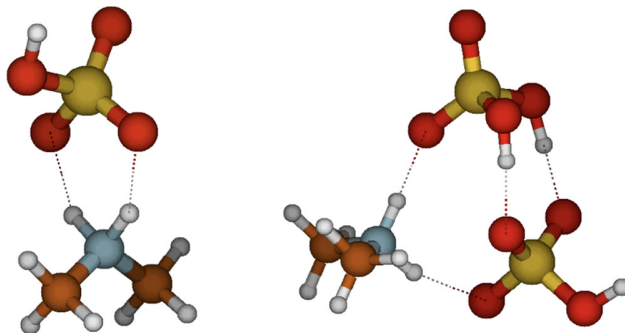


Figure 3.8: Molecular structures of 1SA1D (left) and 2SA1D (right). Color coding: sulfur atoms are yellow, oxygen atoms are red, nitrogen atoms are blue, and hydrogen atoms are gray. Dotted lines indicate hydrogen bonding interactions.

The calculated evaporation rate for the 1SA1D heterodimer is over five orders of magnitude lower than that of the 1NA1D heterodimer. The reason for this can be found from the cluster structures shown in Figure 3.8: in the 1SA1D cluster, sulfuric acid has donated a proton to dimethylamine and there are two intermolecular interactions between the ion pair, while as previously discussed, there is no proton transfer in the 1NA1D cluster and molecules are interacting via one hydrogen bond. As measurements for H_2SO_4 -DMA particles have shown, the small sulfuric acid-dimethylamine particles can contain either the same amount of acid and base molecules or more acid than base molecules (Lawler et al., 2016; Chen et al., 2018; Kürten et al., 2014). That is likely to be dependent on the conditions in which measurements are performed as well as the technique used to measure composition. These findings help shed light on the experimental results of Chen et al. (2018) and Lawler et al. (2016), especially in regards to the observation that the smallest H_2SO_4 -DMA nanoparticles tend to be more acidic despite the presence of excess gas-phase base. In the context of this study, the different behaviors of HNO_3 -DMA and H_2SO_4 -DMA particles can be explained by the strength of intermolecular interactions in the clusters and thus cluster stability. Intermolecular interactions between neutral nitric acid and nitrate or dimethylaminium ions are weak and thus more acidic HNO_3 -DMA clusters are evaporating with a rate higher than 10^6 s^{-1} . However, in the

2SA1D cluster structure, sulfuric acid binds very strongly (Gibbs free energy is -33.8 kcal/mol) to its deprotonated bisulfate counterpart. Thus, additional sulfuric acid molecules in the H_2SO_4 -DMA cluster, in which proton transfer has occurred, are not likely to evaporate. This allows clusters of H_2SO_4 -DMA to grow with a larger than 1:1 acid:base ratio.

3.5 Conclusions

In this study we performed size-resolved measurements of particles formed from dimethylamine and nitric acid under dry and humid conditions. Number-size distributions of these particles indicate that particles are hygroscopic and grow larger with higher relative humidity, but the presence of water vapor does not appear to affect total number concentration. Within experimental uncertainty, the acid:base ratio for nanoparticles formed under both dry and humid conditions remain at unity throughout growth from 9 nm to 30 nm in diameter. Modeled cluster evaporation rates show that clusters are only stable when a 1:1 HNO_3 :DMA ratio occurs, with and without added water vapor. This behavior is in agreement with a theoretical picture of proton exchange between a Brønsted Lowry acid (HNO_3) and base (NH_3), forming a salt with a 1:1 acid:base ratio. Cluster calculations and experimental results confirm what chemical theory might suggest: volatile precursors such as nitric acid and dimethylamine can only contribute to nanoparticle growth through the formation of non-volatile salts. In contrast, calculations performed on clusters formed from precursors containing one non-volatile component, sulfuric acid, show that nanoparticles formed from this system will likely deviate from neutrality due to the increased likelihood of stable structures involving both the deprotonated as well as neutral sulfuric acid molecule. While the current study provides insights into reactive uptake of acids and bases into nanoparticles, it is clear each chemical system exhibits unique properties that require in depth experimental and theoretical studies. Future research should focus on elucidating trends between acid and base structures (e.g., number of hydrogen bond donors or acceptors, symmetry and shape) and nanoparticle composition below 15 nm in diameter.

Chapter 4

A Predictive Model for Salt Nanoparticle Formation Using Heterodimer Stability Calculations

4.1 Abstract

Acid–base clusters and stable salt formation are critical drivers of new particle formation events in the atmosphere. In this study, we explore the relationship between $J_{1.5}$, the theoretically predicted formation rate of clusters larger than 4 acid and 4 base molecules, and acid–base heterodimer stability, a property that is relatively easy to calculate using computational methods. Heterodimer stability as a function of gas-phase acidity, aqueous-phase acidity, heterodimer proton transference, vapor pressure, dipole moment, and polarizability were explored for the salts comprised of sulfuric acid, methanesulfonic acid, and nitric acid with nine bases. The best predictor of heterodimer stability was found to be gas-phase acidity. The relationship between heterodimer stability and $J_{1.5}$ was analyzed for sulfuric acid salts over a range of monomer concentrations from 10^5 to 10^9 molec cm^{-3} and temperatures from 248 to 348 K. Heterodimer concentration was calculated from

heterodimer stability and yielded an expression for predicting $J_{1.5}$ for any salt, given approximately equal acid and base monomer concentrations and knowledge of monomer concentration and temperature. This parameterization was tested for the sulfuric acid–ammonia system by comparing the predicted values to experimental data and was found to be accurate within 2 orders of magnitude. We show that one can create a simple parameterization that incorporates the dependence on temperature and monomer concentration on $J_{1.5}$ by defining a new term that we call the normalized heterodimer concentration, Φ . A plot of $J_{1.5}$ vs. Φ collapses to a single monotonic curve for all weak salts of sulfuric acid, and can be used to accurately estimate $J_{1.5}$ in atmospheric models.

4.2 Introduction

Atmospheric aerosol particles represent the largest uncertainty in our understanding of global climate through their participation in cloud formation and the absorption and scattering of radiation (Kerminen et al., 2005; Kuang et al., 2009; Lohmann and Feichter, 2004; Merikanto et al., 2009; Spracklen et al., 2008). In particular, particle formation by nucleation is still not well understood and is difficult to represent in models (Kerminen et al., 2018). One of the dominant nucleation pathways is through salt formation, where the formation of a cluster is stabilized by the interactions between acid and base molecules, which enhances particle formation (Ball et al., 1999; Kirkby et al., 2011; Kürten et al., 2016; Nadykto and Yu, 2007; Nadykto et al., 2015; Wang et al., 2018). This nucleation pathway is particularly dominant in urban environments, where anthropogenic sources for acidic and basic gases are abundant (Ge et al., 2011; Kirkby et al., 2011; Qiu and Zhang, 2013; Weber et al., 1996; Wang et al., 2020). Although sulfuric acid (H_2SO_4 , sa) is most commonly associated with atmospheric nucleation (Ball et al., 1999; Bzdek et al., 2012; Kirkby et al., 2011; Angelino et al., 2001; Weber et al., 1995), nitric acid (HNO_3 , na) and methanesulfonic acid ($\text{CH}_3\text{SO}_3\text{H}$, msa) have been also observed to be participants and may also play important roles in the initial stages of cluster growth (Afpel et al., 1979; Barsanti et al., 2009; Mäkelä et al., 2001; Smith et al., 2004, 2008a; Weber et al., 1995), the latter of which we shall refer to henceforth as new particle formation (NPF).

Ammonia is the most abundant base in the atmosphere and its reaction with sulfuric acid has been well studied (Bzdek et al., 2010; Glasoe et al., 2015; Weber et al., 1996). Alkylamines have also garnered attention due to their high basicity and demonstrated ability to enhance NPF more than ammonia, despite their lower atmospheric abundance (Kurtén et al., 2008; Smith et al., 2010b; Temelso et al., 2018; Waller et al., 2019; Kreinbihl et al., 2020).

Recently, computational efforts have focused on accurately representing the formation and growth of acid–base clusters (Smith et al., 2021). Myllys et al. (2016b) investigated the accuracy of the domain local pair natural orbital coupled cluster (DLPNO–CCSD(T)) method, and found that it allows for the modeling of up to 10 molecules in a cluster, which had been previously not feasible with other highly accurate methods. The DLPNO–CCSD(T)/aug-cc-pVTZ// ω B97X-D/6-31++G** level of theory has become increasingly popular for modeling atmospheric processes such as cluster formation of sulfuric acid with ammonia, methylamine, dimethylamine, trimethylamine, guanidine, monoethanolamine, trimethylamine N-oxide, and a variety of diamines (Myllys et al., 2016b; Ma et al., 2019; Xie et al., 2017; Myllys et al., 2020, 2018b; Elm et al., 2016, 2017).

This large variety in systems studied has yielded insights into the factors that determine cluster formation and growth. Generally, the enhancing efficiency of the base on heterodimer stability and NPF is known to correlate with base strength, which has been attributed to a more favorable proton transfer and the formation of essentially nonvolatile ionic salts and has been shown to be generally true for the most abundant bases in the atmosphere: ammonia, methylamine, dimethylamine, and trimethylamine (Almeida et al., 2013a; Elm, 2017a; Myllys et al., 2019b; Barsanti et al., 2009; Shen et al., 2020; Han et al., 2020). For many studies that observe both cluster and nanoparticle formation and growth, pK_a has been often used as the metric for basicity. However, since pK_a is, by definition, an aqueous measure of acidity, applying it to cluster and nanoparticle-sized systems does not take into account the drastically different environment. Indeed, in the study by Xie et al. (2017), monoethanolamine ($pK_a = 9.5$) enhanced NPF more than methylamine ($pK_a = 10.6$), despite methylamine being the stronger base according to their pK_a values (Haynes, 2014). In that study, the lack of a base strength trend was attributed to the additional hydrogen bonding sites provided by the -OH group on monoethanolamine. In addition, we have recently studied

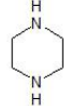
the modelled formation rates of sulfuric acid and trimethylamine-N-oxide (tmao), guanidine, or dimethylamine, where tmao, despite its lower basicity ($pK_a = 4.7$) to both guanidine ($pK_a = 13.6$) and dimethylamine ($pK_a = 10.7$), had similar formation rates to guanidine, which were much higher than those of dimethylamine (Myllys et al., 2020; Haynes, 2014). In these studies, pK_a was insufficient to predict NPF enhancement.

In this study, we aim to use these computational methods to identify what molecular properties predict heterodimer stability, or more specifically the Gibbs free energy of formation of the heterodimer ($\Delta G_{\text{heterodimer}}$), and in turn, formulate a model to predict NPF rate. We specifically investigate the use of pK_a in comparison to gas-phase acidity measures to predict proton transfer in the heterodimer as well as heterodimer stability. In addition, we examine if base vapor pressure has any correlation to heterodimer stability, as sulfuric acid is often cited to participate in NPF because of its low volatility and condensation onto clusters (Weber et al., 1996; Ball et al., 1999; Sipilä et al., 2010). Finally, we also calculate the dipole moment and polarizability of the studied base molecules to see if, in the absence of ions, they have any predictive capability of heterodimer stability. These observations extend to salts of sa, msa, and na with nine bases: ammonia (amm), methylamine (ma), dimethylamine (dma), trimethylamine (tma), trimethylamine N-oxide (tmao), guanidine (gua), monoethanolamine (mea), putrescine (put) and piperazine (pz) (Table 4.1).

In addition to these molecular properties, we further explore the relationship between heterodimer stability and NPF rate for sa salts. The goal of this work is to develop computationally efficient approaches for calculating NPF rate that can be applied to models that estimate the impacts of NPF on climate and air quality. We represent NPF rate as $J_{1.5}$, the rate at which a cluster larger than 4 acid and 4 base molecules is formed. A cluster of this size can range in diameter from 1 to 1.5 nm, depending on the constituent acid and base. We analyze the relationship between heterodimer stability and the theoretically predicted $J_{1.5}$ for sulfuric acid salts over a range of monomer concentrations from 10^5 to 10^9 molec cm^{-3} and temperatures from 248 to 348 K. The concentration of heterodimers was calculated from heterodimer stability, temperature, and monomer concentrations for the case where acid and base monomer concentrations are approximately equal. This results in a parametrization for $J_{1.5}$ as a function of heterodimer concentration that can be

applied to any acid–base system. These results were compared to $J_{1.7}$ rates measured at the CLOUD (Cosmics Leaving OUtdoor Droplets) chamber for sa–amm salts. We note that the relationship between $J_{1.5}$ and heterodimer concentration is not unique, but depends on both temperature and monomer concentration. However if the dependent variable is redefined as a term that we call the “normalized heterodimer concentration,” or Φ , then a simple monotonic relationship develops that can be used to predict $J_{1.5}$ for all weak salts of sulfuric acid, a system that is of great interest in the atmosphere. We believe that this approach is generalizable to any acid–base system, allowing accurate predictions of NPF rates over a wide range of monomer concentration, temperature, and ambient pressure.

Table 4.1: Acid and base compounds in this study. Abbreviations are as follows: ammonia (amm), methylamine (ma), dimethylamine (dma), trimethylamine (tma), trimethylamine N-oxide (tmao), guanidine (gua), monoethanolamine (mea), piperazine (pz), putrescine (put), sulfuric acid (sa), methanesulfonic acid (msa), and nitric acid (na).

amm	ma	dma	tma	tmao
NH_3	$\text{H}_2\text{N}-\text{CH}_3$	$\text{H}_3\text{C}-\text{NH}-\text{CH}_3$	$\text{H}_3\text{C}-\text{N}(\text{CH}_3)_3$	$\text{H}_3\text{C}-\text{N}^+(\text{CH}_3)_3-\text{O}^-$
gua	mea	pz	put	
$\text{H}_2\text{N}-\text{C}(\text{NH})=\text{NH}_2$	$\text{HO}-\text{CH}_2-\text{CH}_2-\text{NH}_2$		$\text{H}_2\text{N}-\text{CH}_2-\text{CH}_2-\text{CH}_2-\text{CH}_2-\text{NH}_2$	
sa	msa		na	
$\text{HO}-\text{S}(=\text{O})_2-\text{OH}$	$\text{HO}-\text{S}(=\text{O})_2-\text{CH}_3$		$\text{HO}-\text{N}^+(\text{O})-\text{O}^-$	

4.3 Computational methods

Two-component acid–base particle formation was studied by making systematic changes in temperature and concentration to understand the effects of simulation conditions and acid/base molecular properties on $J_{1.5}$. Correlations of $J_{1.5}$ with different molecular properties provided insight into

the critical factors of cluster formation. Properties listed in Table 4.2 were examined as possible variables that may have a role in stabilizing clusters and enhancing particle formation.

Table 4.2: Experimental and calculated properties examined in this study.

Property	Source
Gas phase acidity (GA)	calculated this work
Difference between GA of an acid HA and a conjugate acid of a base BH ⁺ (Δ GA)	calculated this work
Aqueous phase acidity (pK_a)	from Haynes (2014)
Difference between pK_a of HA and BH ⁺ (ΔpK_a)	from Haynes (2014)
Vapor pressure	from literature ^a
Electrochemical properties: dipole moment and polarizability	calculated this work
Solvation free energy difference between a base B and its protonated form BH ⁺ ($\Delta\Delta$ SOL)	calculated this work
Heterodimer stability ($\Delta G_{\text{heterodimer}}$, free energy of a complex having one acid and one base)	calculated this work
Remaining H-bond donors on base molecule in heterodimer	inferred
Proton transfer in heterodimer	inferred

^aStull (1947); Aston et al. (1937, 1939); Swift and Hochanadel (1945); Matthews et al. (1950); EPISUITE v 4.11

4.3.1 Cluster thermodynamics

In order to simulate cluster formation and growth, one must calculate accurate structures and thermochemical properties of neutral sa–base clusters up to the cluster size of four sa and four base molecules (4sa4base). Thermochemistry of clusters containing amm, dma, gua and tmao were taken from our previous studies (Myllys et al., 2018a, 2019a, 2020). Thermochemistry of clusters with mea, put and pz were taken from a database (Elm, 2019), collected from original publications of Xie et al. (2017), Elm et al. (2017) and Ma et al. (2019). Available structures with ma and tma were taken from Olenius et al. (2017) and, to be consistent with the level of theory used, structures were optimized and frequencies calculated at the ω B97X-D/6-31++G** level and electronic energies corrected at the DLPNO–CCSD(T)/aug-cc-pVTZ level with TightPNO, TightSCF, and GRID4 keywords. In addition, for the missing structures, we performed a configurational sampling as explained in Kubečka et al. (2019). For the lowest free energy clusters, Gibbs free binding energies were calculated at the DLPNO–CCSD(T)/aug-cc-pVTZ// ω B97X-D/6-31++G** level of theory (Riplinger and Neese, 2013; Riplinger et al., 2013; Myllys et al., 2016b,a).

In addition of a full data set for sa–base clusters, we studied heterodimers of na and msa with above-mentioned nine bases. The same quantum chemical methods were used as in sa–base calculations. In order to detect whether proton transfer was occurring in the heterodimer, the Molden program (Schaftenaar and Noordik, 2000) was used to visualize the global minimum structure. Gas-phase basicity and proton affinity values were computed using the same level of theory. Gaussian 16 RevA.03 (Frisch et al., 2016) was used to optimize geometries and calculate vibrational frequencies and Orca version 4.2.1 (Neese, 2012) was used for single point energy corrections.

4.3.2 Particle formation simulations

Theoretical methods allow us to perform particle formation simulations at any conditions. This means that very low or high temperatures and vapor concentrations can be used to estimate $J_{1.5}$. While some values in this range might not be directly “atmospherically relevant,” these calculations can lead to a deeper understanding of the non-linear behavior of nucleation as a function of vapor concentrations and/or temperature. It is also possible to study cluster formation of different compounds under identical conditions because there are no instrumental limitations or measurement biases.

The calculated thermodynamic data sets for sa–base clusters were used as input in Atmospheric Cluster Dynamics Code (ACDC), which detailed theory is explained in McGrath et al. (2012). Briefly, the ACDC model simulated particle formation by solving the cluster distribution considering collision, evaporation and removal processes. The model calculated the rate constants for each process among the population of clusters and vapor molecules and solved the discrete general dynamic equations for each cluster type. We have performed $J_{1.5}$ simulations at temperatures of 248–348 K using sa and base vapor concentrations of $[\text{acid}] = [\text{base}] = 10^5 - 10^9 \text{ cm}^{-3}$. Simulated $J_{1.5}$ values are given in Appendix C. Simulations were performed for neutral clustering pathways at dry conditions due to computational (quantum chemical) restrictions.

4.4 Results and discussion

4.4.1 Heterodimer stability results

In the cluster formation process, the changes in enthalpy (ΔH) and entropy (ΔS) are always negative because hydrogen bond formation is an exothermic process in which the degrees of freedom are decreasing when isolated molecules become one entity. Gibbs free energy is calculated from ΔH and ΔS as a function of temperature by

$$\Delta G = \Delta H - T\Delta S \tag{4.1}$$

where ΔG decreases as temperature decreases. Lower $\Delta G_{\text{heterodimer}}$ values correspond to more stable heterodimers. However, while a negative $\Delta G_{\text{heterodimer}}$ value indicates a spontaneous reaction in solution at standard conditions, heterodimer formation in the gas phase under atmospheric conditions also depends on the acid and base vapor concentrations. Table C.3 presents enthalpies, entropies and Gibbs free energies of sa–base heterodimer formation at 298 K and corresponding tables for msa and na are given in Appendix C. From these data, heterodimer stability can be calculated at other temperatures readily for all 27 salts studied here. Our calculated $\Delta G_{\text{heterodimer}}$ value for sa–amm indicates a less stable heterodimer than the sa–amines heterodimers, which is consistent with numerous other studies (Kurtén et al., 2008; Nadykto et al., 2011; Leverentz et al., 2013; Kupiainen et al., 2012). Ma and mea are the weakest heterodimer stabilizers among the amines; dma, tma and pz are stronger and form approximately equally stable heterodimers. Of these nine bases, the most stable heterodimers are formed with tmao, gua, and put.

The molecular structures of sa–base heterodimers are presented in Fig. 4.1 and for msa and na heterodimers in Appendix C. Amm is the only base which is unable to accept a proton from sa in the heterodimer structure; the heterodimer is held together via one hydrogen bond between amm and sa. All other base compounds accept a proton from sa and form an ion pair with the deprotonated sa, bisulfate. Protonated tma and tmao form only one hydrogen bond with bisulfate,

Table 4.3: Calculated enthalpy ($\Delta H_{\text{heterodimer}}$ in kcal/mol), entropy ($\Delta S_{\text{heterodimer}}$ in cal/(mol·K)) and Gibbs free energy ($\Delta G_{\text{heterodimer}}$ in kcal/mol) for sa-base heterodimer formation at 298 K.

BASE	$\Delta H_{\text{heterodimer}}$	$\Delta S_{\text{heterodimer}}$	$\Delta G_{\text{heterodimer}}$
amm	-15.1	-29.2	-6.4
ma	-18.2	-33.6	-8.2
dma	-22.2	-30.3	-13.2
tma	-23.6	-35.2	-13.1
tmao	-32.2	-34.9	-21.8
gua	-29.4	-30.4	-20.3
mea	-21.8	-38.2	-10.4
put	-28.9	-44.8	-15.6
pz	-22.8	-33.3	-12.9

whereas the other bases form two hydrogen bonds. In the sa-put heterodimer, put also forms an intramolecular hydrogen bond via its protonated and non-protonated amino groups.

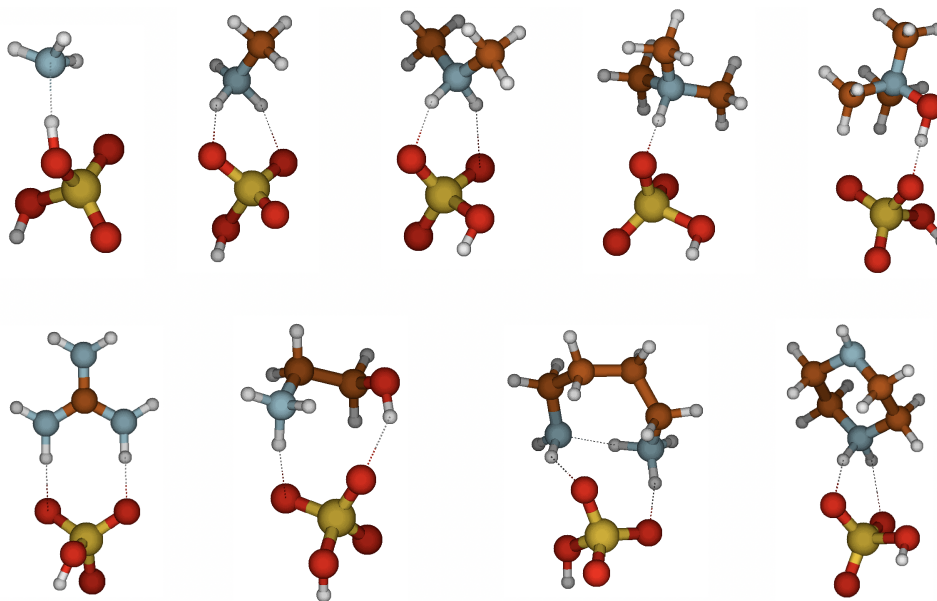


Figure 4.1: Heterodimers of sa with amm, ma, dma, tma, tmao, gua, mea, put and pz, respectively.

4.4.2 Molecular properties that affect heterodimer stability ($\Delta G_{\text{heterodimer}}$)

Evaluation of gas-phase versus aqueous-phase acidity

Figure 4.2 shows that gas phase and aqueous phase basicity values do not trend the same amongst the nine bases. For NR_3 compounds, where R is either H or CH_3 , the gas-phase monomer basicities directly follow the number of substitutions as $\text{amm} < \text{ma} < \text{dma} < \text{tma}$. This means that when removing a proton from isolated gas-phase BH^+ compound, the Gibbs free reaction energy has the largest value in the case of tma. That is because the methyl groups stabilize cation formation by distributing the charge. In the aqueous-phase ($\text{p}K_{\text{a}}$), however, the basicities have an different order: $\text{amm} < \text{tma} < \text{ma} < \text{dma}$. This means that dma has the largest proportion of protonated base cations in water solution. Dma has two methyl groups that facilitate protonation, and H-bond formation with water molecules provides additional stabilization. In the case of tma, the hydration is very limited due to the steric hindrance of three methyl groups, and thus, tma has lower aqueous-phase basicity than dma and ma. Because the basicity order of amines in the gas-phase directly follows the substitution order, the anomalous inversion of basicities in aqueous-phase can be attributed to the stabilization effect of surrounding solvent molecules (Seybold and Shields, 2015).

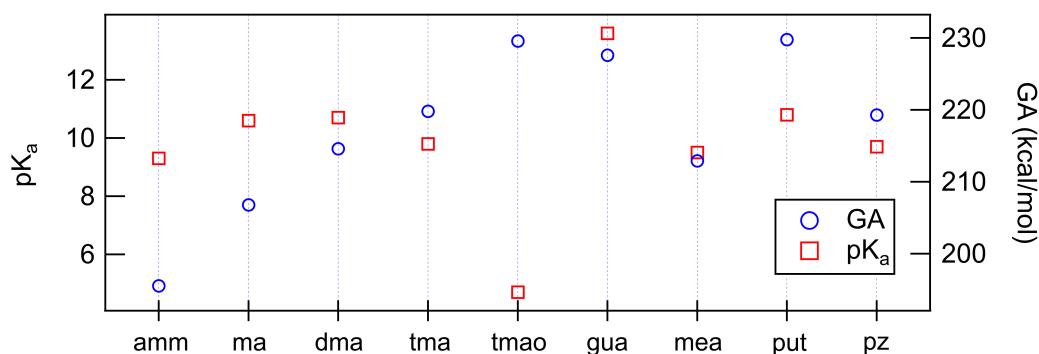


Figure 4.2: Calculated GA vs literature $\text{p}K_{\text{a}}$ values from Haynes (2014).

In the gas phase, the strongest bases are, in decreasing order, put, tmao and gua, whereas in the aqueous phase the order is gua, put and dma. Gua is a very strong base both in gas and aqueous

phase because its cationic form has six π -electrons that are delocalized over the Y-shaped plane. This D_{3h} -symmetric structure of guanidinium makes it extraordinarily stable. Tmao is very strong base in the gas phase because of its zwitterionic bond, where oxygen has a negative charge that strongly attracts H^+ . In the aqueous phase, polar solvent molecules are capable of stabilizing the zwitterionic bond in tmao, thus tmao is the weakest base in the water solution. The reason why put is the strongest base in the gas phase is related to the change of its configuration between neutral and cationic forms. The neutral form of put is linear, but the cation is cyclic as the protonated and deprotonated amino groups are hydrogen bonded to each other as shown in Fig. 4.3. The Gibbs free energy difference between cyclic global minimum configuration and lowest acyclic local minimum configuration is 14.6 kcal/mol, which is the additional stabilization caused by the H-bond in gas phase. The gas basicity of put calculated based on the acyclic form would be 215.2 kcal/mol, which is very close to that of dma — and interestingly the pK_a values of dma and put are very close to each other. This could indicate that protonated put is in aqueous phase mainly in its acyclic form and is stabilized by H-bonds with water molecules in the same manner as dma.

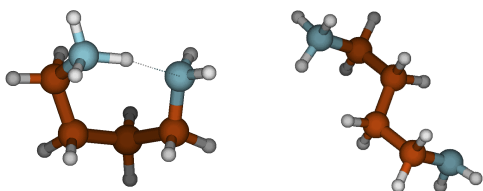


Figure 4.3: Cyclic and acyclic configurations of protonated put. The lowest energy acyclic structure is 14.6 kcal/mol higher in free energy than the cyclic, global minimum structure.

As put and pz are diamines, they can accept two protons and form baseH_2^+ cations. The PA and GA values for the second protonation reaction are significantly smaller than for the first protonation reaction: for put 130.6 and 125.2 kcal/mol and for pz 121.0 and 113.3 kcal/mol, respectively. While the PA and GA values can be measured for the first protonation reaction for each base, there was no experimental data found for the second protonation reaction. Experimental PA and GA values from Hunter and Lias (1998) are given in Appendix C and good agreement with our calculated values is shown. PA, GA and pK_a values are listed for sa, msa and na in Appendix C.

Because heterodimer stability has been shown to be a good proxy for $J_{1.5}$, we have plotted the correlation between $\Delta G_{\text{heterodimer}}$ and ΔGA and ΔpK_a to probe the hypothesis that acid and base strength predict the formation of the heterodimer (Figure 4.4). Here ΔGA is defined to be the difference between the GA of the acid and the GA of the protonated base. And similarly the ΔpK_a value is defined as the difference between the pK_a of the acid and the pK_a of the protonated base. All pK_a values were taken from literature as bulk aqueous phase dissociation constants, whereas GA values were calculated for this study. By definition, the larger the ΔGA , the less favorable the acid–base reaction is in the gas phase. Similarly, the more positive the ΔpK_a , the less favorable the acid–base reaction is in the bulk aqueous phase.

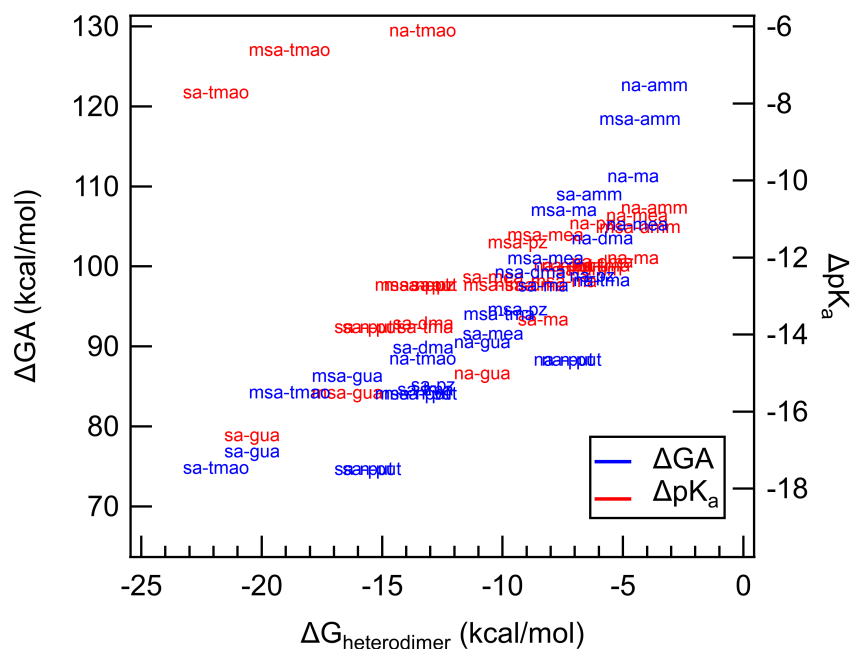


Figure 4.4: Calculated ΔGA and ΔpK_a plotted against $\Delta G_{\text{heterodimer}}$. Each data point represents an acid–base pair between either sa, na, or msa with either amm, ma, dma, tma, tmao, gua, mea, put, or pz. Blue text represent ΔGA values, while red text represent ΔpK_a values. Text markers are centered over the data point.

Over the observed ΔGA , as ΔGA increases, the less stable the heterodimer. The story is similar for ΔpK_a : as ΔpK_a increases, the heterodimer becomes less stable. However, for ΔpK_a , tmao salts seem to deviate drastically from the trend. Indeed, this is most likely because tmao is more able to be stabilized by water molecules in the bulk aqueous phase and its proton exchange in the gas phase is not well represented by pK_a . Otherwise, the trend of ΔpK_a matches up well with

that of ΔGA . These results demonstrate that acid and base strength have a clear relationship with $\Delta G_{\text{heterodimer}}$, and that ΔGA can be used in parameterizations of $\Delta G_{\text{heterodimer}}$. ΔGA is even less computationally intensive than $\Delta G_{\text{heterodimer}}$ because it only models the removal of a proton from the original molecule in comparison to modeling the interactions of two molecules. In addition, GA values can be calculated for an array of acids and bases to get ΔGA for a larger combination of acids and bases rather than modelling $\Delta G_{\text{heterodimer}}$ for each acid–base pair. For example, in this study, 3 acids and 9 bases were studied: to calculate ΔGA for all combinations, only 12 reactions need to be simulated; in contrast, $\Delta G_{\text{heterodimer}}$ would need to be calculated for each of the 27 salts. Because the GA values calculated here agree well with those experimentally determined in Hunter and Lias (1998), this modeling approach may be a simpler, more consistent method to predict GA values for yet-unstudied bases, including those that are atmospherically relevant.

Figure 4.5 illustrates how ΔGA is a better predictor of proton transfer in the gas phase than ΔpK_a . In general, acid–base pairs with ΔGA of 103 kcal/mol or below undergo proton transfer, and thus ΔGA provides a threshold for cluster formation. This is consistent with the stronger trends between heterodimer stability and GA than heterodimer stability and pK_a , the latter of which was affected by the solubilities of the acids and bases, which is not relevant to cluster formation and growth in the gas phase.

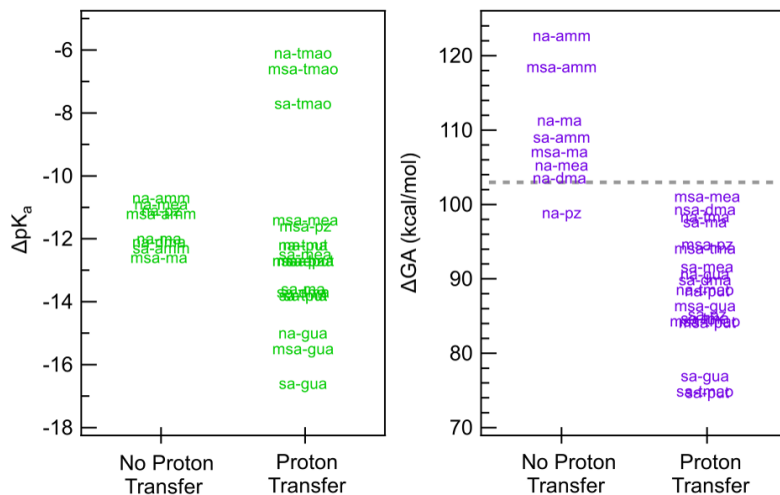


Figure 4.5: ΔGA and ΔpK_a values separated based on whether the heterodimer structure exhibits proton transfer. The grey dashed line on the ΔGA graph at 103 kcal/mol shows the cutoff point for proton transfer.

Interestingly, the na-pz salt is an anomaly in the cutoff for ΔGA in predicting proton transfer, with ΔGA value of 98.9 kcal/mol, yet there is no proton transfer in the global minimum structures of heterodimer. However, there exists a local minimum structure in which proton transfer occurs that is only 1.8 kcal/mol higher in free energy than the global minimum. Figure 4.6 shows that in the proton transferred form of the na-pz pair, the second H-bond formation, which is needed to stabilize the anion-cation pair, is unfavorable because of the induced ring strain. Generally, na is less likely to form two H-bonds with a base than sa or msa as the angle of O-N-O is 120° whereas the O-S-O angle in sa and msa are 109° , and therefore the ring strain would be high in na salts (with an exception for gua as shown in Appendix C). Overall, heterodimer proton transfer only occurs in clusters with a ΔGA smaller than 103 kcal/mol (na-put) with the exception of na-pz. In general, this strengthens the idea that ΔGA is a better estimate of gas-phase reactivity than $\Delta\text{p}K_a$ and emphasizes the importance of using thermodynamic constants that accurately represent the systems being studied.

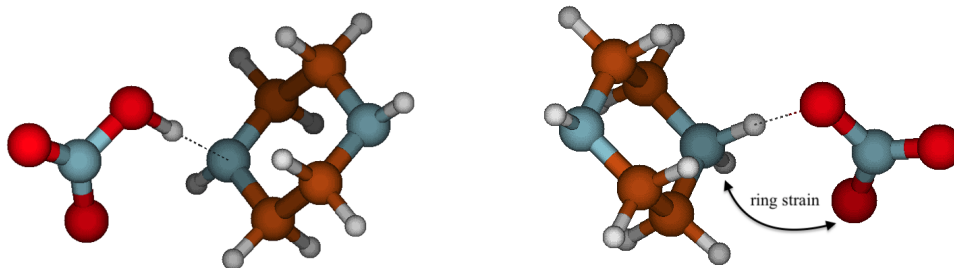


Figure 4.6: Deprotonated (left) and protonated (right) conformers of pz for the na-pz salt showing the ring strain necessary to form another intermolecular hydrogen bond.

ΔGA and $\Delta\text{p}K_a$ values can and should be used in lab settings to gauge the likelihood of nucleation. For example, numerous studies, including those in our own lab, show that oxalic acid does not form particles with any of the methylated amines (ma, dma, tma) in a two-component system at 298 K (Arquero et al., 2017b). The most negative $\Delta\text{p}K_a$ value for these oxalic acid salts is -9.45 , which is more positive than any of the systems studied here. Considering that na-amm does not form particles at room temperature even at high concentrations, its $\Delta\text{p}K_a$ value of -10.7 , or its ΔGA value of 122.65 kcal/mol, could be used as a benchmark for predicting particle formation at room temperature. This cutoff is dependent on both temperature and the concentrations of

precursor acid and base and should be viewed as a qualitative means for predicting NPF at room temperature. A more accurate means of estimating NPF rates that accounts for both temperature and precursor concentration is presented in Section 4.4.3.

Factors that do not affect heterodimer stability

Figure 4.7 shows the relationship between base vapor pressure and heterodimer stability ($\Delta G_{\text{heterodimer}}$), which is plotted to explore the hypothesis that the volatility of the base, which is typically much higher than that of the accompanying acid, is a limiting factor that drives NPF. The lack of correlation suggests that acid–base reactive uptake, leading to salt formation, is the dominant mechanism and that volatility of the constituent acid and base plays a relatively minor role in heterodimer stability. It is important to emphasize that this lack of correlation between vapor pressure and heterodimer stability is only observable because the bases have different structural properties. Otherwise, if only amm, ma, dma, and tma were studied, then trends for vapor pressure and heterodimer stability would follow the trend of the more volatile base making a less stable heterodimer, which is untrue. Since the most well-studied bases in the atmosphere are amm, ma, dma, and tma, due to their relative abundance and contribution to NPF, it may be tempting to make conclusions on base behavior in NPF based solely on those four bases. However, these correlations — or lack thereof — highlight the importance of a wider breadth of study for us to better understand how bases behave in the atmosphere. This disappearance of a trend as more bases are included applies to the dipole moment and polarizability of the base as well (see Appendix C). However, it is worth noting that while base vapor pressure does not affect heterodimer stability, it may have a larger role in determining particle composition as particles grow to a size that represents bulk systems (Lawler et al., 2016; Chen and Finlayson-Pitts, 2017; Myllys et al., 2020; Chee et al., 2019).

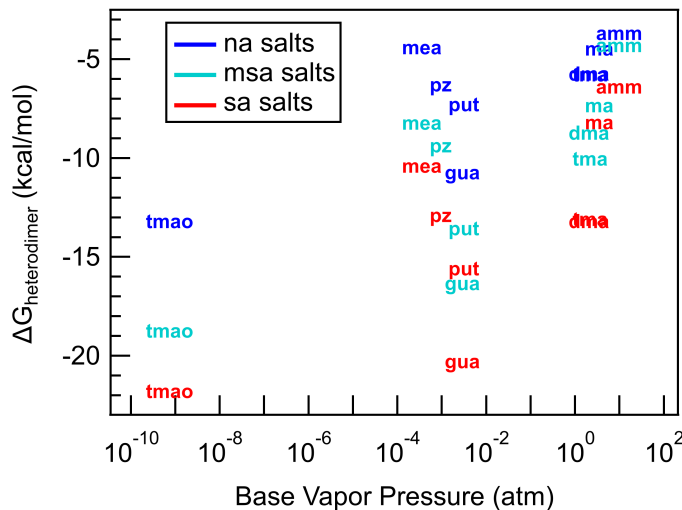


Figure 4.7: Base vapor pressure plotted against $\Delta G_{\text{heterodimer}}$ for sa, msa, and na salts.

4.4.3 Heterodimer stability versus $J_{1.5}$

The stabilities of a heterodimer and other small clusters are known to affect the ability of a cluster to grow to a large aerosol particle (Almeida et al., 2013b; Elm, 2017b; Olenius et al., 2013). We now correlate $\Delta G_{\text{heterodimer}}$ with calculated $J_{1.5}$ for all nine bases with sa at varying conditions to observe the change in new particle formation rate over the temperature range of 248–348 K (Figure 4.8a), and acid and base monomer concentrations from 10^5 – 10^9 molec cm^{-3} (Figure 4.8b). For reference, a J of $0.1 \text{ cm}^{-3}\text{s}^{-1}$ is also indicated, which can be viewed as a lower limit for observed atmospheric $J_{1.5}$ (Kerminen et al., 2018). We emphasize that these some of the concentrations and temperatures might not be very common in the atmosphere. However, through these systematic changes in temperature and concentrations, we are able to gain insight into the predictors of cluster formation and growth.

Previously, theoretically calculated $J_{1.5}$ for reactions of sa with dma or amm have been shown to be a good approximation for experimentally determined NPF rates observed at the CLOUD chamber (Myllys et al., 2019c). As Figure 4.8a shows, $J_{1.5}$ follow a lognormal relationship with $\Delta G_{\text{heterodimer}}$. This makes sense in that, for the most stable heterodimers like salts of tmao and gua, $J_{1.5}$ approaches the kinetic limit and simply cannot form any faster. However, as heterodimer

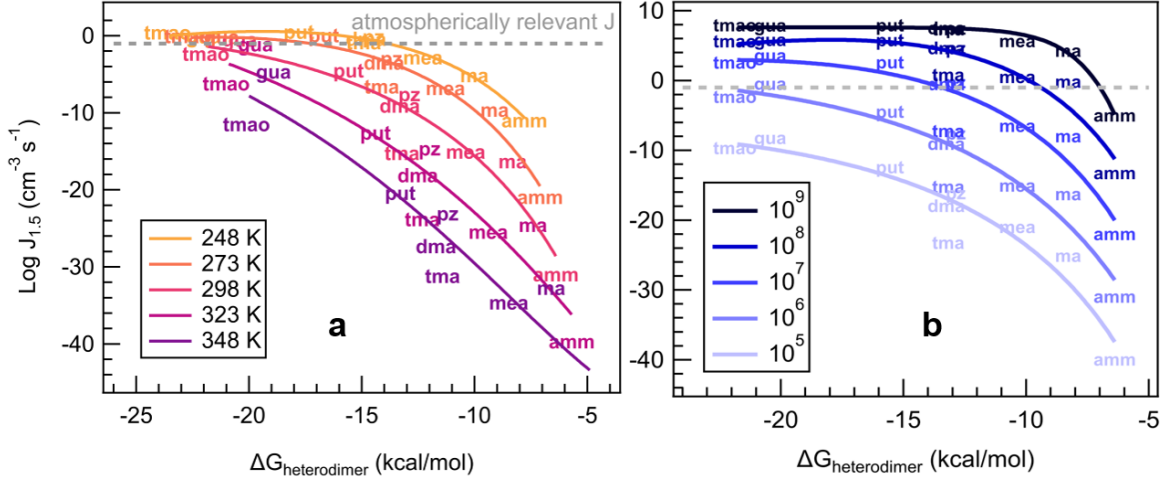


Figure 4.8: Heterodimer stability ($\Delta G_{\text{heterodimer}}$) plotted against NPF rate (J_{theory}) in varied conditions. a) Vapor concentrations are constant: $[\text{acid}] = [\text{base}] = 10^6 \text{ molec cm}^{-3}$ at varying temperature: $T = 248, 273, 298, 323,$ and 348 K . b) Temperature is constant: $T = 298 \text{ K}$ at varying vapor concentrations: $[\text{acid}] = [\text{base}] = 10^5, 10^6, 10^7, 10^8,$ and $10^9 \text{ molec cm}^{-3}$. Text markers are centered over the data point.

stability decreases, the evaporation of a heterodimer occurs faster than its collision with vapor molecules or other clusters, which results in a reduction in $J_{1.5}$. In contrast, when temperature is held constant and base concentration is varied (Figure 4.8b), the lognormal relationship remains the same across all cases and only the maximum $J_{1.5}$ is shifted until the kinetic limit is reached. The changing relationship between $\Delta G_{\text{heterodimer}}$ and $J_{1.5}$ with varying temperature can be attributed to the change in the thermodynamics of the reaction, while the shift in NPF rate with respect to $\Delta G_{\text{heterodimer}}$ with varying concentration can be attributed to the relatively higher number of collisions in a shorter period of time. This behavior matches the relationship of J with temperature and concentration found in classical nucleation theory (Arstila et al., 1999; Trinkaus, 1983; Vehkamäki et al., 2002):

$$J = Z * p(1, 2) * \exp \left[\frac{-(W - W(1/2))}{RT} \right], \quad (4.2)$$

where J is the nucleation rate, Z is a kinetic pre-factor, W is the work of formation of the critical nucleus, and $p(1, 2)$ and $W(1, 2)$ are number concentration and cluster formation energy, respec-

tively. Concentration is directly proportional to J , whereas temperature contributes from within the exponential expression, which matches the behavior seen in Figure 4.8.

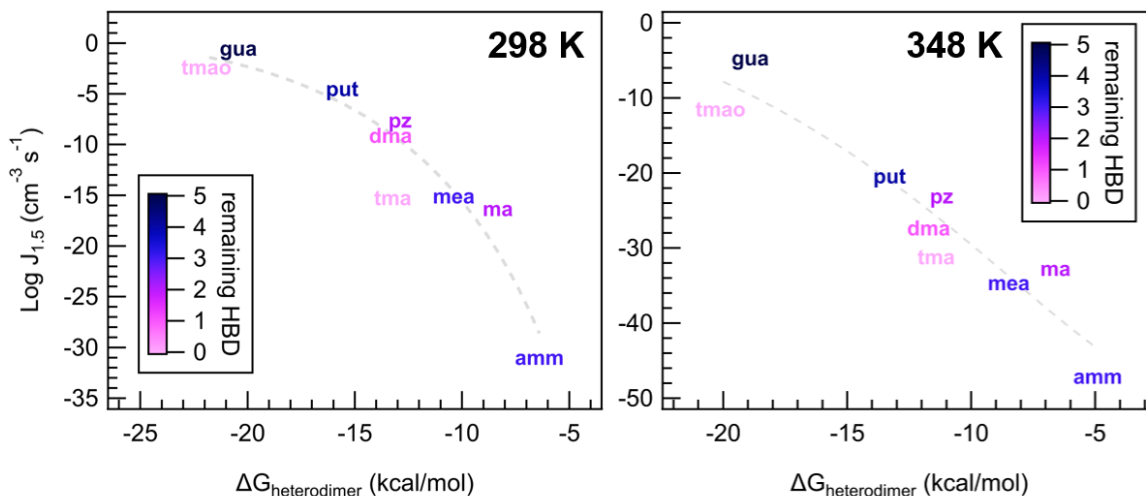


Figure 4.9: Individual data points and trendlines from Figure 4.8a colored according to the number of remaining hydrogen bond donors (HBD) on the heterodimer. The left is data from the 298 K case, and the right is data from the 348 K case, at $[\text{acid}] = [\text{base}] = 10^6 \text{ molec cm}^{-3}$.

Interestingly, as temperature increases, this lognormal relationship transitions to linear, with a larger spread of data points around the trendline. Practically, this implies that $\Delta G_{\text{heterodimer}}$ predicts theoretical $J_{1.5}$ well at cold temperatures, but additional factors become more prominent at warmer temperatures. To understand what processes are important for $J_{1.5}$, we scaled the color on each of the bases to the number of hydrogen bond donors (HBD) remaining on the heterodimer after the proton was transferred at two temperatures (Figure 4.9). The number of remaining HBD was determined by counting the number of polar hydrogens on the base molecule minus the hydrogen donated by sa (if the proton transfer reaction occurred). Although other intermolecular H-bonds exist, those were not subtracted because as the cluster grows, those bonds are broken as the base shifts to accommodate an additional molecule. Sa salts with ma, tmao, put, and gua salts all demonstrate this behavior, where the intermolecular bonds present in the heterodimer for ma, put, and gua are rearranged with each added molecule to the cluster (see Appendix C).

With respect to the lognormal relationship between $J_{1.5}$ and $\Delta G_{\text{heterodimer}}$, tma and tmao, and to a lesser extent, dma, are below the trendline, and they have 0–1 remaining HBD. In contrast, amm,

ma, mea, pz, and put have 2–4 remaining HBD and are closest to the trendline. Gua is the only molecule that has 5 remaining HBD, and consistently has a higher NPF rate than the trendline suggests. This behavior can be attributed to cluster growth being slightly dependent on how well the next molecules can “stick” onto the existing cluster, where if there are more remaining HBD on a cluster, it is easier and faster for the cluster to grow. It is interesting that ma has higher NPF rates than the trendline compared to mea, put, and pz despite having either the same or one fewer HBD, but this may be attributed to the bulkiness of the alkyl groups attached to those amines, which may block the remaining HBD from participating in stabilizing the growing cluster.

These findings are notable in that $\Delta G_{\text{heterodimer}}$ trends consistently with $J_{1.5}$ and deviations from these trendlines can be attributed to structural differences in the base, where a base with more HBD available on the heterodimer would have higher predicted NPF rates than the trendline, with the inverse also being true. However, $\Delta G_{\text{heterodimer}}$ varies strongly with temperature and concentration as described above, and as such is not conducive to predicting $J_{1.5}$, which we attempt to remedy in the following two sections.

A generalized parameterization to predict $J_{1.5}$

In order to combine simulated particle formation rates at different conditions for all acid–base systems, we calculated the heterodimer concentration, which is a function of $\Delta G_{\text{heterodimer}}$, temperature, and the concentration of the gaseous acid and base monomers. The stability of a heterodimer defines its theoretical maximum concentration at given conditions assuming the system is at equilibrium. Assuming mass balance for the heterodimer formation reaction leads to the following concentration under equilibrium conditions:

$$[\text{heterodimer}] = \frac{[\text{acid}][\text{base}]}{C_{\text{ref}}} \exp\left(-\frac{\Delta G_{\text{heterodimer}}}{RT}\right). \quad (4.3)$$

The equilibrium concentration of the heterodimer $[\text{heterodimer}]$ is dependent both on the Gibbs free formation energy $\Delta G_{\text{heterodimer}}$ (calculated at reference concentration $C_{\text{ref}} = \frac{P_{\text{ref}}}{RT}$, where P_{ref} is defined as 1 atm and C_{ref} is in units of molec cm⁻³), and on the monomer concentrations $[\text{acid}]$

and [base]. Here we use heterodimer concentration to estimate $J_{1.5}$ under any (atmospherically relevant) temperature or concentration. However, as different acid–base systems form particles via different pathways depending on acid-to-base ratios, the NPF mechanism may change when either the acid or base is in excess. Thus the derivations here are directly applicable at situations when acid and base concentrations are close to equal.

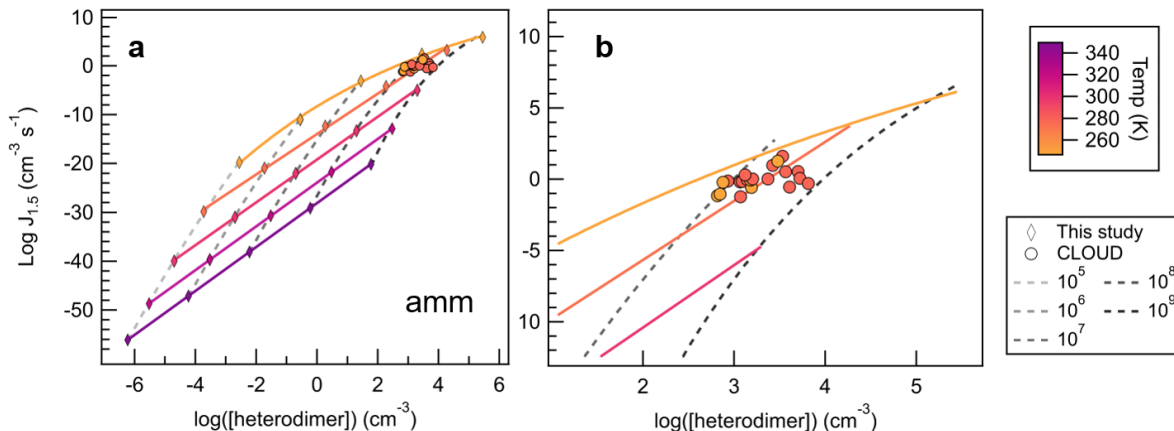


Figure 4.10: Heterodimer concentration plotted against $J_{1.5}$ for sa-amm across 25 computational conditions (filled diamonds) from 248–348 K and monomer concentrations from 10^5 – 10^9 cm^{-3} , where a) shows the full set of conditions calculated for sa-amm, and b) shows a magnification of how CLOUD data compares to the computational dataset. Colored lines correlate to temperature trendlines that were drawn through all data points calculated at the same temperature. Dashed lines represent data points calculated at the same monomer concentrations. We calculated heterodimer concentrations for CLOUD data whose acid and base concentrations were within 50% of each other according to Equation 4.3. All CLOUD data points were collected at temperatures of either 248 or 273 K (colored circles corresponding to color scale) and with monomer concentrations between approx. 10^8 – 10^9 cm^{-3} .

Figure 4.10a shows the temperature and concentration effects on heterodimer concentration for sa-amm salts. As one would expect from Equation 4.3, as concentration increases, heterodimer concentration increases by two orders of magnitude (as reflected in the [heterodimer] term). However, because temperature affects both the calculation of $\Delta G_{\text{heterodimer}}$ and heterodimer concentration, this relationship is not as simple. In general, as temperature decreases, heterodimer concentration increases. As heterodimer concentration increases and temperature decreases, $J_{1.5}$ also increases, though we begin to see $J_{1.5}$ begin to saturate at 248 K and 10^9 cm^{-3} . Through the use of het-

erodimer concentration, we have been able to combine the two factors, temperature and monomer concentration, into one term, where we can now use it to compare (or predict) $J_{1.5}$.

To test the robustness of our calculations, heterodimer concentrations of CLOUD experiments were calculated using Equation 4.3 and this study’s calculated $\Delta G_{\text{heterodimer}}$ values to compare our $J_{1.5}$ calculations to CLOUD’s measured $J_{1.7}$ (Kirkby et al., 2011). Because heterodimer concentration can only be calculated for experiments run at approximately equal acid and base concentrations, all experiments that had more than a 50% difference between monomer concentrations were excluded. Twenty-one measured $J_{1.7}$ values met this criterion and are shown as filled circles in Figure 4.10. When using the closest temperature trendlines (i.e., CLOUD data measured at 273 K was compared to 278 K model trend) to predict the CLOUD data, the difference between the predicted and measured J were within 2 orders of magnitude. On the other hand, if concentration trendlines were used to predict J (i.e, CLOUD vapor concentrations were near 10^8 molec cm^{-3} so the modelled 10^8 molec cm^{-3} trendline was used), differences of up to 4 orders of magnitude occurred. Trendline equations for sa-amm are shown in the Appendix C, as well as difference plots to show the accuracy of the trendlines as discussed.

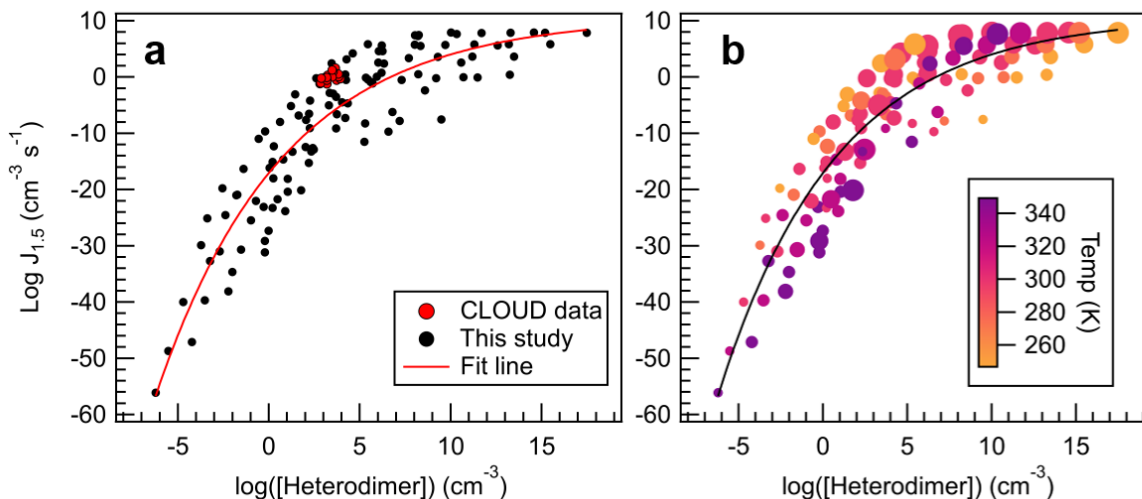


Figure 4.11: Heterodimer concentration plotted against $J_{1.5}$, wherein a) all data are represented with black dots, and b) data points are colored according to temperature and sized to reflect monomer concentrations (10^5 – 10^9 cm^{-3}). Data were fitted to an exponential function, which can be found in Equation 4.4.

All data calculated for this study are plotted in Figure 4.11, which spans 100 K and 5 orders of magnitude in monomer concentrations. Indeed, concentration and temperature effects are minimized compared to the direct comparison between $J_{1.5}$ and $\Delta G_{\text{heterodimer}}$ (Figure 4.8). Because more $J_{1.5}$ were calculated for amm and gua, data points were left as black points to avoid complicating the data. Data were fitted to give the following equation:

$$J_{1.5} = 10.688 - 67.36 \exp\left(\frac{[\text{heterodimer}] + 6.226}{7.0145}\right), \quad (4.4)$$

which can be used as a generalized equation to predict $J_{1.5}$ for acid–base particle formation at any (atmospheric relevant) conditions, given a calculated $\Delta G_{\text{heterodimer}}$ and temperature and concentration. Because $\Delta G_{\text{heterodimer}}$ requires significantly less computational power to calculate than $J_{1.5}$, this trendline provides a method to quickly approximate $J_{1.5}$.

Since the heterodimer concentration is still affected by changes in temperature and concentration, Equation 4.4 is only able to approximate $J_{1.5}$ to within 10 orders of magnitude. This is because of the large range of temperatures and concentrations calculated in this study, where, in general, for concentrations less than 10^7 cm^{-3} and temperatures greater than 298 K, predicted $J_{1.5}$ are below the trendline. Similarly, for concentrations more than 10^7 cm^{-3} and temperatures greater than 298 K, predicted $J_{1.5}$ are above the trendline, which can be seen in Figure 4.11b.

Though the 10 orders of magnitude uncertainty is large, Pierce and Adams (2009) have shown that 6 orders of magnitude uncertainty in new particle formation events in the atmosphere only contributed to a difference of 17% in modeled concentrations of cloud condensation nuclei (CCN) in the troposphere. Considering the simplicity of this calculation, this approach may improve estimates of global CCN in models that are limited by the computational expense of calculating $J_{1.5}$.

4.4.4 System-specific parameterization for weak bases using normalized heterodimer concentration (Φ)

Here we attempt to reduce this uncertainty for nine salts of sa and further simplify the expression used to calculate $J_{1.5}$. We accomplish this by incorporating heterodimer concentration and monomer concentrations into a new independent variable, the normalized heterodimer concentration, Φ :

$$\Phi = \frac{[\text{heterodimer}]}{\left(\frac{[\text{acid}][\text{base}]}{C_{\text{ref}}}\right)^{1/2}}, \quad (4.5)$$

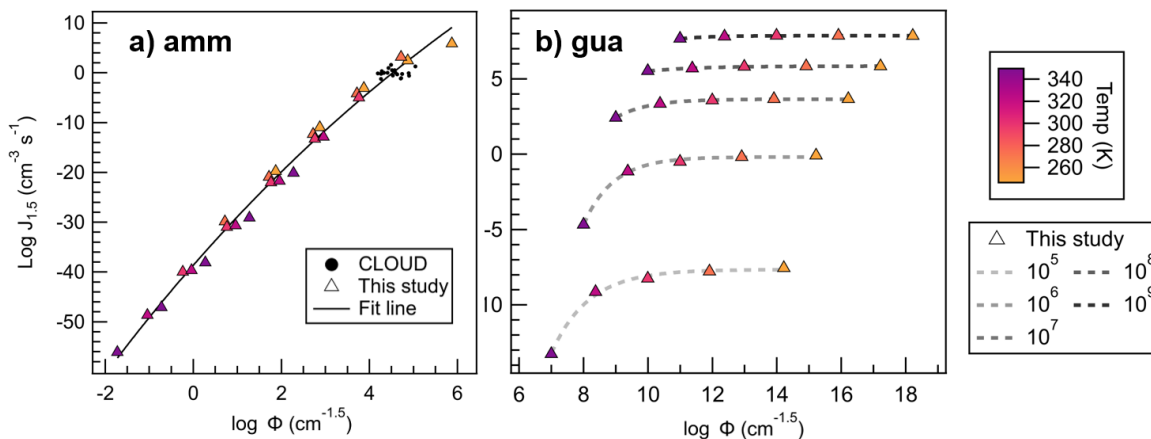


Figure 4.12: A) Amm and b) gua sa salts' $J_{1.5}$ plotted against Φ , where triangles are colored according to the temperature of that point's calculation. CLOUD data are shown as black dots, and their Φ values were calculated according to Equation 4.5. All trendlines used an exponential fit.

When applied to ammonia, a simple monotonic relationship between Φ and $J_{1.5}$ becomes immediately apparent (Figure 4.12a). Here we observe that temperature affects the value of Φ minimally, and that the effects of temperature and concentration are incorporated in the dependent variable resulting in relatively minor data spread. Again, CLOUD Φ values were calculated for comparison, and CLOUD data are all predicted within 2 orders of magnitude of the best exponential fit to the data (fit equation available in the Appendix C). The dispersion in $J_{1.5}$ remains constant over all conditions explored.

As a contrast to the sa-amm system, we also examined the behavior of the sa-gua salt, a strong-acid and strong-base combination. Figure 4.12b shows that a monotonic relationship does not apply for such systems. In fact, at each concentration, $J_{1.5}$ quickly reaches the kinetic limit and remains constant with temperature once monomer concentrations are above 10^7 cm^{-3} . Gua is likely insensitive to changes in temperature because gua is a strong base and forms more stable growing clusters than those of ammonia. In addition, at higher concentrations than 10^7 cm^{-3} , collisions are occurring so quickly that if the cluster evaporates a monomer, another monomer is able to readily take its place. In this way, gua salt $J_{1.5}$ are largely dictated by monomer concentration rather than temperature.

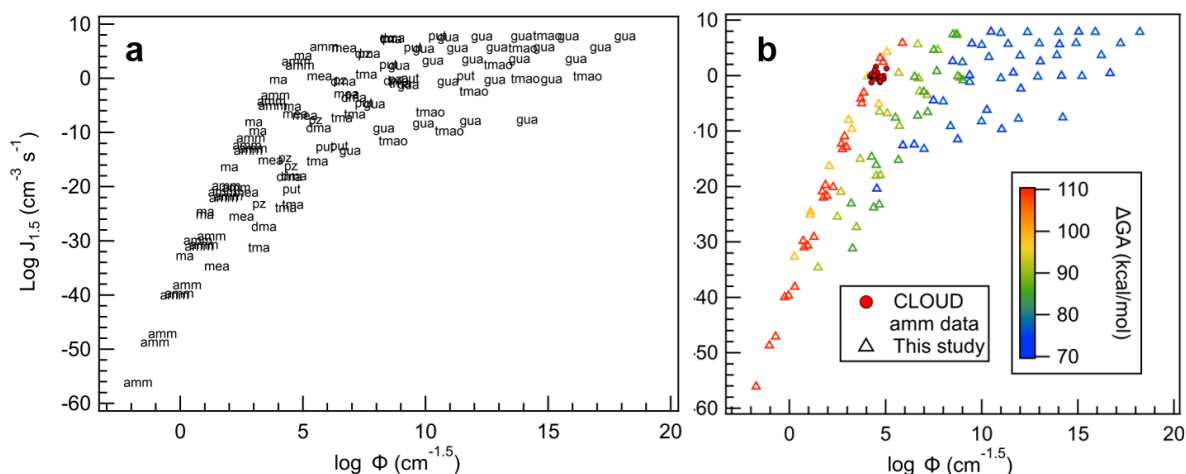


Figure 4.13: All sa salts plotted with a) base names as markers and b) markers colored according to their ΔGA values. CLOUD observations are shown as filled circles.

When Φ is compared to $J_{1.5}$ for all bases (Figure 4.13a), we can immediately see that, in general, each base follows a unique trendline. Additionally, more bases follow the more monotonic behavior of sa-amm than sa-gua and increase in the data dispersion follows increasing basicity. This is apparent when each of the base datapoints are colored according to their ΔGA values (Figure 4.13b). In general, the larger ΔGA values correspond to more linear, less dispersed relationships between $J_{1.5}$ and Φ , and as ΔGA decreases, $J_{1.5}$ begin to saturate and dispersion increases. This change in behavior seems occur most dramatically as ΔGA decreases below 90 kcal/mol for the conditions shown here; however, it is likely for larger concentrations or lower temperatures, even

the weakest of bases will saturate. The fact that ΔGA is directly linked to $J_{1.5}$ saturation highlights how acid and base strength are crucial to understanding cluster formation and growth into particles.

Here, Φ can be used to predict $J_{1.5}$ relatively accurately for specific bases, as demonstrated by the CLOUD $J_{1.7}$ observations. However, for bases with ΔGA below approximately 90 kcal/mol, prediction becomes more uncertain as the kinetic limit becomes easier to reach. This ΔGA cutoff of 90 kcal/mol means that the most abundant bases in the atmosphere, amm, ma, dma, and tma, are not expected to saturate in this model under atmospheric conditions and thus their $J_{1.5}$ can be approximated relatively accurately using the results of this study. While this can only be used for experiments with acid and base monomer concentrations within 50% of each other over the concentrations and temperatures studied, this is a powerful predictive tool using only the term, Φ , which only requires the calculation of one computational parameter, $\Delta G_{\text{heterodimer}}$.

Because each base has its own correlation between Φ and $J_{1.5}$, the trendlines here cannot be generalized to bases that are not described. For those bases not described here, Equation 4.4 should be used to approximate $J_{1.5}$ to within 10 orders of magnitude.

4.5 Conclusions

Here we have shown that heterodimer stability is largely predicted by the gas-phase acidity of the constituent acid and base across 27 acid–base pairs. In addition, we found that trends between heterodimer stability and physical properties such as volatility, dipole moment, and polarizability did not hold for the wide variety of bases studied here, despite a trend existing for the smaller set of amm, ma, dma, and tma. We emphasize here the importance of studying a variety of bases with different structures and physical properties in order to make sure our understanding of salt NPF remains unbiased. We have also shown the relationship between $J_{1.5}$ and heterodimer stability and how it was affected by temperature and concentration. We show that deviations from the lognormal relationship were attributed to the remaining HBD available on the base molecule on the heterodimer. Then in order to devise a simple model to predict $J_{1.5}$, we calculated heterodimer concentration from

our heterodimer stability values. The effects of temperature and concentration on heterodimer concentration were much less than that of those on $\Delta G_{\text{heterodimer}}$ but still were present, as shown by the 25 different calculations of sa-amm $J_{1.5}$. When compared to CLOUD experimental $J_{1.7}$ data, the sa-amm trendlines were able to predict $J_{1.5}$ within two orders of magnitude when the closest temperature trendline was used. We found that heterodimer concentration can be parameterized into an expression that can predict $J_{1.5}$. Because of this, the more difficult to calculate parameter of $J_{1.5}$ could be replaced by the more easily acquired parameter of heterodimer stability. In addition, we have calculated a new parameter, the normalized heterodimer concentration, Φ , which minimized the effects of temperature and concentration even more than that of heterodimer concentration. We found that Φ reduces the complexity of calculating $J_{1.5}$ by producing a single, monotonic trendline for sa-amm, instead of 10 as it was for our calculations using heterodimer concentration as the independent variable. The ability of Φ to accurately predict $J_{1.5}$ applies to sa salts of weaker bases, as stronger bases quickly saturated to reach the kinetic limit. This behavior was exhibited more strongly for salts that had a ΔGA value smaller than 90 kcal/mol.

In addition, we have presented a facile way of predicting $J_{1.5}$ to within 10 orders of magnitude for salts of sa using a generalized parameterization (Equation 4.4). We also present a method to more accurately predict $J_{1.5}$ using the new parameter Φ for the nine sa salts studied here. It is important to note that, due to computational restrictions, all particle formation simulations are performed for two-component neutral clusters with an absence of relative humidity. Thus theoretical results might vary compared to measured particle formation under atmospheric or laboratory conditions. Water enhancement of NPF is known to be greater with more available hydrogen bonding sites as shown in Yang et al. (2018), which may enhance the deviation from the lognormal relationship that was attributed to remaining HBD on the heterodimer. The enhancing effect of ions on the NPF rate can be several orders of magnitude for systems where small neutral clusters are unstable (e.g., ammonium salts in this study), but is negligible with more stable clusters, like a strong acid and base pair (Myllys et al., 2019b). In addition, when more than two components are present at the same time in the atmosphere or even as a contaminant in laboratory, NPF can be largely enhanced due to synergistic effects (Myllys et al., 2019b; Jen et al., 2014b; Yu et al., 2012a; Temelso

et al., 2018; Glasoe et al., 2015). It is infeasible to explicitly study of all possible combinations of multi-component acid and base mixtures, but perhaps in the future the synergy between different compounds and the role of water vapor could be estimated using some simple parameters such as GA values and number of hydrogen bonding sites.

Chapter 5

Conclusions and Future Perspectives

5.1 Conclusions

We have measured acid:base ratio as a function of diameter for particles generated from the reaction of an acid and base, focusing on a variety of chemical systems that include both volatile and nonvolatile reactants. In our first study, we measured the composition of nanoparticles made from sulfuric acid and ammonia or dimethylamine under dry and humid conditions. For the $\text{H}_2\text{SO}_4\text{-NH}_3$ system, nanoparticles were acidic, with acid:base ratios that increased with decreased particle size. Particles larger than 12 nm were fully neutralized with acid:base ratios ~ 1 , but 7 nm particles had ratios of ~ 3.5 . There were no differences observed in this ratio between dry and humid (60% RH) conditions. In contrast, nanoparticles generated from the $\text{H}_2\text{SO}_4\text{-DMA}$ system showed a very different dependence of acid:base ratio with size under dry and humid conditions. Under both dry and humid conditions, 14-20 nm particles were slightly acidic with acid:base ratios of ~ 0.5 , corresponding to dimethylammonium bisulfate. Under dry conditions, particles actually become more basic at sizes below 14 nm with an acid:base ratio that reached a minimum of ~ 0.25 at 11 nm, and then increased to ~ 0.6 at 9 nm. Under humid conditions, sub-12 nm particles were more acidic than larger particles, reaching a maximum ratio of ~ 1.3 for 9 nm particles. We conclude

that nanoparticle physical and chemical properties can affect the relative acidity or basicity of these compounds, which affects their proton transfer efficiency. When we model this behavior based on the measured acid:base ratios, we can qualitatively account for the increase in acidity with decreased particle size by shifting pK_a values by +3.5 and -3.5 units for the reacting acid and base, respectively. We therefore hypothesize that nanoparticles possess a unique environment wherein the acid and the base are less efficient at acid-base chemistry and the fraction of the more volatile base in its neutral form efficiently partitions back to the gas phase and is no longer available to participate in proton transfer.

In contrast to the above system involving a non-volatile acid with a volatile base, we found in our second study that a volatile acid reacting with a volatile base results in particles that are fully neutralized. Acid:base ratios are constant with particle diameter because proton transfer is the governing mechanism by which the acid and base are incorporated into a nanoparticle. We measured the composition of nanoparticles formed from nitric acid and dimethylamine under dry and humid (55% RH) conditions and found that particles remained at a neutral acid:base ratio of ~ 1 over our measurement range of 9-30 nm in diameter. Here, instead of thermodynamic modelling, we used quantum chemical methods to calculate the binding energies of clusters up to 4 acid and 4 base molecules and used a cluster dynamics model to identify the most stable clusters. We found that the most stable cluster compositions of acid and base can be reasonably extrapolated to nanoparticle composition for the volatile/volatile pairing of acid and base, but not necessarily for nonvolatile/volatile pairing such as those discussed in the previous paragraph. The model also sheds light on why particles formed from the $\text{H}_2\text{SO}_4\text{-NH}_3$ system had a higher acid:base ratio compared to the $\text{H}_2\text{SO}_4\text{-DMA}$ system, as sulfuric acid is able to stabilize itself in clusters with ammonia because of the plethora of available H-bonding sites.

Throughout the course of this thesis research, we have explored diverse chemical systems and have observed varying degrees of new particle formation that result from acid-base chemistry. In the final study of this thesis, we employed computational techniques and determined that the stability of the acid-base pair, which we refer to as the heterodimer, is the best predictor of nanoparticle formation rate. Using a dataset consisting of over 27 total acid-base pairings made up of salts of sulfuric, nitric,

and methanesulfonic acid with nine bases, we explored the factors that affect heterodimer stability and found that the strongest predictor is the difference in gas-phase acidity between acid and base. Aqueous phase acidity also predicted heterodimer stability, with the outlier of salts of a zwitterion amine, TMAO, which has radically different behavior in the gas vs aqueous phase. Interestingly, vapor pressure, dipole moment, and polarizability did not trend with heterodimer stability, which introduces a more nuanced idea that vapor pressure may play a role in nanoparticle composition and growth, but not necessarily cluster formation, and therefore, nucleation. In addition to these molecular insights, we studied the ability of heterodimer stability to predict nucleation rates for sulfuric acid salts. This resulted in a model that predicts NPF rates for any system in which sulfuric acid reacts with a weak base such as ammonia or an amine. This model covers a range of monomer concentrations from 10^5 to 10^9 molec cm^{-3} and temperatures from 248 to 348 K, and agrees with laboratory measurements to within two orders of magnitude. This accuracy is sufficient as to allow incorporation of this parametrization in global models.

5.2 Future Work

Future work in understanding salt nanoparticle composition should focus on characterizing the extent to which other physical properties are changing the behavior of the acid-base pairs (e.g., ionic strength, H-bond participators, number of protons available for proton transfer, etc.). Indeed, this would be aided by development of instrumentation that can probe smaller sizes, as well as development of models and computing that can probe larger sizes. Ultimately, our understanding of nanoparticle behavior depends on real-world measurements of nanoparticle composition as well as first-principles models to isolate what physical properties determine that composition.

Modelling is crucial because of two reasons: 1) the physical limitations of instruments are such that we cannot directly measure every physical property of the environment within a nanoparticle, and 2) the possible combinations of acids and bases in the atmosphere are such that it is impractical to rely solely on experimental data (even if we could measure the aforementioned environments),

whereas modelling would be much faster and more efficient. The advent of machine learning also can speed up the model development process given sufficient data for training.

However, this is not to understate the importance of having instrumentation that can provide a benchmark for how real-world nanoparticles behave. Indirect approaches to measuring nanoparticle composition, like hygroscopicity tandem differential mobility analyzers or their volatility counterparts (HTDMAs/VTDMAs) are able to probe the chemical environments of particles small enough to be modelled. Developments in tools to concentrate nanoparticles for analysis can help overcome the sample mass challenge for the TDCIMS as well.

The development of both instrumentation and modelling techniques could open up ways to answer outstanding questions left from these studies, which include: Why were the acid:base ratios of $\text{H}_2\text{SO}_4\text{-NH}_3$ nanoparticles so acidic, with almost four acid molecules per ammonia, despite the presence of 100x more base? Why do $\text{H}_2\text{SO}_4\text{-DMA}$ particles, under dry conditions, form more basic nanoparticles between the sizes of 9–14 nm? Current cluster modelling and measurements do not capture the acid:base ratios measured in nanoparticles in this work, and certainly, a fundamental understanding of salt nanoparticle behavior is still a gap in our knowledge base.

Future work can also iterate upon our model of nucleation rates of salt systems to improve prediction accuracy and to broaden the number of different systems that it can be applied to. This can provide more accurate predictions of new particle formation in global models, as well as help guide laboratory experiments to focus on particle-producing systems, rather than systems that do not form particles. In addition, this model is restricted to specific environmental conditions that are rarely atmospherically relevant (i.e., approximately equal acid and base concentrations, 0% RH). It is possible that further modelling can capture how these systems change in NPF behavior with less restrictive environmental conditions, which can then broaden the applicability of the current parametrization. Indeed, it will be interesting to learn if models can reflect the measured NPF rates in the presence of water, or even the NPF of multi-component acid-base systems.

Bibliography

- Estimation Programs Interface Suite™ for Microsoft® Windows, v 4.11. United States Environmental Protection Agency, Washington, DC, USA.
- Apfel, B. R., Wall, S. M., Tokiwa, Y., and Haik, M.: Simultaneous nitric acid, particulate nitrate, and acidity measurements in ambient air, *Atmospheric Environment*, 14, 549–554, 1979.
- Allen, J. L., Oberdörster, G., Morris-schaffer, K., Wong, C., Klocke, C., Sobolewski, M., Conrad, K., Mayer-Proschel, M., and Cory-slechta, D. A.: Developmental Neurotoxicity of Inhaled Ambient Ultrafine Particle Air Pollution: Parallels with Neuropathological and Behavioral Features of Autism and Other Neurodevelopmental Disorders, *Neurotoxicology*, 59, 140–154, <https://doi.org/10.1016/j.neuro.2015.12.014>. Developmental, 2017.
- Almeida, J., Schobesberger, S., Kürten, A., Ortega, I. K., Kupiainen-Määttä, O., Praplan, A. P., Adamov, A., Amorim, A., Bianchi, F., Breitenlechner, M., David, A., Dommen, J., Donahue, N. M., Downard, A., Dunne, E., Duplissy, J., Ehrhart, S., Flagan, R. C., Franchin, A., Guida, R., Hakala, J., Hansel, A., Heinritzi, M., Henschel, H., Jokinen, T., Junninen, H., Kajos, M., Kangasluoma, J., Keskinen, H., Kupc, A., Kurtén, T., Kvashin, A. N., Laaksonen, A., Lehtipalo, K., Leiminger, M., Leppä, J., Loukonen, V., Makhmutov, V., Mathot, S., McGrath, M. J., Nieminen, T., Olenius, T., Onnela, A., Petäjä, T., Riccobono, F., Riipinen, I., Rissanen, M., Rondo, L., Ruuskanen, T., Santos, F. D., Sarnela, N., Schallhart, S., Schnitzhofer, R., Seinfeld, J. H., Simon, M., Sipilä, M., Stozhkov, Y., Stratmann, F., Tomé, A., Tröstl, J., Tsagkogeorgas, G., Vaattovaara, P., Viisanen, Y., Virtanen, A., Vrtala, A., Wagner, P. E., Weingartner, E., Wex, H., Williamson, C., Wimmer, D., Ye, P., Yli-Juuti, T., Carslaw, K. S., Kulmala, M., Curtius, J., Baltensperger, U., Worsnop, D. R., Vehkamäki, H., and Kirkby, J.: Molecular understanding of sulphuric acid–amine particle nucleation in the atmosphere, *Nature*, 502, 359–363, <https://doi.org/10.1038/nature12663>, 2013a.
- Almeida, J., Schobesberger, S., Kürten, A., Ortega, I. K., Kupiainen-Määttä, O., Praplan, A. P., Adamov, A., Amorim, A., Bianchi, F., Breitenlechner, M., and *et al.*: Molecular Understanding of Sulphuric Acid–Amine Particle Nucleation in the Atmosphere, *Nature*, 502, 359–363, 2013b.
- Angelino, S., Suess, D. T., and Prather, K. A.: Formation of Aerosol Particles from Reactions of Secondary and Tertiary Alkylamines: Characterization by Aerosol Time-of-Flight Mass Spectrometry, *Environ. Sci. Technol.*, 35, 3130–3138, <https://doi.org/10.1021/ES0015444>, 2001.
- Arden Pope III, C. and Dockery, D. W.: Health Effects of Fine Particulate Air Pollution: Lines that Connect, *Journal of the Air & Waste Management Association*, 56, 709–742, <https://doi.org/10.1080/10473289.2006.10464485>, 2012.

- Arquero, K. D., Xu, J., Gerber, R. B., and Finlayson-Pitts, B. J.: Particle formation and growth from oxalic acid, methanesulfonic acid, trimethylamine and water: A combined experimental and theoretical study, *Physical Chemistry Chemical Physics*, 19, 28 286–28 301, <https://doi.org/10.1039/c7cp04468b>, 2017a.
- Arquero, K. D., Xu, J., Gerber, R. B., and Finlayson-Pitts, B. J.: Particle formation and growth from oxalic acid, methanesulfonic acid, trimethylamine and water: A combined experimental and theoretical study, *Physical Chemistry Chemical Physics*, 19, 28 286–28 301, <https://doi.org/10.1039/c7cp04468b>, 2017b.
- Arstila, H., Korhonen, P., and Kulmala, M.: Ternary nucleation: Kinetics and application to water-ammonia-hydrochloric acid system, *Journal of Aerosol Science*, 30, 131–138, [https://doi.org/10.1016/S0021-8502\(98\)00033-0](https://doi.org/10.1016/S0021-8502(98)00033-0), 1999.
- Aston, B. J. G., Eidinoff, M. L., and Forster, W. S.: The Heat Capacity and Entropy, Heats of Fusion and Vaporization and the Vapor Pressure of Dimethylamine, *Journal of the American Chemical Society*, 61, 1539–1543, <https://doi.org/10.1021/ja01875a061>, 1939.
- Aston, J. G., Siller, C. W., and Messerly, G. H.: Heat Capacities and Entropies of Organic Compounds. III. Methylamine from 11.5°K. To the Boiling Point. Heat of Vaporization and Vapor Pressure. The Entropy from Molecular Data, *Journal of the American Chemical Society*, 59, 1743–1751, <https://doi.org/10.1021/ja01288a054>, 1937.
- Baccarini, A., Karlsson, L., Dommen, J., Duplessis, P., Vüllers, J., Brooks, I. M., Saiz-Lopez, A., Salter, M., Tjernström, M., Baltensperger, U., Zieger, P., and Schmale, J.: Frequent new particle formation over the high Arctic pack ice by enhanced iodine emissions, *Nature Communications*, 11, 1–11, <https://doi.org/10.1038/s41467-020-18551-0>, 2020.
- Ball, S. M., Hanson, D. R., Eisele, F. L., and McMurry, P. H.: Laboratory studies of particle nucleation: Initial results for H₂SO₄, H₂O, and NH₃ vapors, *Journal of Geophysical Research: Atmospheres*, 104, 23 709–23 718, <https://doi.org/10.1029/1999JD900411>, 1999.
- Barsanti, K. C., McMurry, P. H., and Smith, J. N.: The potential contribution of organic salts to new particle growth, *Atmospheric Chemistry and Physics*, 9, 2949–2957, <https://doi.org/10.5194/acp-9-2949-2009>, 2009.
- Behera, S. N., Sharma, M., Aneja, V. P., and Balasubramanian, R.: Ammonia in the atmosphere: a review on emission sources , atmospheric chemistry and deposition on terrestrial bodies, *Environ. Sci. Pollut. Res.*, 20, 8092–8131, <https://doi.org/10.1007/s11356-013-2051-9>, 2013.
- Benson, D. R., Erupe, M. E., and Lee, S. H.: Laboratory-measured H₂SO₄-H₂O-NH₃ ternary homogeneous nucleation rates: Initial observations, *Geophysical Research Letters*, 36, <https://doi.org/10.1029/2009GL038728>, 2009.
- Berndt, T., Stratmann, F., Sipilä, M., Vanhanen, J., Petäjä, T., Mikkilä, J., Uner, A. G., Spindler, G., Lee, R., Iii, M., Curtius, J., Kulmala, M., and Heintzenberg, J.: Laboratory study on new particle formation from the reaction OH + SO₂ : influence of experimental conditions, H₂O vapour, NH₃ and the amine tert-butylamine on the overall process, *Atmos. Chem. Phys. Atmospheric Chemistry and Physics*, 10, 7101–7116, <https://doi.org/10.5194/acp-10-7101-2010>, 2010.

- Berndt, T., Sipilä, M., Stratmann, F., Petäjä, T., Vanhanen, J., Mikkilä, J., Patokoski, J., Taipale, R., Lee Mauldin III, R., and Kulmala, M.: Enhancement of atmospheric H₂SO₄/H₂O nucleation: organic oxidation products versus amines, *Atmospheric Chemistry and Physics Discussions*, 13, 16 301–16 335, <https://doi.org/10.5194/acpd-13-16301-2013>, 2013.
- Besel, V., Kubečka, J., Kurtén, T., and Vehkamäki, H.: Impact of Quantum Chemistry Parameter Choices and Cluster Distribution Model Settings on Modeled Atmospheric Particle Formation Rates, *The Journal of Physical Chemistry A*, 124, 5931–5943, 2020.
- Bianchi, F., Praplan, A. P., Sarnela, N., Dommen, J., Kürten, A., Ortega, I. K., Schobesberger, S., Junninen, H., Simon, M., Tröstl, J., Jokinen, T., Sipilä, M., Adamov, A., Amorim, A., Almeida, J., Breitenlechner, M., Duplissy, J., Ehrhart, S., Flagan, R. C., Franchin, A., Hakala, J., Hansel, A., Heinritzi, M., Kangasluoma, J., Keskinen, H., Kim, J., Kirkby, J., Laaksonen, A., Lawler, M. J., Lehtipalo, K., Leiminger, M., Makhmutov, V., Mathot, S., Onnela, A., Petäjä, T., Riccobono, F., Rissanen, M. P., Rondo, L., Tomé, A., Virtanen, A., Viisanen, Y., Williamson, C., Wimmer, D., Winkler, P. M., Ye, P., Curtius, J., Kulmala, M., Worsnop, D. R., Donahue, N. M., and Baltensperger, U.: Insight into Acid–Base Nucleation Experiments by Comparison of the Chemical Composition of Positive, Negative, and Neutral Clusters, *Environmental Science & Technology*, 48, 13 675–13 684, <https://doi.org/10.1021/es502380b>, 2014.
- Bianchi, F., Tröstl, J., Junninen, H., Frege, C., Henne, S., Hoyle, C. R., Molteni, U., Herrmann, E., Adamov, A., Bukowiecki, N., Chen, X., Duplissy, J., Gysel, M., Hutterli, M., Kangasluoma, J., Kontkanen, J., Kürten, A., Manninen, H. E., Münch, S., Peräkylä, O., Petäjä, T., Rondo, L., Williamson, C., Weingartner, E., Curtius, J., Worsnop, D. R., Kulmala, M., Dommen, J., and Baltensperger, U.: New particle formation in the free troposphere: A question of chemistry and timing, *Science*, 352, 1109–1112, <https://doi.org/10.1126/science.aad5456>, 2016.
- Braban, C. F., Abbatt, J. P. D., and Cziczo, D. J.: Deliquescence of Ammonium Sulfate Particles at Sub-Eutectic Temperatures, *Geophysical Research Letters*, 28, 3879–3882, 2001.
- Brooks, S. D., Wise, M. E., Cushing, M., and Tolbert, M. A.: Deliquescence behavior of organic / ammonium sulfate aerosol, 29, 2–5, <https://doi.org/10.1029/2002GL014733>, 2002.
- Brus, D., Hyvärinen, A. P., Viisanen, Y., Kulmala, M., and Lihavainen, H.: Homogeneous nucleation of sulfuric acid and water mixture: Experimental setup and first results, *Atmospheric Chemistry and Physics*, 10, 2631–2641, <https://doi.org/10.5194/acp-10-2631-2010>, 2010.
- Bzdek, B. R., Ridge, D. P., and Johnston, M. V.: Size-Dependent Reactions of Ammonium Bisulfate Clusters with Dimethylamine, *The Journal of Physical Chemistry A*, 114, 11 638–11 644, <https://doi.org/10.1021/jp106363m>, 2010.
- Bzdek, B. R., Ridge, D. P., and Johnston, M. V.: Amine reactivity with charged sulfuric acid clusters, *Atmos. Chem. Phys.*, pp. 8735–8743, <https://doi.org/10.5194/acp-11-8735-2011>, 2011.
- Bzdek, B. R., Zordan, C. A., Pennington, M. R., Luther, G. W., and Johnston, M. V.: Quantitative Assessment of the Sulfuric Acid Contribution to New Particle Growth, *Environmental Science & Technology*, 46, 4365–4373, <https://doi.org/10.1021/es204556c>, 2012.
- Bzdek, B. R., Horan, A. J., Pennington, M. R., DePalma, J. W., Zhao, J., Jen, C. N., Hanson, D. R., Smith, J. N., McMurry, P. H., and Johnston, M. V.: Quantitative and time-resolved

- nanoparticle composition measurements during new particle formation, *Faraday Discussions*, 165, 25–43, <https://doi.org/10.1039/c3fd00039g>, 2013.
- Bzdek, B. R., DePalma, J. W., and Johnston, M. V.: Mechanisms of Atmospherically Relevant Cluster Growth, *Accounts of Chemical Research*, 50, 1965–1975, <https://doi.org/10.1021/acs.accounts.7b00213>, 2017.
- Cai, R. and Jiang, J.: A new balance formula to estimate new particle formation rate: reevaluating the effect of coagulation scavenging, *Atmos. Chem. Phys.*, 17, 12 659–12 675, 2017.
- Cass, G. R., Hughes, L. A., Bhave, P., Kleeman, M. J., Allen, J. O., and Salmon, L. G.: The chemical composition of atmospheric ultrafine particles, *Philosophical Transactions of the Royal Society A: Mathematical, Physical and Engineering Sciences*, 358, 2581–2592, <https://doi.org/10.1098/rsta.2000.0670>, 2000.
- Chai, J.-d. and Head-Gordon, M.: Long-range corrected hybrid density functionals with damped atom – atom dispersion corrections, *Physical Chemistry Chemical Physics*, 10, 6615–6620, <https://doi.org/10.1039/b810189b>, 2008.
- Chan, L. P. and Chan, C. K.: Displacement of Ammonium from Aerosol Particles by Uptake of Triethylamine, 6826, <https://doi.org/10.1080/02786826.2011.618815>, 2012.
- Chan, L. P. and Chan, C. K.: Role of the Aerosol Phase State in Ammonia/Amines Exchange Reactions, *Environmental Science & Technology*, 47, 5755–5762, <https://doi.org/10.1021/es4004685>, 2013.
- Chan, T. and Mozurkewich, M.: Measurement of the Coagulation Rate Constant for Sulfuric Acid Particles as a Function of Particle Size Using Tandem Differential Mobility Analysis, *Journal of Aerosol Science*, 32, 321–339, [https://doi.org/10.1016/S0021-8502\(00\)00081-1](https://doi.org/10.1016/S0021-8502(00)00081-1), 2001.
- Chattopadhyay, S. and Ziemann, P. J.: Vapor Pressures of Substituted and Unsubstituted Monocarboxylic and Dicarboxylic Acids Measured Using an Improved Thermal Desorption Particle Beam Mass Spectrometry Method, 6826, <https://doi.org/10.1080/02786820500421547>, 2007.
- Chee, S., Myllys, N., Barsanti, K. C., Wong, B. M., and Smith, J. N.: An Experimental and Modeling Study of Nanoparticle Formation and Growth from Dimethylamine and Nitric Acid, *J. Phys. Chem. A*, 123, 5640–5648, <https://doi.org/10.1021/acs.jpca.9b03326>, 2019.
- Chen, D. R. and Pui, D. Y.: A high efficiency, high throughput unipolar aerosol charger for nanoparticles, *Journal of Nanoparticle Research*, 1, 115–126, <https://doi.org/10.1023/A:1010087311616>, 1999.
- Chen, H. and Finlayson-Pitts, B. J.: New Particle Formation from Methanesulfonic Acid and Amines/Ammonia as a Function of Temperature, *Environmental Science and Technology*, 51, 243–252, <https://doi.org/10.1021/acs.est.6b04173>, 2017.
- Chen, H., Chee, S., Lawler, M. J., Barsanti, K. C., Wong, B. M., and Smith, J. N.: Size resolved chemical composition of nanoparticles from reactions of sulfuric acid with ammonia and dimethylamine, *Aerosol Science and Technology*, 52, 1120–1133, <https://doi.org/10.1080/02786826.2018.1490005>, 2018.

- Chen, M., Titcombe, M., Jiang, J., Jen, C., Kuang, C., Fischer, M. L., Eisele, F. L., Siepmann, J. I., Hanson, D. R., Zhao, J., and McMurry, P. H.: Acid-base chemical reaction model for nucleation rates in the polluted atmospheric boundary layer, *Proceedings of the National Academy of Sciences of the United States of America*, 109, 18 713–18 718, <https://doi.org/10.1073/pnas.1210285109>, 2012.
- Cheng, C., Huang, Z., Chan, C. K., Chu, Y., Li, M., Zhang, T., Ou, Y., and Chen, D.: Characteristics and mixing state of amine-containing particles at a rural site in the Pearl River Delta, China, *Atmospheric Chemistry and Physics*, pp. 9147–9159, 2018.
- Cheng, Y., Su, H., Koop, T., Mikhailov, E., and Pöschl, U.: Size dependence of phase transitions in aerosol nanoparticles, *Nature Communications*, 6, 5923, <https://doi.org/10.1038/ncomms6923>, 2015.
- Clegg, S. L., Brimblecombe, P., and Wexler, A. S.: Extended AIM Aerosol Thermodynamics Model, URL <http://www.aim.env.uea.ac.uk/aim/aim.php>.
- Dada, L., Ylivinkka, I., Baalbaki, R., Li, C., Guo, Y., Yan, C., Yao, L., Sarnela, N., Jokinen, T., Daellenbach, K. R., Yin, R., Deng, C., Chu, B., Nieminen, T., Wang, Y., Lin, Z., Thakur, R. C., Kontkanen, J., Stolzenburg, D., Sipilä, M., Hussein, T., Paasonen, P., Bianchi, F., Salma, I., Weidinger, T., Pikridas, M., Sciare, J., Jiang, J., Liu, Y., Petäjä, T., Kerminen, V.-M., and Kulmala, M.: Sources and sinks driving sulfuric acid concentrations in contrasting environments: implications on proxy calculations, *Atmos. Chem. Phys*, 20, 11 747–11 766, 2020.
- Dawson, M. L., Varner, M. E., Perraud, V., Ezell, M. J., Gerber, R. B., and Finlayson-Pitts, B. J.: Simplified mechanism for new particle formation from methanesulfonic acid, amines, and water via experiments and ab initio calculations, *Proceedings of the National Academy of Sciences of the United States of America*, 109, 18 719–18 724, <https://doi.org/10.1073/pnas.1211878109>, 2012.
- DePalma, J. W., Bzdek, B. R., Doren, D. J., and Johnston, M. V.: Structure and Energetics of Nanometer Size Clusters of Sulfuric Acid with Ammonia and Dimethylamine, *The Journal of Physical Chemistry A*, 116, 1030–1040, <https://doi.org/10.1021/jp210127w>, 2012.
- Dockery, D. W., Arden Pope III, C., Xu, X., Spengler, J. D., Ware, J. H., Fay, M. E., Ferris, B. G., and Speizer, F. E.: An Association Between Air Pollution and Mortality In Six U.S. Cities, *The New England Journal of Medicine*, 329, 1753–1759, 1993.
- Donahue, N. M., Ortega, I. K., Chuang, W., Riipinen, I., Riccobono, F., Schobesberger, S., Dommen, J., Baltensperger, U., Kulmala, M., Worsnop, D. R., and Vehkamäki, H.: How do organic vapors contribute to new-particle formation?, *Faraday Discussions*, 165, 91–104, <https://doi.org/10.1039/c3fd00046j>, 2013.
- Duplissy, J., Merikanto, J., Franchin, A., Tsagkogeorgas, G., Kangasluoma, J., Wimmer, D., Vuollekoski, H., Schobesberger, S., Lehtipalo, K., Flagan, R. C., Brus, D., Donahue, N. M., Vehkamäki, H., Almeida, J., Amorim, A., Barmet, P., Bianchi, F., Breitenlechner, M., Dunne, E. M., Guida, R., Henschel, H., Junninen, H., Kirkby, J., Kürten, A., Kupc, A., Määttä, A., Makhmutov, V., Mathot, S., Nieminen, T., Onnela, A., Praplan, A. P., Riccobono, F., Rondo, L., Steiner, G., Tome, A., Walther, H., Baltensperger, U., Carslaw, K. S., Dommen, J., Hansel, A., Petäjä, T., Sipilä, M., Stratmann, F., Vrtala, A., Wagner, P. E., Worsnop, D. R., Curtius, J.,

- and Kulmala, M.: Effect of ions on sulfuric acid-water binary particle formation: 2. Experimental data and comparison with QC-normalized classical nucleation theory, *Journal of Geophysical Research: Atmospheres*, 121, 1752–1775, <https://doi.org/10.1002/2015JD023539>, 2016.
- Ehn, M., Thornton, J. A., Kleist, E., Sipilä, M., Junninen, H., Pullinen, I., Springer, M., Rubach, F., Tillmann, R., Lee, B., Lopez-Hilfiker, F., Andres, S., Acir, I.-H., Rissanen, M., Jokinen, T., Schobesberger, S., Kangasluoma, J., Kontkanen, J., Nieminen, T., Kurtén, T., Nielsen, L. B., Jørgensen, S., Kjaergaard, H. G., Canagaratna, M., Maso, M. D., Berndt, T., Petäjä, T., Wahner, A., Kerminen, V.-M., Kulmala, M., Worsnop, D. R., Wildt, J., and Mentel, T. F.: A large source of low-volatility secondary organic aerosol, *Nature*, 506, 476–479, <https://doi.org/10.1038/nature13032>, 2014.
- Eiguren-Fernandez, A., Lewis, G. S., Spielman, S. R., and Hering, S. V.: Time-resolved characterization of particle associated polycyclic aromatic hydrocarbons using a newly-developed sequential spot sampler with automated extraction and analysis, *Atmospheric Environment*, 96, 125–134, <https://doi.org/10.1016/j.atmosenv.2014.07.031>, 2014.
- Elm, J.: Elucidating the Limiting Steps in Sulfuric Acid-Base New Particle Formation, *Journal of Physical Chemistry A*, 121, 8288–8295, <https://doi.org/10.1021/acs.jpca.7b08962>, 2017a.
- Elm, J.: Elucidating the Limiting Steps in Sulfuric Acid-Base New Particle Formation, *J. Phys. Chem. A*, 121, 8288–8295, <https://doi.org/10.1021/acs.jpca.7b08962>, 2017b.
- Elm, J.: An Atmospheric Cluster Database Consisting of Sulfuric Acid, Bases, Organics, and Water, *ACS Omega*, 4, 10965–10974, <https://doi.org/10.1021/acsomega.9b00860>, 2019.
- Elm, J., Jen, C. N., Kurtén, T., and Vehkamäki, H.: Strong Hydrogen Bonded Molecular Interactions between Atmospheric Diamines and Sulfuric Acid, *J. Phys. Chem. A*, 120, 3693–3700, <https://doi.org/10.1021/acs.jpca.6b03192>, 2016.
- Elm, J., Passananti, M., Kurtén, T., and Vehkamäki, H.: Diamines Can Initiate New Particle Formation in the Atmosphere, *Journal of Physical Chemistry A*, 121, 6155–6164, <https://doi.org/10.1021/acs.jpca.7b05658>, 2017.
- Elm, J., Kubečka, J., Besel, V., Jääskeläinen, M. J., Halonen, R., Kurten, T., and Vehkamäki, H.: Modeling the formation and growth of atmospheric molecular clusters : A review, *Journal of Aerosol Science*, 149, <https://doi.org/10.1016/j.jaerosci.2020.105621>, 2020.
- Erupe, M. E., Viggiano, A. A., and Lee, S. H.: The effect of trimethylamine on atmospheric nucleation involving H₂SO₄, *Atmospheric Chemistry and Physics*, 11, 4767–4775, <https://doi.org/10.5194/acp-11-4767-2011>, 2011.
- Facchini, M. C., Decesari, S., Rinaldi, M., Carbone, C., Finessi, E., Mircea, M., Fuzzi, S., Moretti, F., Tagliavini, E., Ceburnis, D., and O’Dowd, C. D.: Important source of marine secondary organic aerosol from biogenic amines, *Environmental Science and Technology*, 42, 9116–9121, <https://doi.org/10.1021/es8018385>, 2008.
- Farrokhpour, H. and Manassir, M.: Approach for predicting the standard free energy solvation of H⁺ and acidity constant in nonaqueous organic solvents, *Journal of Chemical and Engineering Data*, 59, 3555–3564, <https://doi.org/10.1021/je500459x>, 2014.

- Finlayson-Pitts, B. J. and Pitts, J. N.: Chemistry of the Upper and Lower Atmosphere, Academic Press, 2000.
- Freshour, N. A., Carlson, K. K., Melka, Y. A., Hinz, S., Panta, B., and Hanson, D. R.: Amine permeation sources characterized with acid neutralization and sensitivities of an amine mass spectrometer, *Atmospheric Measurement Techniques*, 7, 3611–3621, <https://doi.org/10.5194/amt-7-3611-2014>, 2014.
- Frisch, M. J., Trucks, G. W., Schlegel, H. B., Scuseria, G. E., Robb, M. A., Cheeseman, J. R., Scalmani, G., Barone, V., Petersson, G. A., Nakatsuji, H., Li, X., Caricato, M., Marenich, A. V., Bloino, J., Janesko, B. G., Gomperts, R., Mennucci, B., Hratchian, H. P., Ortiz, J. V., Izmaylov, A. F., Sonnenberg, J. L., Williams-Young, D., Ding, F., Lipparini, F., Egidi, F., Goings, J., Peng, B., Petrone, A., Henderson, T., Ranasinghe, D., Zakrzewski, V. G., Gao, J., Rega, N., Zheng, G., Liang, W., Hada, M., Ehara, M., Toyota, K., Fukuda, R., Hasegawa, J., Ishida, M., Nakajima, T., Honda, Y., Kitao, O., Nakai, H., Vreven, T., Throssell, K., Montgomery, J. A., J., Peralta, J. E., Ogliaro, F., Bearpark, M. J., Heyd, J. J., Brothers, E. N., Kudin, K. N., Staroverov, V. N., Keith, T. A., Kobayashi, R., Normand, J., Raghavachari, K., Rendell, A. P., Burant, J. C., Iyengar, S. S., Tomasi, J., Cossi, M., Millam, J. M., Klene, M., Adamo, C., Cammi, R., Ochterski, J. W., Martin, R. L., Morokuma, K., Farkas, O., Foresman, J. B., and Fox, D. J.: Gaussian16 Revision A.03, 2016.
- Ge, X., Wexler, A. S., and Clegg, S. L.: Atmospheric amines Part I. A review, *Atmospheric Environment*, 45, 524–546, <https://doi.org/10.1016/j.atmosenv.2010.10.012>, 2011.
- Glasoe, W. A., Volz, K., Panta, B., Freshour, N., Bachman, R., Hanson, D. R., McMurry, P. H., and Jen, C.: Sulfuric acid nucleation: An experimental study of the effect of seven bases, *Journal of Geophysical Research: Atmospheres*, 120, 1933–1950, <https://doi.org/10.1002/2014JD022730>, 2015.
- Hamed, A., Korhonen, H., Sihto, S. L., Joutsensaari, J., Jrvinen, H., Petäjä, T., Arnold, F., Nieminen, T., Kulmala, M., Smith, J. N., Lehtinen, K. E., and Laaksonen, A.: The role of relative humidity in continental new particle formation, *Journal of Geophysical Research Atmospheres*, 116, <https://doi.org/10.1029/2010JD014186>, 2011.
- Han, J., Wang, L., Zhang, H., Su, Q., Zhou, X., and Liu, S.: Determinant Factor for Thermodynamic Stability of Sulfuric Acid–Amine Complexes, *The Journal of Physical Chemistry A*, 124, 10 246–10 257, <https://doi.org/10.1021/acs.jpca.0c07908>, 2020.
- Hartono, A., Saeed, M., Kim, I., and Svendsen, H. F.: Protonation constant (pKa) of MDEA in water as function of temperature and ionic strength, *Energy Procedia*, 63, 1122–1128, <https://doi.org/10.1016/j.egypro.2014.11.121>, 2014.
- Haynes, W. M.: CRC handbook of chemistry and physics, CRC press, 2014.
- Hemmilä, M., Hellén, H., Virkkula, A., Makkonen, U., Praplan, A. P., Kontkanen, J., Ahonen, L., Kulmala, M., and Hakola, H.: Amines in boreal forest air at SMEAR II station in Finland, *Atmospheric Chemistry and Physics*, 18, 6367–6380, <https://doi.org/10.5194/acp-18-6367-2018>, 2018.

- Henschel, H., Navarro, J. C. A., Yli-Juuti, T., Kupiainen-Määttä, O., Olenius, T., Ortega, I. K., Clegg, S. L., Kurtén, T., Riipinen, I., and Vehkamäki, H.: Hydration of Atmospherically Relevant Molecular Clusters: Computational Chemistry and Classical Thermodynamics, *The Journal of Physical Chemistry A*, 118, 2599–2611, <https://doi.org/10.1021/jp500712y>, 2014.
- Herrmann, E., Brus, D., Hyvärinen, A. P., Stratmann, F., Wilck, M., Lihavainen, H., and Kulmala, M.: A computational fluid dynamics approach to nucleation in the water-sulfuric acid system, *Journal of Physical Chemistry A*, 114, 8033–8042, <https://doi.org/10.1021/jp103499q>, 2010.
- Holmes, B. J. and Petrucci, G. A.: Water-soluble oligomer formation from acid-catalyzed reactions of levoglucosan in proxies of atmospheric aqueous aerosols, *Environmental Science and Technology*, 40, 4983–4989, <https://doi.org/10.1021/es060646c>, 2006.
- Huang, G., Zhou, X., Deng, G., Qiao, H., and Civerolo, K.: Measurements of atmospheric nitrous acid and nitric acid, Tech. rep., URL https://ac.els-cdn.com/S135223100200170X/1-s2.0-S135223100200170X-main.pdf?_tid=304d59cd-b40b-4fce-a951-429d3d6e2300&acdnat=1542235641_7acc81148c138e29a8171f2d7b5654ea, 2002.
- Hunter, E. P. L. and Lias, S. G.: Evaluated Gas Phase Basicities and Proton Affinities of Molecules; Heats of Formation of Protonated Molecules, *Journal of Physical and Chemical Reference Data*, 27, 413–656, <https://doi.org/10.1063/1.555719>, 1998.
- IPCC: Climate Change 2014: Synthesis Report. Contribution of Working Groups I, II and III to the Fifth Assessment Report of the Intergovernmental Panel on Climate Change [Core Writing Team, R.K. Pachauri and L.A. Meyer (eds.)], Tech. rep., IPCC, Geneva, Switzerland, 2014.
- Jang, M., Czoschke, N. M., Lee, S., and Kamens, R. M.: Heterogeneous atmospheric aerosol production by acid-catalyzed particle-phase reactions, *Science*, 298, 814–817, <https://doi.org/10.1126/science.1075798>, 2002.
- Jen, C. N., McMurry, P. H., and Hanson, D. R.: Stabilization of sulfuric acid dimers by ammonia, methylamine, dimethylamine, and trimethylamine, *Journal of Geophysical Research: Atmospheres*, 119, 7502–7514, <https://doi.org/10.1002/2014JD021592>, 2014a.
- Jen, C. N., McMurry, P. H., and Hanson, D. R.: Stabilization of Sulfuric Acid Dimers by Ammonia, Methylamine, Dimethylamine, and Trimethylamine, *J. Geophys. Res. Atmos.*, 119, 7502–7514, <https://doi.org/10.1002/2014JD021592>, 2014b.
- Jew, K., Herr, D., Wong, C., Kennell, A., Morris-schaffer, K., Oberdörster, G., Banion, M. K. O., Cory-slechta, D. A., and Elder, A.: Selective memory and behavioral alterations after ambient ultrafine particulate matter exposure in aged 3xTgAD Alzheimer’s disease mice, *Particle and Fibre Toxicology*, 16, 2019.
- Junninen, H., Ehn, M., Petäjä, Luosujärvi, L., Kotiaho, T., Kostianen, R., Rohner, U., Gonnin, M., Fuhrer, K., Kulmala, M., and Worsnop, D. R.: A high-resolution mass spectrometer to measure atmospheric ion composition, *Atmospheric Measurement Techniques*, 3, 1039–1053, <https://doi.org/10.5194/amt-3-1039-2010>, 2010.
- Kerminen, V.-M., Lihavainen, H., Komppula, M., Viisanen, Y., and Kulmala, M.: Direct observational evidence linking atmospheric aerosol formation and cloud droplet activation, *Geophysical Research Letters*, 32, <https://doi.org/10.1029/2005GL023130>, 2005.

- Kerminen, V. M., Chen, X., Vakkari, V., Petäjä, T., Kulmala, M., and Bianchi, F.: Atmospheric new particle formation and growth: Review of field observations, *Environmental Research Letters*, 13, 103 003, <https://doi.org/10.1088/1748-9326/aadf3c>, 2018.
- Keskinen, H., Virtanen, A., Joutsensaari, J., Tsagkogeorgas, G., Duplissy, J., Schobesberger, S., Gysel, M., Riccobono, F., Slowik, J. G., Bianchi, F., Yli-Juuti, T., Lehtipalo, K., Rondo, L., Breitenlechner, M., Kupc, A., Almeida, J., Amorim, A., Dunne, E. M., Downard, A. J., Ehrhart, S., Franchin, A., Kajos, M., Kirkby, J., Kürten, A., Nieminen, T., Makhmutov, V., Mathot, S., Miettinen, P., Onnela, A., Petäjä, T., Praplan, A., Santos, F. D., Schallhart, S., Sipilä, M., Stozhkov, Y., Tomé, A., Vaattovaara, P., Wimmer, D., Prevot, A., Dommen, J., Donahue, N. M., Flagan, R., Weingartner, E., Viisanen, Y., Riipinen, I., Hansel, A., Curtius, J., Kulmala, M., Worsnop, D. R., Baltensperger, U., Wex, H., Stratmann, F., and Laaksonen, A.: Evolution of particle composition in CLOUD nucleation experiments, *Atmospheric Chemistry and Physics*, 13, 5587–5600, <https://doi.org/10.5194/acp-13-5587-2013>, 2013.
- Kim, J., Ahlm, L., Yli-Juuti, T., Lawler, M., Keskinen, H., Tröstl, J., Schobesberger, S., Duplissy, J., Amorim, A., Bianchi, F., Donahue, N. M., Flagan, R. C., Hakala, J., Heinritzi, M., Jokinen, T., Kürten, A., Laaksonen, A., Lehtipalo, K., Miettinen, P., Petäjä, T., Rissanen, M. P., Rondo, L., Sengupta, K., Simon, M., Tomé, A., Williamson, C., Wimmer, D., Winkler, P. M., Ehrhart, S., Ye, P., Kirkby, J., Curtius, J., Baltensperger, U., Kulmala, M., Lehtinen, K. E. J., Smith, J. N., Riipinen, I., and Virtanen, A.: Hygroscopicity of nanoparticles produced from homogeneous nucleation in the CLOUD experiments, *Atmospheric Chemistry and Physics*, 16, 293–304, <https://doi.org/10.5194/acp-16-293-2016>, 2016.
- Kirkby, J., Curtius, J., Almeida, J., Dunne, E., Duplissy, J., Ehrhart, S., Franchin, A., Gagné, S., Ickes, L., Kürten, A., Kupc, A., Metzger, A., Riccobono, F., Rondo, L., Schobesberger, S., Tsagkogeorgas, G., Wimmer, D., Amorim, A., Bianchi, F., Breitenlechner, M., David, A., Dommen, J., Downard, A., Ehn, M., Flagan, R. C., Haider, S., Hansel, A., Hauser, D., Jud, W., Junninen, H., Kreissl, F., Kvashin, A., Laaksonen, A., Lehtipalo, K., Lima, J., Lovejoy, E. R., Makhmutov, V., Mathot, S., Mikkilä, J., Minginette, P., Mogo, S., Nieminen, T., Onnela, A., Pereira, P., Petäjä, T., Schnitzhofer, R., Seinfeld, J. H., Sipilä, M., Stozhkov, Y., Stratmann, F., Tomé, A., Vanhanen, J., Viisanen, Y., Vrtala, A., Wagner, P. E., Walther, H., Weingartner, E., Wex, H., Winkler, P. M., Carslaw, K. S., Worsnop, D. R., Baltensperger, U., and Kulmala, M.: Role of sulphuric acid, ammonia and galactic cosmic rays in atmospheric aerosol nucleation, *Nature*, 476, 429–433, <https://doi.org/10.1038/nature10343>, 2011.
- Kiyoura, R. and Urano, K.: Mechanism, Kinetics, and Equilibrium of Thermal Decomposition of Ammonium Sulfate, *Industrial and Engineering Chemistry Process Design and Development*, 9, 489–494, <https://doi.org/10.1021/i260036a001>, 1970.
- Korhonen, P., Kulmala, M., Laaksonen, A., Viisanen, Y., McGraw, R., and Seinfeld, J. H.: Ternary nucleation of H₂SO₄, NH₃, and H₂O in the atmosphere, *Journal of Geophysical Research*, 104, 26 349–26 353, 1999.
- Kreidenweis, S. M., Flagan, R. C., Seinfeld, J. H., and Okuyama, K.: Binary nucleation of methanesulfonic acid and water, *Journal of Aerosol Science*, 20, 585–607, [https://doi.org/10.1016/0021-8502\(89\)90105-5](https://doi.org/10.1016/0021-8502(89)90105-5), 1989.

- Kreinbühl, J. J., Frederiks, N. C., Waller, S. E., Yang, Y., and Johnson, C. J.: Establishing the structural motifs present in small ammonium and aminium bisulfate clusters of relevance to atmospheric new particle formation, *The Journal of Chemical Physics*, 153, 034307, <https://doi.org/10.1063/5.0015094>, 2020.
- Kuang, C., McMurry, P. H., McCormick, A. V., and Eisele, F. L.: Dependence of nucleation rates on sulfuric acid vapor concentration in diverse atmospheric locations, *Journal of Geophysical Research*, 113, D10209, <https://doi.org/10.1029/2007JD009253>, 2008.
- Kuang, C., McMurry, P. H., and McCormick, A. V.: Determination of cloud condensation nuclei production from measured new particle formation events, *Geophysical Research Letters*, 36, 1–5, <https://doi.org/10.1029/2009GL037584>, 2009.
- Kuang, C., Riipinen, I., Sihto, S.-L., Kulmala, M., McCormick, A. V., and McMurry, P. H.: An improved criterion for new particle formation in diverse atmospheric environments, *Atmospheric Chemistry and Physics*, 10, 8469–8480, <https://doi.org/10.5194/acp-10-8469-2010>, 2010.
- Kubečka, J., Besel, V., Kurtén, T., Myllys, N., and Vehkamäki, H.: Configurational Sampling of Noncovalent (Atmospheric) Molecular Clusters: Sulfuric Acid and Guanidine, *J. Phys. Chem. A*, 123, 6022–6033, <https://doi.org/10.1021/acs.jpca.9b03853>, 2019.
- Kulkarni, P., Baron, P. A., and Willeke, K., eds.: *Aerosol Measurement: Principles, Techniques, and Applications*, Wiley, <https://doi.org/10.1002/9781118001684>, 2011.
- Kulmala, M., Vehkamäki, H., Petäjä, T., Dal Maso, M., Lauri, A., Kerminen, V.-M., Birmili, W., and McMurry, P.: Formation and growth rates of ultrafine atmospheric particles: a review of observations, *Journal of Aerosol Science*, 35, 143–176, <https://doi.org/10.1016/j.jaerosci.2003.10.003>, 2004.
- Kulmala, M., Lehtinen, K. E., and Laaksonen, A.: Cluster activation theory as an explanation of the linear dependence between formation rate of 3 nm particles and sulphuric acid concentration, *Atmospheric Chemistry and Physics*, 6, 787–793, <https://doi.org/10.5194/acp-6-787-2006>, 2006.
- Kulmala, M., Kerminen, V. M., Petäjä, T., Ding, A. J., and Wang, L.: Atmospheric gas-to-particle conversion: Why NPF events are observed in megacities?, *Faraday Discussions*, 200, 271–288, <https://doi.org/10.1039/c6fd00257a>, 2017.
- Kupiainen, O., Ortega, I. K., Kurtén, T., and Vehkamäki, H.: Amine Substitution into Sulfuric Acid–Ammonia Clusters, *Atmos. Chem. Phys.*, 12, 3591–3599, 2012.
- Kurt, T., Loukonen, V., and Vehkamäki, H.: Amines are likely to enhance neutral and ion-induced sulfuric acid-water nucleation in the atmosphere more effectively than ammonia, pp. 4095–4103, 2008.
- Kürten, A., Jokinen, T., Simon, M., Sipilä, M., Sarnela, N., Junninen, H., Adamov, A., Almeida, J., Amorim, A., Bianchi, F., Breitenlechner, M., Dommen, J., Donahue, N. M., Duplissy, J., Ehrhart, S., Flagan, R. C., Franchin, A., Hakala, J., Hansel, A., Heinritzi, M., Hutterli, M., Kangasluoma, J., Kirkby, J., Laaksonen, A., Lehtipalo, K., Leiminger, M., Makhmutov, V., Mathot, S., Onnela, A., Petäjä, T., Praplan, A. P., Riccobono, F., Rissanen, M. P., Rondo, L., Schobesberger, S., Seinfeld, J. H., Steiner, G., Tomé, A., Tröstl, J., Winkler, P. M., Williamson, C., Wimmer, D., Ye, P., Baltensperger, U., Carslaw, K. S., Kulmala, M., Worsnop, D. R., and Curtius, J.:

- Neutral molecular cluster formation of sulfuric acid–Dimethylamine observed in real time under atmospheric conditions, *Proceedings of the National Academy of Sciences*, 111, 15 019–15 024, <https://doi.org/10.1073/pnas.1404853111>, 2014.
- Kürten, A., Bergen, A., Heinritzi, M., Leiminger, M., Lorenz, V., Piel, F., Simon, M., Sitals, R., Wagner, A. C., and Curtius, J.: Observation of new particle formation and measurement of sulfuric acid, ammonia, amines and highly oxidized organic molecules at a rural site in central Germany, *Atmospheric Chemistry and Physics*, 16, 12 793–12 813, <https://doi.org/10.5194/acp-16-12793-2016>, 2016.
- Kurtén, T., Loukonen, V., Vehkamäki, H., and Kulmala, M.: Amines are likely to enhance neutral and ion-induced sulfuric acid-water nucleation in the atmosphere more effectively than ammonia, *Atmospheric Chemistry and Physics*, 8, 4095–4103, <https://doi.org/10.5194/acp-8-4095-2008>, 2008.
- Kurtén, T., Loukonen, V., Vehkamäki, H., and Kulmala, M.: Amines Are Likely to Enhance Neutral and Ion-Induced Sulfuric Acid-Water Nucleation in the Atmosphere More Effectively Than Ammonia, *Atmos. Chem. Phys.*, 8, 4095–4103, <https://doi.org/10.5194/acp-8-4095-2008>, 2008.
- Laaksonen, A., Kulmala, M., Berndt, T., Stratmann, F., Mikkonen, S., Ruuskanen, A., Lehtinen, K. E., Dal Maso, M., Aalto, P., Petäjä, T., Riipinen, I., Sihto, S. L., Janson, R., Arnold, F., Hanke, M., Ücker, J., Umann, B., Sellegri, K., O’Dowd, C. D., and Viisanen, Y.: SO₂ oxidation products other than H₂SO₄ as a trigger of new particle formation. Part 2: Comparison of ambient and laboratory measurements, and atmospheric implications, *Atmospheric Chemistry and Physics*, 8, 7255–7264, <https://doi.org/10.5194/acp-8-7255-2008>, 2008.
- Lavi, A., Segre, E., Gomez-Hernandez, M., Zhang, R., and Rudich, Y.: Volatility of Atmospherically Relevant Alkylammonium Carboxylate Salts, *The Journal of Physical Chemistry A*, 119, 4336–4346, <https://doi.org/10.1021/jp507320v>, 2015.
- Lawler, M. J., Whitehead, J., O’Dowd, C., Monahan, C., Mcfiggans, G., and Smith, J. N.: Composition of 15–85 nm particles in marine air, *Atmos. Chem. Phys.*, 14, 11 557–11 569, <https://doi.org/10.5194/acp-14-11557-2014>, 2014.
- Lawler, M. J., Winkler, P. M., Kim, J., Ahlm, L., Tröstl, J., Praplan, A. P., Schobesberger, S., Kürten, A., Kirkby, J., Bianchi, F., Duplissy, J., Hansel, A., Jokinen, T., Keskinen, H., Lehtipalo, K., Leiminger, M., Petäjä, T., Rissanen, M., Rondo, L., Simon, M., Sipilä, M., Williamson, C., Wimmer, D., Riipinen, I., Virtanen, A., and Smith, J. N.: Unexpectedly acidic nanoparticles formed in dimethylamine-ammonia-sulfuric-acid nucleation experiments at CLOUD, *Atmospheric Chemistry and Physics*, 16, 13 601–13 618, <https://doi.org/10.5194/acp-16-13601-2016>, 2016.
- Lee, S. H., Gordon, H., Li, Y., Zhang, R., and Lehtipalo, K.: New Particle Formation in the Atmosphere : From Molecular Clusters to Global Climate *Journal of Geophysical Research : Atmospheres*, <https://doi.org/10.1029/2018JD029356>, 2019.
- Lehtipalo, K., Rondo, L., Kontkanen, J., Schobesberger, S., Jokinen, T., Sarnela, N., Kürten, A., Ehrhart, S., Franchin, A., Nieminen, T., et al.: The Effect of Acid–Base Clustering and Ions on the Growth of Atmospheric Nano-Particles, *Nature Comm.*, 7, 11 594, 2016.

- Leverentz, H. R., Siepmann, J. I., Truhlar, D. G., Loukonen, V., and Vehkamäki, H.: Energetics of Atmospherically Implicated Clusters Made of Sulfuric Acid, Ammonia, and Dimethyl Amine, *J. Phys. Chem. A*, 117, 3819–3825, <https://doi.org/10.1021/jp402346u>, 2013.
- Li, X., Chee, S., Hao, J., Abbatt, J. P. D., Jiang, J., and Smith, J. N.: Relative humidity effect on the formation of highly oxidized molecules and new particles during monoterpene oxidation, *Atmos. Chem. Phys.*, 19, 1555–1570, <https://doi.org/acp-19-1555-2019>, 2019.
- Lightstone, J. M., Onasch, T. B., Imre, D., York, N., and Oatis, S.: Deliquescence, Efflorescence, and Water Activity in Ammonium Nitrate and Mixed Ammonium Nitrate/Succinic Acid Microparticles, *The Journal of Physical Chemistry A*, 104, 9337–9346, <https://doi.org/10.1021/jp002137h>, 2000.
- Liu, P. S. K. and Deshler, T.: Causes of Concentration Differences Between a Scanning Mobility Particle Sizer and a Condensation Particle Counter, *Aerosol Science and Technology*, 37, 916–923, <https://doi.org/10.1080/027868203000931>, 2010.
- Liu, Y., Han, C., Liu, C., Ma, J., Ma, Q., and He, H.: Differences in the reactivity of ammonium salts with methylamine, *Atmospheric Chemistry and Physics*, 12, 4855–4865, <https://doi.org/10.5194/acp-12-4855-2012>, 2012.
- Lohmann, U. and Feichter, J.: Global indirect aerosol effects: a review, *Atmospheric Chemistry and Physics Discussions*, 4, 7561–7614, <https://doi.org/10.5194/acpd-4-7561-2004>, 2004.
- Loukonen, V., Kurtén, T., Ortega, I. K., Vehkamäki, H., adua, A. A., Sellegri, K., and Kulmala, M.: Enhancing effect of dimethylamine in sulfuric acid nucleation in the presence of water—a computational study, *Atmospheric Chemistry and Physics*, 10, 4961–4974, <https://doi.org/10.5194/acp-10-4961-2010>, 2010.
- Ma, F., Xie, H.-B., Elm, J., Shen, J., Chen, J., and Vehkamäki, H.: Piperazine enhancing sulfuric acid-based new particle formation: implications for the atmospheric fate of piperazine, *Environmental science & technology*, 53, 8785–8795, 2019.
- MacMillan, A. C., Morrison, J. B., Harmon, C. W., and Nizkorodov, S. A.: Enhancement of Surfactants in Nanoparticles Produced by an Electrospray Aerosol Generator, 6826, <https://doi.org/10.1080/02786826.2012.708946>, 2012.
- Mäkelä, J. M., Ylikoivisto, S., Hiltunen, V., Seidl, W., Swietlicki, E., Teinilä, K., Sillanpää, M., Koponen, I. K., Paatero, J., Rosman, K., and Hämeri, K.: Chemical composition of aerosol during particle formation events in boreal forest, *Tellus, Series B: Chemical and Physical Meteorology*, 53, 380–393, <https://doi.org/10.3402/tellusb.v53i4.16610>, 2001.
- Matthews, J., Sumner, J. F., and Moelwyn-Hughes, E.: The Vapour Pressures of Certain Liquids, *Transactions of the Faraday Society*, 46, 797–803, 1950.
- Mcgrath, M. J., Olenius, T., Ortega, I. K., Loukonen, V., Paasonen, P., and Kurtén, T.: Atmospheric Cluster Dynamics Code: a flexible method for solution of the birth-death equations, *Atmospheric Chemistry and Physics*, 12, 2345–2355, <https://doi.org/10.5194/acp-12-2345-2012>, 2012.

- McGrath, M. J., Olenius, T., Ortega, I. K., Loukonen, V., Paasonen, P., Kurtén, T., Kulmala, M., and Vehkamäki, H.: Atmospheric Cluster Dynamics Code: a Flexible Method for Solution of the Birth–Death Equations, *Atmos. Chem. Phys.*, 12, 2345–2355, <https://doi.org/10.5194/acp-12-2345-2012>, 2012.
- McMurry, P. H., Woo, K. S., Weber, R., Chen, D. R., and Pui, D. Y.: Size distributions of 3–10 nm atmospheric particles: Implications for nucleation mechanisms, *Philosophical Transactions of the Royal Society A: Mathematical, Physical and Engineering Sciences*, 358, 2625–2642, <https://doi.org/10.1098/rsta.2000.0673>, 2000.
- McMurry, P. H., Ghimire, A., Ahn, H.-K., Sakurai, H., Moore, K., Stolzenburg, M. R., and Smith, J. N.: Sampling Nanoparticles for Chemical Analysis by Low Resolution Electrical Mobility Classification, *Environmental Science & Technology*, 43, 4653–4658, <https://doi.org/10.1016/j.jbi.2012.04.006>, 2009.
- Merikanto, J., Spracklen, D. V., Mann, G. W., Pickering, S. J., and Carslaw, K. S.: Impact of nucleation on global CCN, *Atmospheric Chemistry and Physics*, 9, 8601–8616, <https://doi.org/10.5194/acp-9-8601-2009>, 2009.
- Murphy, S. M., Sorooshian, A., Kroll, J. H., Ng, N. L., Chhabra, P., Tong, C., Surratt, J. D., and Knipping, E.: Secondary aerosol formation from atmospheric reactions of aliphatic amines, *Atmospheric Chemistry and Physics*, 7, 2313–2337, 2007.
- Myllys, N., Elm, J., Halonen, R., Kurtén, T., and Vehkamäki, H.: Coupled Cluster Evaluation of the Stability of Atmospheric AcidBase Clusters with up to 10 Molecules, *The Journal of Physical Chemistry A*, 120, 621–630, <https://doi.org/10.1021/acs.jpca.5b09762>, 2016a.
- Myllys, N., Elm, J., and Kurtén, T.: Density functional theory basis set convergence of sulfuric acid-containing molecular clusters, *Computational and Theoretical Chemistry*, 1098, 1–12, <https://doi.org/10.1016/j.comptc.2016.10.015>, 2016b.
- Myllys, N., Ponkkonen, T., Passananti, M., Elm, J., Vehkamäki, H., and Olenius, T.: Guanidine: A Highly Efficient Stabilizer in Atmospheric New-Particle Formation, *Journal of Physical Chemistry A*, 122, 4717–4729, <https://doi.org/10.1021/acs.jpca.8b02507>, 2018a.
- Myllys, N., Ponkkonen, T., Passananti, M., Elm, J., Vehkamäki, H., and Olenius, T.: Guanidine: A Highly Efficient Stabilizer in Atmospheric New-Particle Formation, *J. Phys. Chem. A*, 122, 4717–4729, <https://doi.org/10.1021/acs.jpca.8b02507>, 2018b.
- Myllys, N., Chee, S., Olenius, T., Lawler, M., and Smith, J.: Molecular-Level Understanding of Synergistic Effects in Sulfuric Acid Amine Ammonia Mixed Clusters, *The Journal of Physical Chemistry A*, 123, 2420–2425, <https://doi.org/10.1021/acs.jpca.9b00909>, 2019a.
- Myllys, N., Kubecka, J., Besel, V., Alfaouri, D., Olenius, T., Smith, J. N., and Passananti, M.: Role of base strength, cluster structure and charge in sulfuric-acid-driven particle formation, *Atmos. Chem. Phys.*, pp. 9753–9768, 2019b.
- Myllys, N., Kubečka, J., Besel, V., Alfaouri, D., Olenius, T., Smith, J. N., and Passananti, M.: Role of Base Strength, Cluster Structure and Charge in Sulfuric-Acid-Driven Particle Formation, *Atmos. Chem. Phys.*, 19, 9753–9768, <https://doi.org/10.5194/acp-19-9753-2019>, 2019c.

- Myllys, N., Ponkkonen, T., Chee, S., and Smith, J.: Enhancing Potential of Trimethylamine Oxide on Atmospheric Particle Formation, *Atmosphere*, 11, 35, <https://doi.org/10.3390/atmos11010035>, 2020.
- Nadykto, A., Herb, J., Yu, F., Xu, Y., and Nazarenko, E.: Estimating the Lower Limit of the Impact of Amines on Nucleation in the Earth's Atmosphere, *Entropy*, 17, 2764–2780, <https://doi.org/10.3390/e17052764>, 2015.
- Nadykto, A. B. and Yu, F.: Strong Hydrogen Bonding between Atmospheric Nucleation Precursors and Common Organics, *Chem. Phys. Lett.*, 435, 14–18, <https://doi.org/http://dx.doi.org/10.1016/j.cplett.2006.12.050>, 2007.
- Nadykto, A. B., Yu, F., Jakovleva, M. V., Herb, J., and Xu, Y.: Amines in the Earth's Atmosphere: A Density Functional Theory Study of the Thermochemistry of Pre-Nucleation Clusters, *Entropy*, 13, 554–569, 2011.
- Nair, A. A. and Yu, F.: Quantification of Atmospheric Ammonia Concentrations: A Review of Its Measurement and Modeling, *Atmosphere*, 11, <https://doi.org/10.3390/atmos11101092>, 2020.
- Neese, F.: The ORCA program system, *WIREs Comput. Mol. Sci.*, 2, 73–78, <https://doi.org/10.1002/wcms.81>, 2012.
- Neitola, K., Brus, D., Makkonen, U., Sipilä, M., Mauldin, R. L., Sarnela, N., Jokinen, T., Lihavainen, H., and Kulmala, M.: Total sulfate vs. sulfuric acid monomer concentrations in nucleation studies, *Atmospheric Chemistry and Physics*, 15, 3429–3443, <https://doi.org/10.5194/acp-15-3429-2015>, 2015.
- Noble, C. A. and Prather, K. A.: Real-time measurement of correlated size and composition profiles of individual atmospheric aerosol particles, *Environmental Science and Technology*, 30, 2667–2680, <https://doi.org/10.1021/es950669j>, 1996.
- Oberdörster, G., Sharp, Z., Atudorei, V., Elder, A., Gelein, R., Kreyling, W., and Cox, C.: Translocation of Inhaled Ultrafine Particles to the Brain, *Inhalation Toxicology*, 16, 437–445, 2004.
- Oberdörster, G., Oberdörster, E., and Oberdörster, J.: Nanotoxicology: An Emerging Discipline Evolving from Studies of Ultrafine Particles, *Environmental Health Perspectives*, 113, 823–839, <https://doi.org/10.1289/ehp.7339>, 2005.
- Olenius, T. and Riipinen, I.: Molecular-resolution simulations of new particle formation: Evaluation of common assumptions made in describing nucleation in aerosol dynamics models, *Aerosol Science and Technology*, 51, 397–408, <https://doi.org/10.1080/02786826.2016.1262530>, 2017.
- Olenius, T., Kupiainen-Määttä, O., Ortega, I. K., Kurtén, T., and Vehkamäki, H.: Free Energy Barrier in the Growth of Sulfuric Acid–Ammonia and Sulfuric Acid–Dimethylamine Clusters, *J. Chem. Phys.*, 139, 084312, <https://doi.org/http://dx.doi.org/10.1063/1.4819024>, 2013.
- Olenius, T., Halonen, R., Kurtén, T., Henschel, H., Kupiainen-Määttä, O., Ortega, I. K., Jen, C. N., Vehkamäki, H., and Riipinen, I.: New Particle Formation from Sulfuric Acid and Amines: Comparison of Mono-, Di-, and Trimethylamines, *J. Geophys. Res. Atmos.*, 122, 7103–7118, <https://doi.org/10.1002/2017JD026501>, 2017.

- Pakkanen, T. A.: STUDY OF FORMATION OF COARSE PARTICLE NITRATE AEROSOL, Tech. Rep. 14, URL https://ac.els-cdn.com/1352231095004920/1-s2.0-1352231095004920-main.pdf?_tid=1817e0f4-fa76-46dc-8528-70e816bfa47f&acdnat=1542231332_c5c4cd79b1fecf916990c93153052441, 1996.
- Panta, B., Glasoe, W. A., Zollner, J. H., Carlson, K. K., and Hanson, D. R.: Computational fluid dynamics of a cylindrical nucleation flow reactor with detailed cluster thermodynamics, *Journal of Physical Chemistry A*, 116, 10 122–10 134, <https://doi.org/10.1021/jp302444y>, 2012.
- Perraud, V., Li, X., Jiang, J., Finlayson-Pitts, B. J., and Smith, J. N.: Size-Resolved Chemical Composition of Sub-20 nm Particles from Methanesulfonic Acid Reactions with Methylamine and Ammonia, *ACS Earth and Space Chemistry*, 4, 1182–1194, <https://doi.org/10.1021/acsearthspacechem.0c00120>, 2020.
- Petäjä, T., Sipila, M., Paasonen, P., Nieminen, T., Kurtén, T., Ortega, I. K., Stratmann, F., Vehkamäki, H., Berndt, T., and Kulmala, M.: Experimental Observation of Strongly Bound Dimers of Sulfuric Acid : Application to Nucleation in the Atmosphere, *Physical Review Letters*, 106, 1–4, <https://doi.org/10.1103/PhysRevLett.106.228302>, 2011.
- Pichelstorfer, L., Stolzenburg, D., Ortega, J., Karl, T., Kokkola, H., Laakso, A., Lehtinen, K. E. J., Smith, J. N., McMurry, P. H., and Winkler, P. M.: Resolving nanoparticle growth mechanisms from size- and time-dependent growth rate analysis, *Atmospheric Chemistry and Physics*, 18, 1307–1323, <https://doi.org/10.5194/acp-18-1307-2018>, 2018.
- Pierce, J. R. and Adams, P. J.: Uncertainty in global CCN concentrations from uncertain aerosol nucleation and primary emission rates, *Atmos. Chem. Phys*, 9, 1339–1356, 2009.
- Pratt, K. A., Hatch, L. E., and Prather, K. A.: Seasonal volatility dependence of ambient particle phase amines, *Environmental Science and Technology*, 43, 5276–5281, <https://doi.org/10.1021/es803189n>, 2009.
- Qiu, C. and Zhang, R.: Physiochemical Properties of Alkylammonium Sulfates: Hygroscopicity, Thermostability, and Density, *Environmental Science & Technology*, 46, 4474–4480, <https://doi.org/10.1021/es3004377>, 2012.
- Qiu, C. and Zhang, R.: Multiphase chemistry of atmospheric amines, *Physical Chemistry Chemical Physics*, 15, 5738, <https://doi.org/10.1039/c3cp43446j>, 2013.
- Qiu, C., Wang, L., Lal, V., Khalizov, A. F., and Zhang, R.: Heterogeneous reactions of alkylamines with ammonium sulfate and ammonium bisulfate, *Environmental Science and Technology*, 45, 4748–4755, <https://doi.org/10.1021/es1043112>, 2011.
- Reijenga, J., van Hoof, A., van Loon, A., and Teunissen, B.: Development of methods for the determination of pKa values, *Analytical Chemistry Insights*, 8, 53–71, <https://doi.org/10.4137/ACI.S12304>, 2013.
- Riccobono, F., Schobesberger, S., Scott, C. E., Dommen, J., Ortega, I. K., Rondo, L., Almeida, J., Amorim, A., Bianchi, F., Breitenlechner, M., David, A., Downard, A., Dunne, E. M., Duplissy, J., Ehrhart, S., Flagan, R. C., Franchin, A., Hansel, A., Junninen, H., Kajos, M., Keskinen, H., Kupc, A., Kurten, A., Kvashin, A. N., Laaksonen, A., Lehtipalo, K., Makhmutov, V., Mathot, S., Nieminen, T., Onnela, A., Petaja, T., Praplan, A. P., Santos, F. D., Schallhart, S., Seinfeld,

- J. H., Sipila, M., Spracklen, D. V., Stozhkov, Y., Stratmann, F., Tome, A., Tsagkogeorgas, G., Vaattovaara, P., Viisanen, Y., Vrtala, A., Wagner, P. E., Weingartner, E., Wex, H., Wimmer, D., Carslaw, K. S., Curtius, J., Donahue, N. M., Kirkby, J., Kulmala, M., Worsnop, D. R., and Baltensperger, U.: Oxidation Products of Biogenic Emissions Contribute to Nucleation of Atmospheric Particles, *Science*, 344, 717–721, <https://doi.org/10.1126/science.1243527>, 2014.
- Riplinger, C. and Neese, F.: An Efficient and Near Linear Scaling Pair Natural Orbital Based Local Coupled Cluster Method, *J. Chem. Phys.*, 138, 034106, <https://doi.org/http://dx.doi.org/10.1063/1.4773581>, 2013.
- Riplinger, C., Sandhoefer, B., Hansen, A., and Neese, F.: Natural Triple Excitations in Local Coupled Cluster Calculations with Pair Natural Orbitals, *J. Chem. Phys.*, 139, 134101, <https://doi.org/http://dx.doi.org/10.1063/1.4821834>, 2013.
- Riplinger, C., Pinski, P., Becker, U., and Valeev, E. F.: Sparse maps — A systematic infrastructure for reduced-scaling electronic structure methods. II. Linear scaling domain based pair natural orbital coupled cluster theory, *The Journal of Chemical Physics*, 144, <https://doi.org/10.1063/1.4939030>, 2016.
- Rovelli, G., Miles, E. H., Reid, P. J., and Clegg, L. S.: Hygroscopic properties of aminium sulfate aerosols, *Atmospheric Chemistry and Physics*, 17, 4369–4385, <https://doi.org/10.5194/acp-17-4369-2017>, 2017.
- Salo, K., Westerlund, J., Andersson, P. U., Nielsen, C., Anna, B. D., and Hallquist, M.: Thermal Characterization of Aminium Nitrate Nanoparticles, *The Journal of Physical Chemistry A*, 115, 11 671–11 677, <https://doi.org/10.1021/jp204957k>, 2011.
- Sareen, N., Waxman, E. M., Turpin, B. J., Volkamer, R., and Carlton, A. G.: Potential of Aerosol Liquid Water to Facilitate Organic Aerosol Formation: Assessing Knowledge Gaps about Precursors and Partitioning, *ENVIRONMENTAL SCIENCE & TECHNOLOGY*, 51, 3327–3335, <https://doi.org/10.1021/acs.est.6b04540>, 2017.
- Sauerwein, M., Clegg, S. L., and Chan, C. K.: Water Activities and Osmotic Coefficients of Aqueous Solutions of Five Alkylaminium Sulfates and Their Mixtures with H₂SO₄ at 25 °C, *Aerosol Science and Technology*, 49, 566–579, <https://doi.org/10.1080/02786826.2015.1043045>, 2015.
- Sauerwein, M., Keung Chan, C., and to, C.: Heterogeneous uptake of ammonia and dimethylamine into sulfuric and oxalic acid particles, *Atmos. Chem. Phys*, 17, 6323–6339, <https://doi.org/10.5194/acp-17-6323-2017>, 2017.
- Schaftenaar, G. and Noordik, J. H.: Molden: a pre-and post-processing program for molecular and electronic structures, *Journal of computer-aided molecular design*, 14, 123–134, 2000.
- Schobesberger, S., Junninen, H., Bianchi, F., Lonn, G., Ehn, M., Lehtipalo, K., Dommen, J., Ehrhart, S., Ortega, I. K., Franchin, A., Nieminen, T., Riccobono, F., Hutterli, M., Duplissy, J., Almeida, J., Amorim, A., Breitenlechner, M., Downard, A. J., Dunne, E. M., Flagan, R. C., Kajos, M., Keskinen, H., Kirkby, J., Kupc, A., Kurten, A., Kurten, T., Laaksonen, A., Mathot, S., Onnela, A., Praplan, A. P., Rondo, L., Santos, F. D., Schallhart, S., Schnitzhofer, R., Sipila, M., Tome, A., Tsagkogeorgas, G., Vehkamäki, H., Wimmer, D., Baltensperger, U., Carslaw, K. S.,

- Curtius, J., Hansel, A., Petaja, T., Kulmala, M., Donahue, N. M., and Worsnop, D. R.: Molecular understanding of atmospheric particle formation from sulfuric acid and large oxidized organic molecules, *Proceedings of the National Academy of Sciences*, 110, 17 223–17 228, <https://doi.org/10.1073/pnas.1306973110>, 2013.
- Schobesberger, S., Franchin, A., Bianchi, F., Rondo, L., Duplissy, J., Kürten, A., Ortega, I. K., and Metzger, A.: On the composition of ammonia – sulfuric-acid ion clusters during aerosol particle formation, *Atmos. Chem. Phys*, 15, 55–78, <https://doi.org/10.5194/acp-15-55-2015>, 2015a.
- Schobesberger, S., Franchin, A., Bianchi, F., Rondo, L., Duplissy, J., Kürten, A., Ortega, I. K., Metzger, A., Schnitzhofer, R., Almeida, J., Amorim, A., Dommen, J., Dunne, E. M., Ehn, M., Gagné, S., Ickes, L., Junninen, H., Hansel, A., Kerminen, V.-M., Kirkby, J., Kupc, A., Laaksonen, A., Lehtipalo, K., Mathot, S., Onnela, A., Petäjä, T., Riccobono, F., Santos, F. D., Sipilä, M., Tomé, A., Tsagkogeorgas, G., Viisanen, Y., Wagner, P. E., Wimmer, D., Curtius, J., Donahue, N. M., Baltensperger, U., Kulmala, M., and Worsnop, D. R.: On the composition of ammonia–sulfuric-acid ion clusters during aerosol particle formation, *Atmospheric Chemistry and Physics*, 15, 55–78, <https://doi.org/10.5194/acp-15-55-2015>, 2015b.
- Seinfeld, J. H. and Pandis, S. N.: *Atmospheric Chemistry and Physics: From Air Pollution to Climate Change.*, John Wiley & Sons, Inc., New York, 2006.
- Seybold, P. G. and Shields, G. C.: Computational estimation of pKa values, *WIREs Computational Molecular Science*, 5, 290–297, <https://doi.org/https://doi.org/10.1002/wcms.1218>, 2015.
- Shen, J., Elm, J., Xie, H. B., Chen, J., Niu, J., and Vehkamäki, H.: Structural Effects of Amines in Enhancing Methanesulfonic Acid-Driven New Particle Formation, *Environmental Science and Technology*, 54, 13 498–13 508, <https://doi.org/10.1021/acs.est.0c05358>, 2020.
- Sihto, S. L., Kulmala, M., Kerminen, V. M., Dal Maso, M., Petäjä, T., Riipinen, I., Korhonen, H., Arnold, F., Janson, R., Boy, M., Laaksonen, A., and Lehtinen, K. E.: Atmospheric sulphuric acid and aerosol formation: Implications from atmospheric measurements for nucleation and early growth mechanisms, *Atmospheric Chemistry and Physics*, 6, 4079–4091, <https://doi.org/10.5194/acp-6-4079-2006>, 2006.
- Sipilä, M., Berndt, T., Petäjä, T., Brus, D., Vanhanen, J., Stratmann, F., Patokoski, J., Mauldin III, R. L., Hyvärinen, A.-P., Lihavainen, H., and Kulmala, M.: The Role of Sulfuric Acid in Atmospheric Nucleation, *Science*, 327, 1243–1247, 2010.
- Slater, A. M.: The IUPAC aqueous and non-aqueous experimental pKa data repositories of organic acids and bases, *Journal of Computer-Aided Molecular Design*, 28, 1031–1034, <https://doi.org/10.1007/s10822-014-9764-9>, 2014.
- Smith, J. N., Moore, K. F., McMurry, P. H., and Eisele, F. L.: Atmospheric Measurements of Sub-20 nm Diameter Particle Chemical Composition by Thermal Desorption Chemical Ionization Mass Spectrometry, *Aerosol Science and Technology*, 38, 100–110, <https://doi.org/10.1080/02786820490249036>, 2004.
- Smith, J. N., Dunn, M. J., VanReken, T. M., Iida, K., Stolzenburg, M. R., McMurry, P. H., and Huey, L. G.: Chemical composition of atmospheric nanoparticles formed from nucleation in Tecamac, Mexico: Evidence for an important role for organic species in nanoparticle growth, *Geophysical Research Letters*, 35, L04 808, <https://doi.org/10.1029/2007GL032523>, 2008a.

- Smith, J. N., Dunn, M. J., VanReken, T. M., Iida, K., Stolzenburg, M. R., McMurry, P. H., and Huey, L. G.: Chemical composition of atmospheric nanoparticles formed from nucleation in Tecamac, Mexico: Evidence for an important role for organic species in nanoparticle growth, *Geophysical Research Letters*, 35, L04 808, <https://doi.org/10.1029/2007GL032523>, 2008b.
- Smith, J. N., Barsanti, K. C., Friedli, H. R., Ehn, M., Kulmala, M., Collins, D. R., Scheckman, J. H., Williams, B. J., and McMurry, P. H.: Observations of aminium salts in atmospheric nanoparticles and possible climatic implications, *Proceedings of the National Academy of Sciences*, 107, 6634–6639, <https://doi.org/10.1073/pnas.0912127107>, 2010a.
- Smith, J. N., Barsanti, K. C., Friedli, H. R., Ehn, M., Kulmala, M., Collins, D. R., Scheckman, J. H., Williams, B. J., and McMurry, P. H.: Observations of aminium salts in atmospheric nanoparticles and possible climatic implications, *Proceedings of the National Academy of Sciences*, 107, 6634–6639, <https://doi.org/10.1073/pnas.0912127107>, 2010b.
- Smith, J. N., Draper, D. C., Chee, S., Dam, M., Glicker, H., Myers, D., Thomas, A. E., Lawler, M. J., and Myllys, N.: Atmospheric clusters to nanoparticles: Recent progress and challenges in closing the gap in chemical composition, *Journal of Aerosol Science*, 153, 105 733, <https://doi.org/https://doi.org/10.1016/j.jaerosci.2020.105733>, 2021.
- Sorooshian, A., Padro, L. T., Nenes, A., Feingold, G., Mccomiskey, A., Hersey, S. P., Gates, H., Jonsson, H. H., Miller, S. D., Stephens, G. L., Flagan, R. C., and Seinfeld, J. H.: On the link between ocean biota emissions , aerosol , and maritime clouds : Airborne , ground , and satellite measurements off the coast of California, 23, 1–15, <https://doi.org/10.1029/2009GB003464>, 2009.
- Spracklen, D. V., Carslaw, K. S., Kulmala, M., Kerminen, V.-M., Sihto, S.-L., Riipinen, I., Merikanto, J., Mann, G. W., Chipperfield, M. P., Wiedensohler, A., Birmili, W., and Lihavainen, H.: Contribution of particle formation to global cloud condensation nuclei concentrations, *Geophysical Research Letters*, 35, L06 808, <https://doi.org/10.1029/2007GL033038>, 2008.
- Stangl, C. M., Johnston, M. V., and Accepted, J.: Aqueous Reaction of Dicarbonyls with Ammonia as a Potential Source of Organic Nitrogen in Airborne Nanoparticles, *Journal of Physical Chemistry A*, <https://doi.org/10.1021/acs.jpca.7b02464>, 2017.
- Stewart, J. J. P.: Optimization of parameters for semiempirical methods V: Modification of NDDO approximations and application to 70 elements, *Journal of Molecular Modeling*, 13, 1173–1213, <https://doi.org/10.1007/s00894-007-0233-4>, 2007.
- Stull, D. R.: Vapor Pressure of Pure Substances. *Organic and Inorganic Compounds, Industrial & Engineering Chemistry*, 39, 517–540, <https://doi.org/10.1021/ie50448a022>, 1947.
- Swift, E. and Hochanadel, H. P.: The Vapor Pressure of Trimethylamine from 0 to 40°, *Journal of the American Chemical Society*, 67, 880–881, <https://doi.org/10.1021/ja01221a508>, 1945.
- Temelso, B., Morrison, E. F., Speer, D. L., Cao, B. C., Appiah-Padi, N., Kim, G., and Shields, G. C.: Effect of Mixing Ammonia and Alkylamines on Sulfate Aerosol Formation, *J. Phys. Chem. A*, 122, 1612–1622, <https://doi.org/10.1021/acs.jpca.7b11236>, 2018.
- Trinkaus, H.: Theory of the nucleation of multicomponent precipitates, *Physical Review B*, 27, 7372–7378, <https://doi.org/10.1103/PhysRevB.27.7372>, 1983.

- Tröstl, J., Chuang, W. K., Gordon, H., Heinritzi, M., Yan, C., Molteni, U., Ahlm, L., Frege, C., Bianchi, F., Wagner, R., Simon, M., Lehtipalo, K., Williamson, C., Craven, J. S., Duplissy, J., Adamov, A., Almeida, J., Bernhammer, A.-K., Breitenlechner, M., Brilke, S., Dias, A., Ehrhart, S., Flagan, R. C., Franchin, A., Fuchs, C., Guida, R., Gysel, M., Hansel, A., Hoyle, C. R., Jokinen, T., Junninen, H., Kangasluoma, J., Keskinen, H., Kim, J., Krapf, M., Kürten, A., Laaksonen, A., Lawler, M., Leiminger, M., Mathot, S., Möhler, O., Nieminen, T., Onnela, A., Petäjä, T., Piel, F. M., Miettinen, P., Rissanen, M. P., Rondo, L., Sarnela, N., Schobesberger, S., Sengupta, K., Sipilä, M., Smith, J. N., Steiner, G., Tomè, A., Virtanen, A., Wagner, A. C., Weingartner, E., Wimmer, D., Winkler, P. M., Ye, P., Carslaw, K. S., Curtius, J., Dommen, J., Kirkby, J., Kulmala, M., Riipinen, I., Worsnop, D. R., Donahue, N. M., and Baltensperger, U.: The role of low-volatility organic compounds in initial particle growth in the atmosphere, *Nature*, 533, 527–531, <https://doi.org/10.1038/nature18271>, 2016.
- Turner, M. C., Krewski, D., Pope, C. A., Chen, Y., Gapstur, S. M., and Thun, M. J.: Long-term Ambient Fine Particulate Matter Air Pollution and Lung Cancer in a Large Cohort of Never-Smokers, <https://doi.org/10.1164/rccm.201106-1011OC>, 2008.
- Vehkamäki, H., Kulmala, M., Napari, I., Lehtinen, K. E., Timmreck, C., Noppel, M., and Laaksonen, A.: An improved parameterization for sulfuric acid-water nucleation rates for tropospheric and stratospheric conditions, *Journal of Geophysical Research Atmospheres*, 107, 3–1, <https://doi.org/10.1029/2002JD002184>, 2002.
- Voisin, D., Smith, J. N., Sakurai, H., McMurry, P. H., and Eisele, F. L.: Thermal Desorption Chemical Ionization Mass Spectrometer for Ultrafine Particle Chemical Composition, *Aerosol Science and Technology*, 37, 471–475, <https://doi.org/10.1080/02786820390125232>, 2003.
- Waller, S. E., Yang, Y., Castracane, E., Kreinbuhl, J. J., Nickson, K. A., and Johnson, C. J.: Electropray Ionization–Based Synthesis and Validation of Amine-Sulfuric Acid Clusters of Relevance to Atmospheric New Particle Formation, *Journal of the American Society for Mass Spectrometry*, 30, 2267–2277, <https://doi.org/10.1021/jasms.8b06260>, 2019.
- Wang, C. Y., Jiang, S., Liu, Y. R., Wen, H., Wang, Z. Q., Han, Y. J., Huang, T., and Huang, W.: Synergistic Effect of Ammonia and Methylamine on Nucleation in the Earth’s Atmosphere. A Theoretical Study, *Journal of Physical Chemistry A*, 122, 3470–3479, <https://doi.org/10.1021/acs.jpca.8b00681>, 2018.
- Wang, M., Kong, W., Marten, R., He, X.-C., Chen, D., Pfeifer, J., Heitto, A., Kontkanen, J., Dada, L., Kürten, A., Yli-Juuti, T., Manninen, H. E., Amanatidis, S., Amorim, A., Baalbaki, R., Baccarini, A., Bell, D. M., Bertozzi, B., Bräkling, S., Brilke, S., Murillo, L. C., Chiu, R., Chu, B., De Menezes, L.-P., Duplissy, J., Finkenzeller, H., Carracedo, L. G., Granzin, M., Guida, R., Hansel, A., Hofbauer, V., Krechmer, J., Lehtipalo, K., Lamkaddam, H., Lampimäki, M., Lee, C. P., Makhmutov, V., Marie, G., Mathot, S., Mauldin, R. L., Mentler, B., Müller, T., Onnela, A., Partoll, E., Petäjä, T., Philippov, M., Pospisilova, V., Ranjithkumar, A., Rissanen, M., Rörup, B., Scholz, W., Shen, J., Simon, M., Sipilä, M., Steiner, G., Stolzenburg, D., Tham, Y. J., Tomé, A., Wagner, A. C., Wang, D. S., Wang, Y., Weber, S. K., Winkler, P. M., Wlasits, P. J., Wu, Y., Xiao, M., Ye, Q., Zauner-Wieczorek, M., Zhou, X., Volkamer, R., Riipinen, I., Dommen, J., Curtius, J., Baltensperger, U., Kulmala, M., Worsnop, D. R., Kirkby, J., Seinfeld, J. H., El-Haddad, I., Flagan, R. C., and Donahue, N. M.: Rapid growth of new atmospheric particles by nitric acid and ammonia condensation, *Nature*, 581, 184–189, <https://doi.org/10.1038/s41586-020-2270-4>, 2020.

- Wang, S., Zordan, C. A., and Johnston, M. V.: Chemical characterization of individual, airborne sub-10-nm particles and molecules, *Analytical Chemistry*, 78, 1750–1754, <https://doi.org/10.1021/ac052243l>, 2006.
- Weber, R. J., McMurry, P. H., Eisele, F. L., and Tanner, D. J.: Measurement of Expected Nucleation Precursor Species and 3–500-nm Diameter Particles at Mauna Loa Observatory, Hawaii, *Journal of the Atmospheric Sciences*, 52, 2242–2257, [https://doi.org/10.1175/1520-0469\(1995\)052<2242:MOENPS>2.0.CO;2](https://doi.org/10.1175/1520-0469(1995)052<2242:MOENPS>2.0.CO;2), 1995.
- Weber, R. J., Marti, J. J., McMurry, P. H., Eisele, F. L., Tanner, D. J., and Jefferson, A.: Measured Atmospheric New Particle Formation Rates: Implications for Nucleation Mechanisms, *Chemical Engineering Communications*, 151, 53–64, <https://doi.org/10.1080/00986449608936541>, 1996.
- Weber, R. J., Marti, J. J., McMurry, P. H., Eisele, F. L., Tanner, D. J., and Jefferson, A.: Measurements of new particle formation and ultrafine particle growth rates at a clean continental site, *Journal of Geophysical Research: Atmospheres*, 102, 4375–4385, <https://doi.org/10.1029/96JD03656>, 1997.
- Weber, R. J., Chen, G., Davis, D. D., Mauldin, R. L., Tanner, D. J., Eisele, F. L., Clarke, A. D., Thornton, D. C., and Bandy, A. R.: Measurements of enhanced H₂SO₄ and 3–4 nm particles near a frontal cloud during the First Aerosol Characterization Experiment (ACE 1), *Journal of Geophysical Research Atmospheres*, 106, 24 107–24 117, <https://doi.org/10.1029/2000JD000109>, 2001.
- Westervelt, D. M., Pierce, J. R., Riipinen, I., Trivitayanurak, W., Hamed, A., Kulmala, M., Laaksonen, A., Decesari, S., and Adams, P. J.: Formation and growth of nucleated particles into cloud condensation nuclei: Model-measurement comparison, *Atmospheric Chemistry and Physics*, 13, 7645–7663, <https://doi.org/10.5194/acp-13-7645-2013>, 2013.
- Wexler, A. S. and Clegg, S. L.: Atmospheric aerosol models for systems including the ions H⁺, NH₄⁺, Na⁺, SO₄²⁻, NO₃⁻, Cl⁻, Br⁻ and H₂O., *Journal of Geophysical Research*, 107, 2002.
- Whitby, K. T.: The physical characteristics of sulfur aerosols, *Atmospheric Environment*, 12, 135–159, <https://doi.org/10.1016/j.atmosenv.2007.10.057>, 1978.
- Winkler, P. M., Ortega, J., Karl, T., Cappellin, L., Friedli, H. R., Barsanti, K., McMurry, P. H., and Smith, J. N.: Identification of the biogenic compounds responsible for size-dependent nanoparticle growth, *Geophysical Research Letters*, 39, <https://doi.org/10.1029/2012GL053253>, 2012.
- Wyslouzil, B. E., Seinfeld, J. H., Flagan, R. C., and Okuyama, K.: Binary nucleation in acid-water systems. I. Methanesulfonic acid-water, *The Journal of Chemical Physics*, 94, 6827–6841, <https://doi.org/10.1063/1.460261>, 1991.
- Xie, H.-B., Elm, J., Halonen, R., Myllys, N., Kurtén, T., Kulmala, M., and Vehkamäki, H.: Atmospheric Fate of Monoethanolamine: Enhancing New Particle Formation of Sulfuric Acid as an Important Removal Process, *Environ. Sci. Technol.*, 51, 8422–8431, <https://doi.org/10.1021/acs.est.7b02294>, 2017.
- Yang, Y., Waller, S. E., Kreinbühl, J. J., and Johnson, C. J.: Direct Link Between Structure and Hydration in Ammonium and Aminium Bisulfate Clusters Implicated in Atmospheric New Particle Formation, *The Journal of Physical Chemistry Letters*, 9, 5647–5652, <https://doi.org/10.1021/acs.jpcclett.8b02500>, 2018.

- Yu, F.: Effect of ammonia on new particle formation: A kinetic H₂SO₄-H₂O-NH₃ nucleation model constrained by laboratory measurements, *Journal of Geophysical Research Atmospheres*, 111, <https://doi.org/10.1029/2005JD005968>, 2006.
- Yu, H., McGraw, R., and Lee, S.-H.: Effects of Amines on Formation of Sub-3 nm Particles and Their Subsequent Growth, *Geophys. Res. Lett.*, 39, 2, 2012a.
- Yu, H., Dai, L., Zhao, Y., Kanawade, V. P., Tripathi, S. N., Ge, X., Chen, M., and Lee, S. H.: Laboratory observations of temperature and humidity dependencies of nucleation and growth rates of sub-3nm particles, *Journal of Geophysical Research*, 122, 1919–1929, <https://doi.org/10.1002/2016JD025619>, 2017.
- Yu, W., He, X., Vanommeslaeghe, K., and Jr., A. D. M.: Extension of the CHARMM General Force Field to Sulfonyl-Containing Compounds and Its Utility in Biomolecular Simulations, *J. Comput. Chem.*, 33, 2451–2468, 2012b.
- Zhang, J. and Dolg, M.: ABCluster: the artificial bee colony algorithm for cluster global optimization, *Physical Chemistry Chemical Physics*, 17, 24 173–24 181, <https://doi.org/10.1039/c5cp04060d>, 2015.
- Zhang, J. and Dolg, M.: Global optimization of clusters of rigid molecules using the artificial bee colony algorithm, *Physical Chemistry Chemical Physics*, 18, 3003–3010, <https://doi.org/10.1039/c5cp06313b>, 2016.
- Zhang, R., Khalizov, A., Wang, L., Hu, M., and Xu, W.: Nucleation and Growth of Nanoparticles in the Atmosphere, *Chemical Reviews*, 112, 1957–2011, <https://doi.org/10.1021/cr2001756>, 2012.
- Zollner, J. H., Glasoe, W. A., Panta, B., Carlson, K. K., McMurry, P. H., and Hanson, D. R.: Sulfuric acid nucleation: power dependencies, variation with relative humidity, and effect of bases, *Atmospheric Chemistry and Physics*, 12, 4399–4411, <https://doi.org/10.5194/acp-12-4399-2012>, 2012.

Appendix A

Chapter 2 Supporting Information

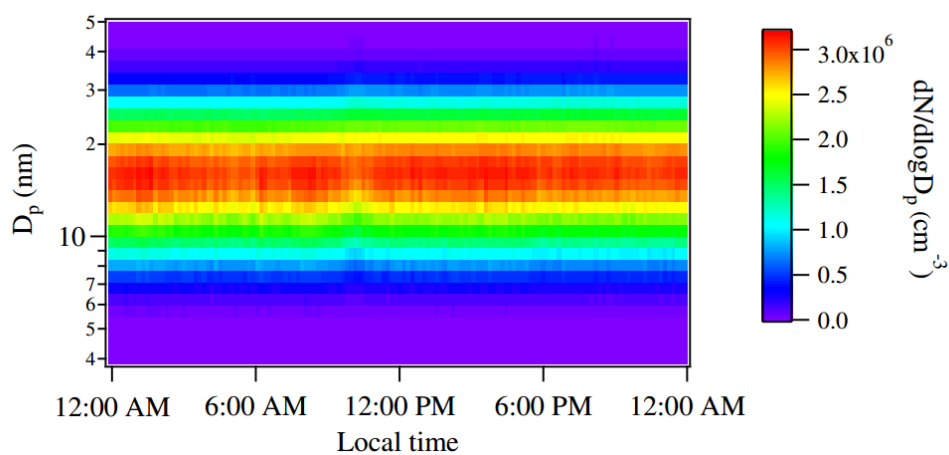


Figure A.1: Time evolution of size distributions of particles measured by SMPS from the reaction of $2.5 \times 10^{10} \text{ cm}^{-3} \text{ H}_2\text{SO}_4$ with $8.9 \times 10^{10} \text{ cm}^{-3} \text{ DMA}$ under dry conditions.

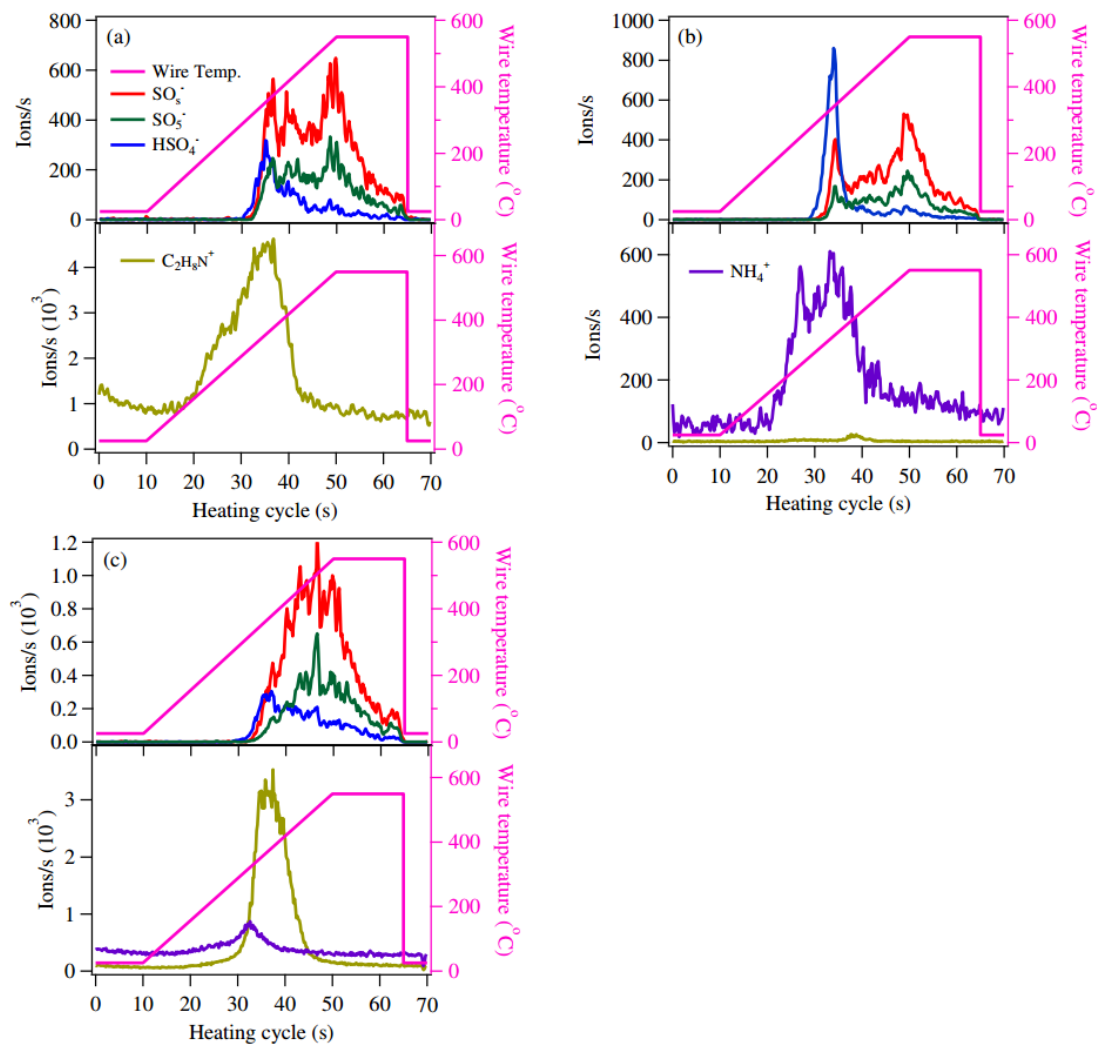


Figure A.2: Typical desorption profiles of ions formed by heating atomized particles of (a) $(\text{C}_2\text{H}_8\text{N})_2\text{SO}_4$, (b) $(\text{NH}_4)_2\text{SO}_4$ and (c) mixture of $(\text{C}_2\text{H}_8\text{N})_2\text{SO}_4$ and $(\text{NH}_4)_2\text{SO}_4$ in a 1:1 molar ratio collected on the Pt filament. The top panels show ions collected in the negative ion mode. The lower panels show ions collected in the positive ion mode. The magenta lines show the evolution of the filament temperature. The signal of $\text{C}_2\text{H}_8\text{N}^+$ is much higher than NH_4^+ in the lower panel of (c), suggesting that TDCIMS is more sensitive to $\text{C}_2\text{H}_8\text{N}^+$ ions.

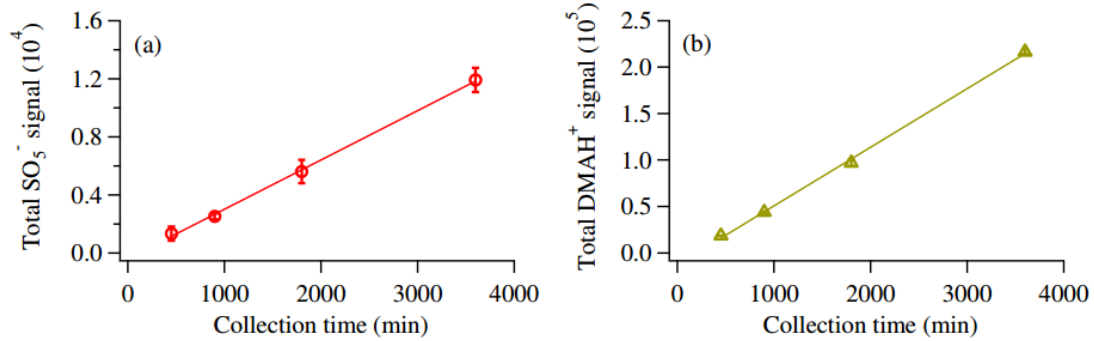


Figure A.3: Total (a) SO_5^- and (b) DMAH^+ signals as a function of collection time for H_2SO_4 -DMA particles. The error bars represent standard deviations of at least three repeated measurements.

Appendix B

Chapter 3 Supporting Information

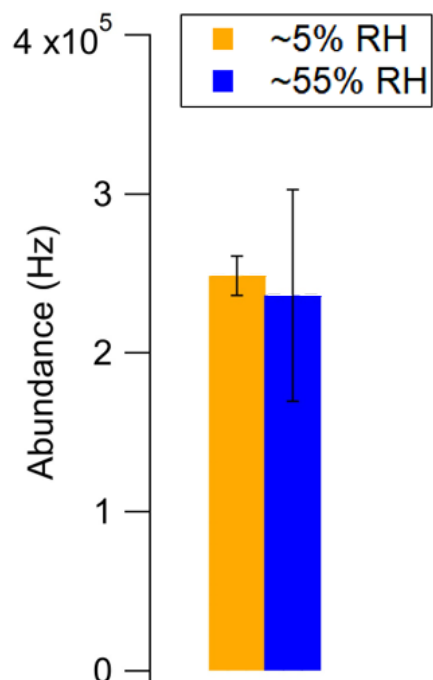


Figure B.1: Measured DMA abundance under 5% and 55% RH conditions using a transverse ionization chemical ionization inlet coupled with mass spectrometry (TI-CIMS) (Li et al., 2019). The reagent ion used for these experiments was H_3O^+ , and measured DMA abundances were within the linear range (that is, reagent ion was not saturated). No significant difference in DMA concentration was observed in the presence of water, which suggests that the different RH experiments did not operate under different vapor concentrations of DMA.

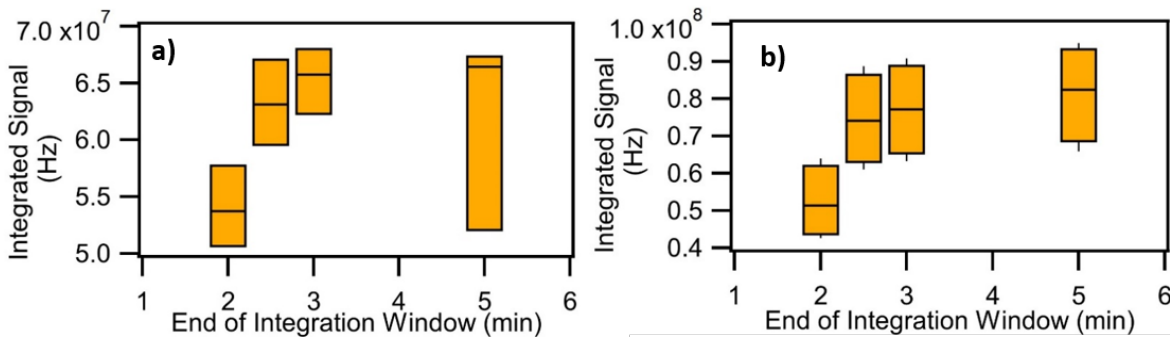


Figure B.2: Box-and-whisker plots of the difference in integration end times, where 5 minutes is across the entire desorption period. a) shows the effect on variability and average signal for nitrate ion, while b) shows the affect on variability and average signal on dimethylammonium ion.

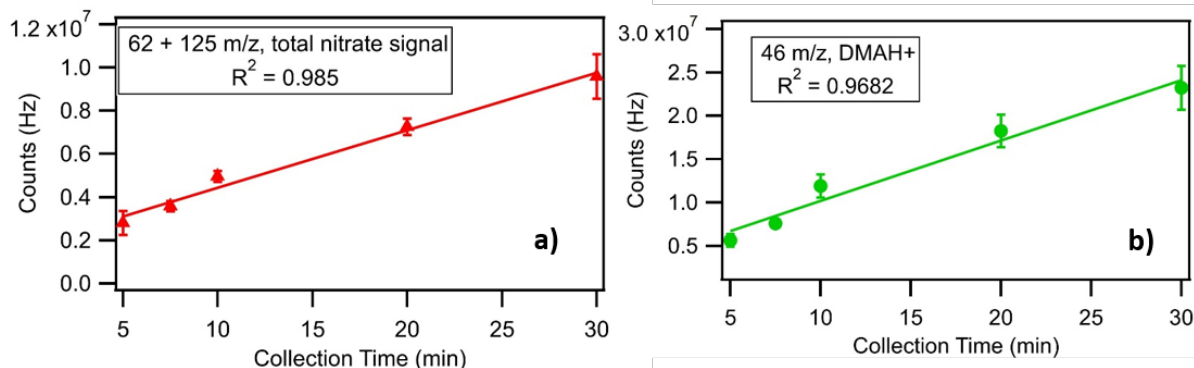


Figure B.3: Linearity tests of signal vs collection time for particles generated with dimethylamine and nitric acid in dry conditions, where a) shows the linearity of m/z 46 with collection time, and b) shows the linearity of total nitrate signal (m/z 62 and m/z 125).

B.1 Computational Methods

The Gibbs free binding energies for the global minimum energy clusters are calculated

$$\Delta G = G_{\text{cluster}} - \sum_i G_{\text{monomers},i}$$

The evaporation rates of the clusters are obtained from the Gibbs free binding energies ΔG of the evaporating cluster and its products as

$$\gamma_{(i+j) \rightarrow i,j} = \beta_{i,j} \frac{p_{\text{ref}}}{k_B T} \exp\left(\frac{\Delta G_{i+j} - \Delta G_i - \Delta G_j}{k_B T}\right).$$

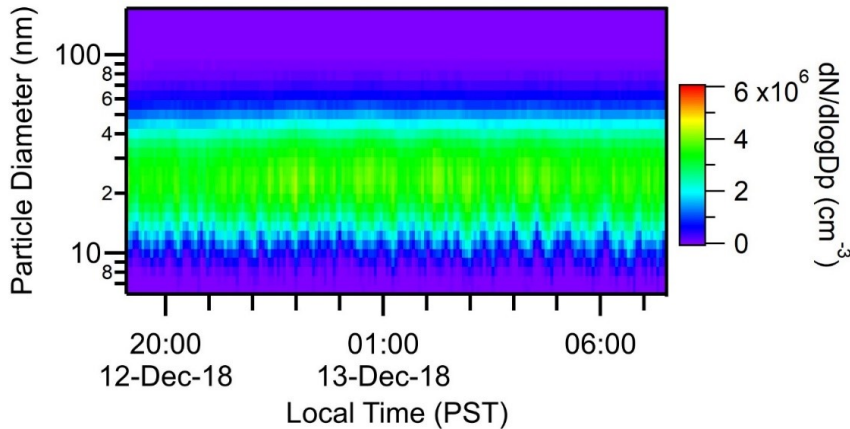


Figure B.4: Particle size distribution produced from dimethylamine and nitric acid in humid conditions over a period of 10 hours.

The collision coefficients for neutral-neutral collisions are computed from kinetic gas theory as

$$\beta_{i,j} = \left(\frac{3}{4\pi}\right)^{1/6} \left[6k_{\text{B}}T \left(\frac{1}{m_i} + \frac{1}{m_j}\right)\right]^{1/2} (V_i^{1/3} + V_j^{1/3})^2,$$

where m_i and V_i are the mass and volume of cluster i , respectively. The volumes are calculated using bulk liquid densities assuming spherical clusters and ideal mixing.

B.2 Hydrated Nitric Acid-Dimethylamine Clusters

We have calculated the evaporation rates for all studied acid-base clusters with 1–4 water molecules. Figure S5 shows that all evaporation rates are very high, which is related to the rapid evaporation of water monomers as discussed in the main text.

In order to prove that water has no contribution in the initial steps of new-particle formation, we have simulated the nanoparticle formation rates in dry and wet conditions using ACDC. We tested several different nitric acid and dimethylamine concentrations in order to detect even a small difference between RH=0% and RH=55% in particle formation rates. However, since water is so weakly-bound in nitric acid-dimethylamine clusters, particle formation is occurring via dry

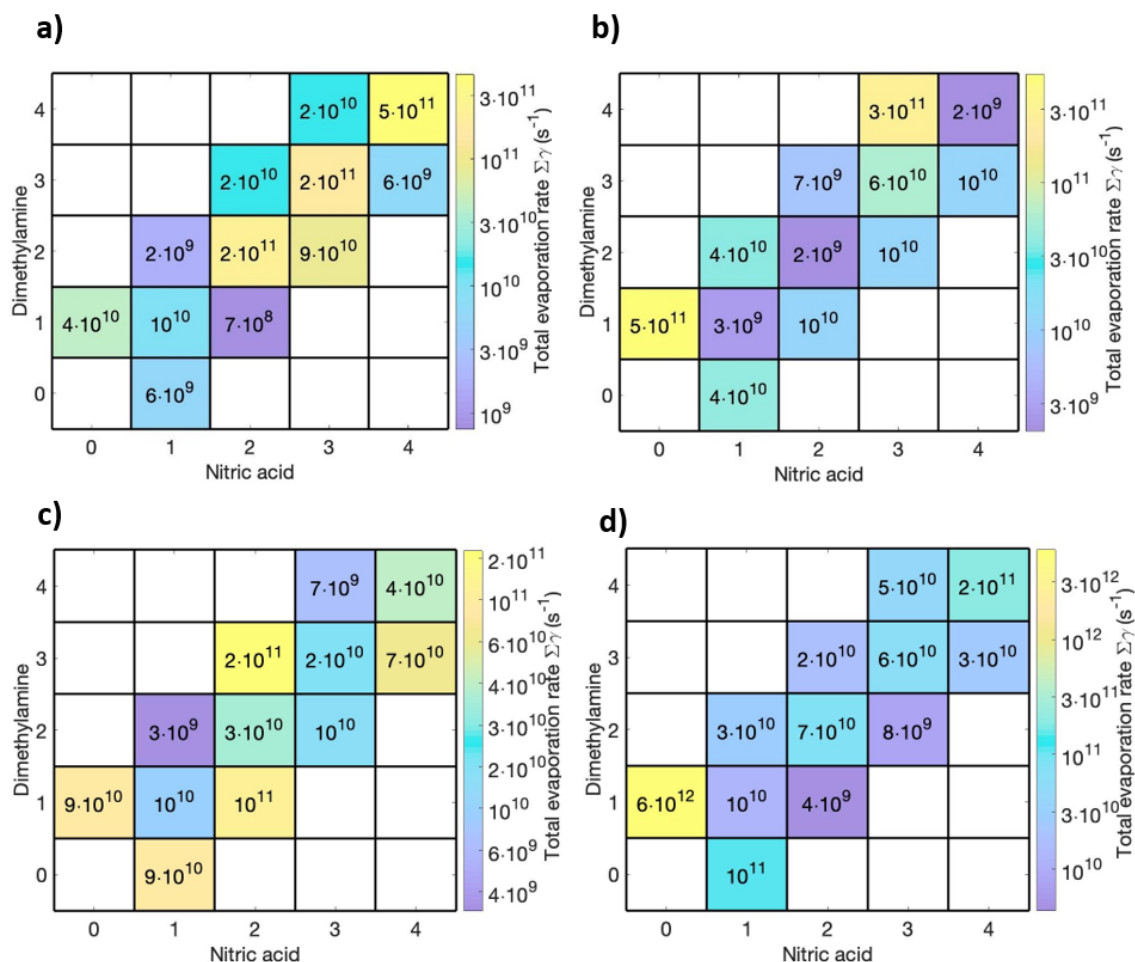


Figure B.5: Evaporation rates for nitric acid-dimethylamine clusters containing a) one water molecule, b) two water molecules, c) three water molecules and d) four water molecules.

pathway even at low concentrations and thus the presence of water does not increase the particle formation rate. Figure S5 shows that very low nitric acid and dimethylamine concentrations are required and that the effect of hydration is not negligible. When dimethylamine concentration is set as low as 0.001 pptV and nitric acid concentration is less than 10^6 cm^{-3} , the particle formation rate is increased at RH=55%. However, the particle formation rate is so small that it has no relevance in the atmosphere or even in laboratory measurements. Thus, we can conclude that due to the small number of available hydrogen bonds acceptors and donors in nitric acid-dimethylamine clusters and weak intermolecular interaction of water with nitric acid and dimethylamine, water is not contributing in the initial steps of particle formation. Therefore, we can assume that the

small increase in experimentally measured size-distribution is related to the uptake of water in large particles.

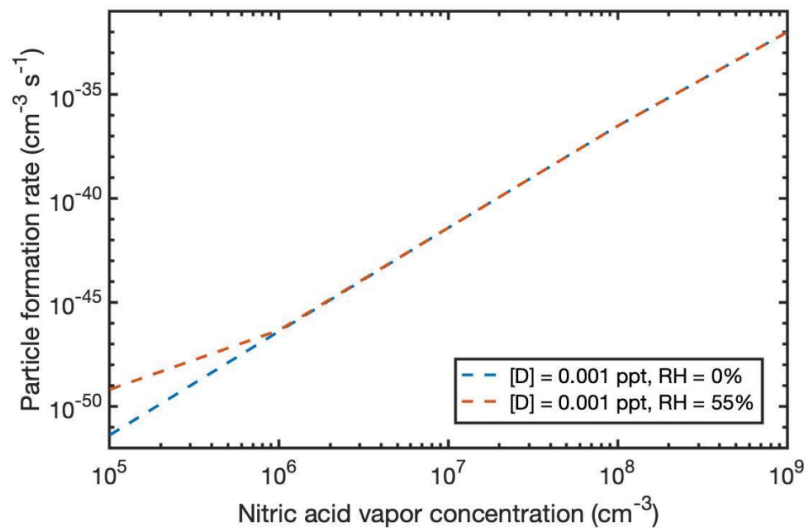


Figure B.6: Nanoparticle formation rate as a function of nitric acid concentration at dimethylamine concentration of 0.001 pptv at 298.15 K at RH=0% and RH=55%.

Table B.1: Calculated cluster Gibbs free binding energies in kcal/mol at 298.15 K.

Cluster	Gibbs energy	Cluster	Gibbs energy	Cluster	Gibbs energy
1NA1D	-5.7242	2NA1D4W	-12.275	4NA3D1W	-52.871
1NA2D	-6.7352	2NA2D1W	-26.098	4NA3D2W	-53.328
2NA1D	-10.444	2NA2D2W	-27.468	4NA3D3W	-52.762
2NA2D	-27.578	2NA2D3W	-27.175	4NA3D4W	-52.77
2NA3D	-28.86	2NA2D4W	-26.43	4NA4D1W	-67.816
3NA2D	-32.142	2NA3D1W	-29.077	4NA4D2W	-69.373
3NA3D	-47.425	2NA3D2W	-29.783	4NA4D3W	-69.135
3NA4D	-47.16	2NA3D3W	-28.589	4NA4D4W	-67.983
4NA3D	-52.065	2NA3D4W	-28.803	2W	3.16207
4NA4D	-69.522	3NA2D1W	-31.279	3W	4.86461
1NA1D1W	-5.9349	3NA2D2W	-31.68	4W	4.74604
1NA1D2W	-6.9573	3NA2D3W	-31.965	1NA1W	-0.3441
1NA1D3W	-7.2534	3NA2D4W	-32.585	1NA2W	0.42641
1NA1D4W	-7.432	3NA3D1W	-46.214	1NA3W	1.58792
1NA2D1W	-8.244	3NA3D2W	-45.677	1NA4W	2.77977
1NA2D2W	-7.8701	3NA3D3W	-45.948	1D1W	0.71937
1NA2D3W	-9.0972	3NA3D4W	-45.404	1D2W	2.89612
1NA2D4W	-8.949	3NA4D1W	-47.643	1D3W	3.87937
2NA1D1W	-12.27	3NA4D2W	-46.208	1D4W	7.28173
2NA1D2W	-12.493	3NA4D3W	-47.287		
2NA1D3W	-11.403	3NA4D4W	-46.893		

Appendix C

Chapter 4 Supporting Information

C.1 Monomer structures and properties

Molecular structures of each studied base compound are presented in Figure C.1. Ammonia, methylamine, dimethylamine and trimethylamine form a homologous series, where the substitution of H by CH_3 increases from zero for amm to three for tma. Thus, in a similar manner, the capability to form hydrogen bonding decreases from four for amm to one for tma. Trimethylamine oxide is an oxidation product of tma, in which an oxygen atom is attached to the nitrogen atom. Structurally tmao resembles tma with three methyl groups, an ability to form only one hydrogen bond and having a C_{3v} symmetry. However, their structures have a substantial differences due to the zwitterionic bond between N^+ and O^- , which cause an immense dipole moment of 5.2 D for tmao, whereas the dipole moment of tma is substantially lower at 0.7 D.

Guanidine has three functional groups: one imino group and two amino groups. When the imino group accepts a proton, there are three identical amino groups and these amino groups are not as basic as amines, since the imino group carbon already carries a positive charge, meaning that gua is very unlikely to accept more than one proton and it is not a triamine. Guanidine can form six hydrogen bonds and has a moderately high dipole moment of 3.0 D. Monoethanolamine, putrescine

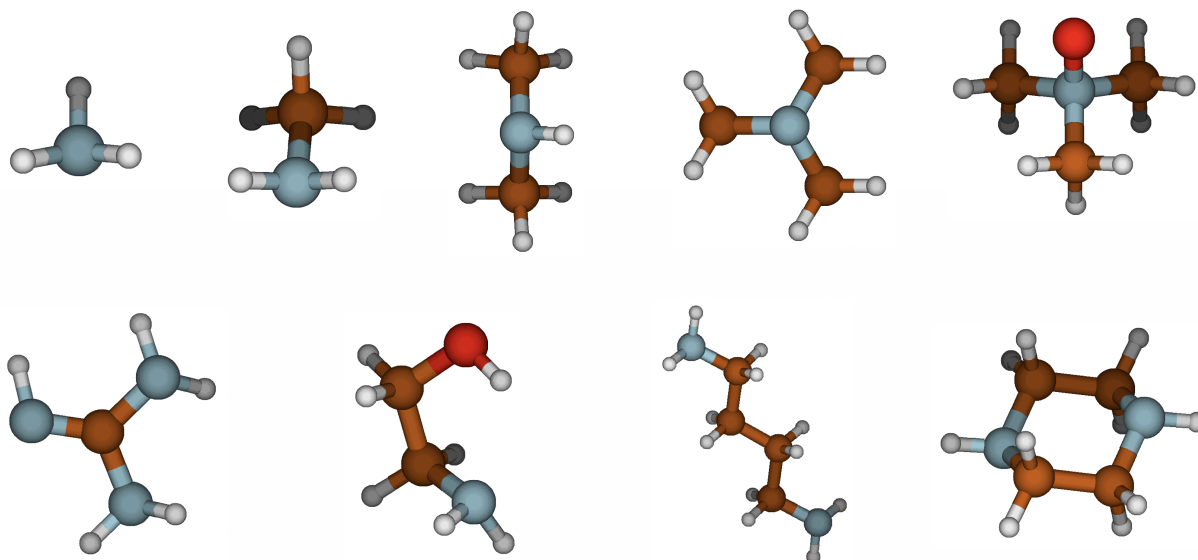


Figure C.1: Molecular structures of ammonia, methylamine, dimethylamine, trimethylamine, trimethylamine oxide, guanidine, monoethanolamine, putrescine and piperazine, respectively. Color coding: blue is nitrogen, brown is carbon, red is oxygen and white is hydrogen.

and piperazine have two functional groups: mea has one amino and one hydroxyl group, and put and pz have two amino groups. The alkanolamine, mea, has an increased ability to form H-bonds compared to monoamines due to the OH group. The primary amino group can form three H-bonds and the hydroxyl group increases the total number of hydrogen binding sites to five. The diamines, put and pz, have an ability to accept two protons. Putrescine has two primary amino groups, both of which can form three H-bonds, making the total number of H-bonds six. Piperazine is has two secondary amino groups in a six-membered ring structure in which both have two hydrogen binding sites and the total number of H-bonds is four. Both put and pz belong to point group of C_1 , and therefore, their dipole moment is 0 D. Table C.1 lists the dipole moments, polarizabilities, and point groups for monomeric structures. In addition, vapor pressures for the nine bases are listed in Table C.2 along with their corresponding sources.

Table C.1: Dipole moment, polarizability and point group for neutral and ionic structures.

BASE	Dipole D (neutral)	Dipole D (cation)	Polarizability \AA^3 (neutral)	Polarizability \AA^3 (cation)	Point group neutral	Point group cation
amm	1.8	0.0	1.6	1.1	C_{3v}	T_d
ma	1.5	2.3	3.3	2.7	C_s	C_{3v}
dma	1.1	1.6	5.2	4.3	C_s	C_2
tma	0.7	0.9	7.1	5.9	C_{3v}	C_{3v}
tmao	5.2	2.1	7.7	6.6	C_{3v}	C_s
gua	3	0.0	5.7	4.7	C_1	D_{3h}
mea	3.4	3.6	5.7	5.0	C_1	C_1
put	0	3.7	9.8	8.9	C_i	C_1
pz	0	4.0	9.3	8.3	C_i	C_s
ACID	neutral	anion	neutral	anion	neutral	anion
sa	3.3	2.7	4.9	5.6	C_2	C_s
msa	3.7	4.2	6.1	7.1	C_s	D_{3h}
na	2.6	0.0	3.4	4.1	C_1	C_{3v}

Table C.2: Literature vapor pressure values used in this study.

Base	Vapor Pressure (atm)	Reference
amm	9.8142303	Stull (1947)
ma	3.486597	Aston et al. (1937)
dma	2.044955	Aston et al. (1939)
tma	2.188	Swift and Hochanadel (1945)
tmao	7.41E-10	EPISUITE v. 4.11
gua	0.0028947	EPISUITE v. 4.11
mea	0.0003533	Matthews et al. (1950)
put	0.0031	EPISUITE v. 4.11
pz	0.00094	EPISUITE v. 4.11

We have performed the Gibbs free energy calculations by letting the monomer structures relax toward correct symmetry and making the frequency calculation for the optimized structure for which the quantum chemistry program has detected the point group shown in Table C.1. Approximately the same results can be reached by using initially C_1 symmetry for a system and making an *ad hoc* correction to the Gibbs free energy as suggested by Besel et al. (2020). An *ad hoc* correction to the free energy can be calculated as

$$C_{\text{symm}} = RT \ln \sigma_{\text{R}}, \tag{C.1}$$

where R is the gas constant, T is temperature and σ_{R} is the rotational symmetry number (which is less than or equal to the total symmetry number σ_{tot}).

Methanesulfonic acid and nitric acid complexes

Figure C.2 presents the molecular structures of msa-base and na-base heterodimers and their thermochemical parameters are listed in Table C.3.

Table C.3: Calculated enthalpy ($\Delta H_{\text{heterodimer}}$ in kcal/mol), entropy ($\Delta S_{\text{heterodimer}}$ in cal/(mol·K)) and Gibbs free energy ($\Delta G_{\text{heterodimer}}$ in kcal/mol) for msa-base and na-base heterodimer formation at 298 K.

heterodimer	$\Delta H_{\text{heterodimer}}$	$\Delta S_{\text{heterodimer}}$	$\Delta G_{\text{heterodimer}}$
1msalamm	-13.49	-30.84	-4.30
1msalma	-15.92	-28.72	-7.35
1msaldma	-19.29	-35.39	-8.74
1msaltma	-20.59	-35.40	-10.04
1msaltmao	-29.73	-36.88	-18.74
1msalgua	-26.55	-34.25	-16.34
1msalmea	-21.05	-43.02	-8.22
1msalput	-27.52	-46.82	-13.56
1msalpz	-20.37	-36.86	-9.38
1nalamm	-12.12	-28.29	-3.69
1nalma	-14.46	-33.49	-4.47
1naldma	-15.74	-33.51	-5.75
1naltma	-15.91	-33.99	-5.78
1naltmao	-23.68	-35.13	-13.21
1nalgua	-20.49	-32.69	-10.74
1nalmea	-14.05	-32.35	-4.41
1nalput	-19.63	-41.40	-7.29
1nalpz	-16.44	-34.03	-6.29

Acidity measures

As a measure for acidity in the gas phase, we have calculated the proton affinities (PA) and gas acidities (GA) for each studied compound. The gas-phase reaction can be written as



PA and GA are defined as the enthalpy and Gibbs free energy needed to extract a proton from the isolated gas-phase compound, respectively. That means the larger the PA and GA values are, the stronger the base is in the gas phase. For the bulk basicity, experimental $\text{p}K_{\text{a}}$ values are used (Haynes, 2014). A $\text{p}K_{\text{a}}$ value is a measure for the proton transfer ability when solvated by water, so it takes the solvation effect into account (Seybold and Shields, 2015). The larger the $\text{p}K_{\text{a}}$ value is, the stronger the base is in the aqueous phase. The aqueous-phase reaction can be written as



The Gibbs free energy for the proton transfer reaction in the aqueous phase can be calculated from the experimentally determined $\text{p}K_{\text{a}}$ value as

$$\Delta G_{\text{aq}} = \text{p}K_{\text{a}}RT \ln 10. \quad (\text{C.2})$$

Table C.4 shows different measures for acidities. As an alternative to Figure 4, the relationship between PA and $\Delta G_{\text{heterodimer}}$ has been shown in Figure C.3. In addition, the relationship between GA and $\Delta H_{\text{heterodimer}}$ is shown in Figure C.3.

Table C.4: Calculated proton affinity (PA) and gas acidity (GA), measured pK_a value from Haynes (2014) and aqueous-phase proton transfer free energy (ΔG_{aq}) and experimental PA and GA values from Hunter and Lias (1998). Values are given in kcal/mol at 298 K (when applicable).

Compound	PA (calc)	GA (calc)	pK_a	ΔG_{aq}	PA (exp)	GA (exp)
amm	203.7	195.5	9.3	12.6	204.02	195.75
ma	215.1	206.8	10.6	14.5	214.87	206.62
dma	222.6	214.6	10.7	14.6	222.16	214.27
tma	227.3	219.8	9.8	13.4	226.79	219.43
tmao	236.1	229.6	4.7	6.4	234.99	227.89
gua	236.0	227.6	13.6	18.6	235.73	226.91
mea	220.2	212.9	9.5	13.0	222.35	214.34
put	239.4	229.8	10.8	14.7	240.34	228.08
pz	226.9	219.3	9.7	13.2	225.55	218.62
sa	312.80	304.50	-3.0	-4.1	313.58	306.17
na	324.50	318.15	-1.4	-1.9	324.50	317.81
msa	319.98	313.92	-1.9	-2.6	320.98	315.01

Base dipole moment and polarizability

In addition to base vapor pressure exhibiting no correlation with $\Delta G_{heterodimer}$, dipole moment and polarizability also show no relationship with heterodimer stability, as shown in Figure C.4. Only sa salts are shown for clarity, as both neutral and cation forms of base polarizability and dipole moment are shown. Like vapor pressure, the only difference between the sa and na and msa salts would be a shift in $\Delta G_{heterodimer}$ for the same base polarizability or dipole moment values.

Boundary conditions in particle formation simulations

In NPF simulations, clusters are allowed to grow out of the 4acid4base simulation system as stable particles. The formed particle outside of a simulation box is expected to be stable in NPF simulations if it has larger or equal number of acid and base molecules than in following particles:

sa-amm: 5sa4amm

sa-ma: 5sa4ma

sa-dma: 5sa4dma

sa-tma: 5sa4tma

sa-tmao: 5sa3tmao and 4sa5tmao

sa-gua: 5sa4gua and 4sa5gua

sa-mea: 5sa3mea

sa-put: 5sa3put

sa-pz: 5sa3pz.

Simulated particle formation rates

Logarithm of the $J_{1.5}$ values for sulfuric acid–base systems with varying temperature and monomer concentrations are given in Table C.5.

Table C.5: Simulated $\log J_{1.5}$ values in $\text{cm}^{-3}\text{s}^{-1}$ for sa–base systems at varying temperature and monomer concentrations.

[A]=[B] (cm^{-3})	10^5	10^6	10^7	10^8	10^9	10^6	10^6	10^6	10^6
T (K)	298	298	298	298	298	248	273	323	348
amm	−40.0	−31.0	−22.0	−13.3	−5.0	−11.0	−20.9	−39.7	−47.1
ma	−25.1	−16.3	−8.0	−0.2	4.2	−5.1	−9.6	−24.6	−32.7
dma	−18.0	−9.1	−0.5	4.6	7.5	−0.4	−3.5	−18.1	−27.3
tma	−23.3	−15.3	−7.2	0.8	7.3	−0.9	−6.6	−23.8	−31.2
tmao	−9.7	−2.4	2.6	5.6	7.9	0.4	0.0	−6.2	−11.5
gua	−8.3	−0.5	3.6	5.8	7.9	−0.1	−0.2	−1.1	−4.7
mea	−21.0	−15.1	−6.5	0.5	5.6	−2.8	−6.8	−25.5	−34.6
put	−12.4	−4.5	2.6	5.8	7.9	0.5	0.0	−12.6	−20.4
pz	−16.1	−7.6	−0.2	4.6	7.4	−0.1	−2.9	−14.7	−23.1

The logarithm of the $J_{1.5}$ for sulfuric acid and ammonia or guanidine systems under all different conditions are given in Table C.6.

Table C.6: Simulated $\log J_{1.5}$ values in $\text{cm}^{-3}\text{s}^{-1}$ for sa-amm and sa-gua systems under all studied conditions.

amm	$\log J_{1.5}$	T (K)	$[A]=[B]$ (cm^{-3})	gua	$\log J_{1.5}$	T (K)	$[A]=[B]$ (cm^{-3})
	-19.8	248	10^5		-7.6	248	10^5
	-11.0	248	10^6		-0.1	248	10^6
	-3.1	248	10^7		3.7	248	10^7
	2.4	248	10^8		5.8	248	10^8
	5.9	248	10^9		7.9	248	10^9
	-29.9	273	10^5		-7.8	273	10^5
	-20.9	273	10^6		-0.2	273	10^6
	-12.3	273	10^7		3.7	273	10^7
	-4.2	273	10^8		5.8	273	10^8
	3.2	273	10^9		7.9	273	10^9
	-40.0	298	10^5		-8.3	298	10^5
	-31.0	298	10^6		-0.5	298	10^6
	-22.0	298	10^7		3.6	298	10^7
	-13.3	298	10^8		5.8	298	10^8
	-5.0	298	10^9		7.9	298	10^9
	-48.7	323	10^5		-9.1	323	10^5
	-39.7	323	10^6		-1.1	323	10^6
	-30.7	323	10^7		3.4	323	10^7
	-21.7	323	10^8		5.7	323	10^8
	-12.9	323	10^9		7.8	323	10^9
	-56.1	348	10^5		-13.3	348	10^5
	-47.1	348	10^6		-4.7	348	10^6
	-38.1	348	10^7		2.4	348	10^7
	-29.1	348	10^8		5.5	348	10^8
	-20.1	348	10^9		7.7	348	10^9

Hydrogen bonding in clusters

Hydrogen bonding rearrangement is shown in Figure C.5 to demonstrate why H-bonds in the heterodimer were counted as the number of polar hydrogens on the molecule, as they are able to break and re-form new H-bonds to take part in subsequent cluster growth. For example, although putrescine (blue box) participates in H-bonding with itself to stabilize the heterodimer (1put1sa), the second amine group breaks those bonds to participate in H-bonds with the second sulfuric acid molecule in the 1put2sa cluster.

Predictive expressions of $J_{1.5}$ for ammonia

The fit lines in Figures 10 and 12a all follow the form:

$$J_{1.5} = A + B * \exp\left(-\frac{\log x - Constant}{C}\right), \quad (C.3)$$

where x is defined as either $\log[\text{heterodimer}]$ or Φ , and A, B, C, and Constant are fit coefficients, of which all values are defined in Table C.7.

Table C.7: Equation coefficients used for the trend lines plotted on Figures 10 and 12a, following equation C.3.

x	Condition		Equation Coefficients			
	T (K)	[A] = [B] (cm^{-3})	A	B	C	Constant
$\log[\text{heterodimer}]$	248	10^5-10^9	18.614	-38.569	7.0896	-2.554
	273	10^5-10^9	119.81	-149.72	31.973	-3.729
	298	10^5-10^9	300.62	-340.65	73.629	-4.704
	323	10^5-10^9	1528.6	-1577.3	348.09	-5.525
	348	10^5-10^9	14125	-14181	3148.9	-6.226
	248-348	10^5	91.754	-148.03	12.911	-6.226
	248-348	10^6	91.707	-138.98	12.075	-4.226
	248-348	10^7	67.519	-105.82	9.0243	-2.226
	248-348	10^8	30.158	-59.575	4.7254	-0.226
	248-348	10^9	15.175	-35.76	2.5685	1.774
Φ	248-348	10^5-10^9	92.237	-148.48	12.947	-1.726

The 21 sa-amm CLOUD $J_{1.7}$ data points that were compared to our predicted results are shown in Table C.8, along with their respective experimental parameters and calculated $\Delta G_{\text{heterodimer}}$ values. Heterodimer concentration and Φ were calculated from this data for subsequent comparison to our model results.

Table C.8: CLOUD data of the sa-amm system taken from Kirkby et al. (2011), with experimental conditions outlined, as well as J values used. Concentrations are in units of molec cm^{-3} , and rates are in units of $\text{cm}^{-3} \text{ s}^{-1}$. $\Delta G_{\text{heterodimer}}$ values were calculated using Table C.3 and the temperature of the respective CLOUD experiment, and are in units of kcal/mol.

T (K)	[sa]	[amm]	Ionization rate	RH(%)	$J_{1.7}$	$\log J_{1.7}$	$\Delta G_{\text{heterodimer}}$
278.6	7.26E+08	7.64E+08	73.98	37.02	41.57	1.61878	-6.97364
278.6	7.48E+08	8.05E+08	3.24	37.01	3.36	0.526339	-6.96488
278.6	7.65E+08	8.69E+08	0	37	0.28	-0.55284	-6.96488
278.6	8.27E+08	1.29E+09	0	36.94	0.5	-0.30103	-6.97656
278.5	8.69E+08	9.84E+08	0	37.02	1.15	0.060698	-6.97364
278.5	3.86E+08	4.93E+08	3.63	37.37	0.06	-1.22185	-6.97656
278.3	4.42E+08	4.21E+08	2.4	38.37	0.65	-0.18709	-6.9678
278.3	8.55E+08	9.38E+08	2.01	37.56	3.52	0.546543	-6.96488
278.3	4.08E+08	3.34E+08	2.53	38.12	0.75	-0.12494	-7.84964
278.2	4.22E+08	4.59E+08	2.4	38.63	0.7	-0.1549	-6.97656
278.2	4.42E+08	4.98E+08	2.33	38.4	0.95	-0.02228	-7.84964
278.2	7.01E+08	5.95E+08	2.01	38.08	9.39	0.972666	-6.9678
278.2	4.28E+08	5.88E+08	2.27	37.97	1.05	0.021189	-6.97364
278.2	3.52E+08	5.91E+08	2.46	38.36	2.07	0.31597	-7.84964
278.2	4.45E+08	8.34E+08	2.53	38.07	1.03	0.012837	-7.84964
248.3	7.39E+07	6.57E+07	2.25	14.5	0.07	-1.1549	-6.97656
248.3	7.89E+07	6.57E+07	0	14.68	0.09	-1.04576	-7.84964
248.3	9.40E+07	1.22E+08	0	37.18	0.27	-0.56864	-6.96488
248.3	9.19E+07	1.22E+08	2.25	37.12	0.88	-0.05552	-6.97656
248.3	8.44E+07	6.59E+07	2.25	37.12	0.62	-0.20761	-6.97656
248.3	1.83E+08	1.22E+08	2.25	36.96	18.79	1.273927	-7.84964

Figure C.6 shows the accuracy of using either the temperature or concentration expressions to predict the experimentally measured CLOUD values. The expression used to predict CLOUD data was determined based on the conditions of the experiment (i.e., if the experiment was run at 278 K, the 273 K equation was used, or if the experiment was run at starting monomer concentrations approx. $10^8 \text{ molec cm}^{-3}$, the corresponding concentration equation was used). The use of monomer concentration expressions to predict J sees a larger spread in the predicted CLOUD $J_{1.7}$ rates:

within 4 orders of magnitude compared to the temperature expressions predicting within 2 orders of magnitude. This stands to reason since the concentration equations are separated by an order of magnitude, which has more effect on J than steps of 25 K in temperature.

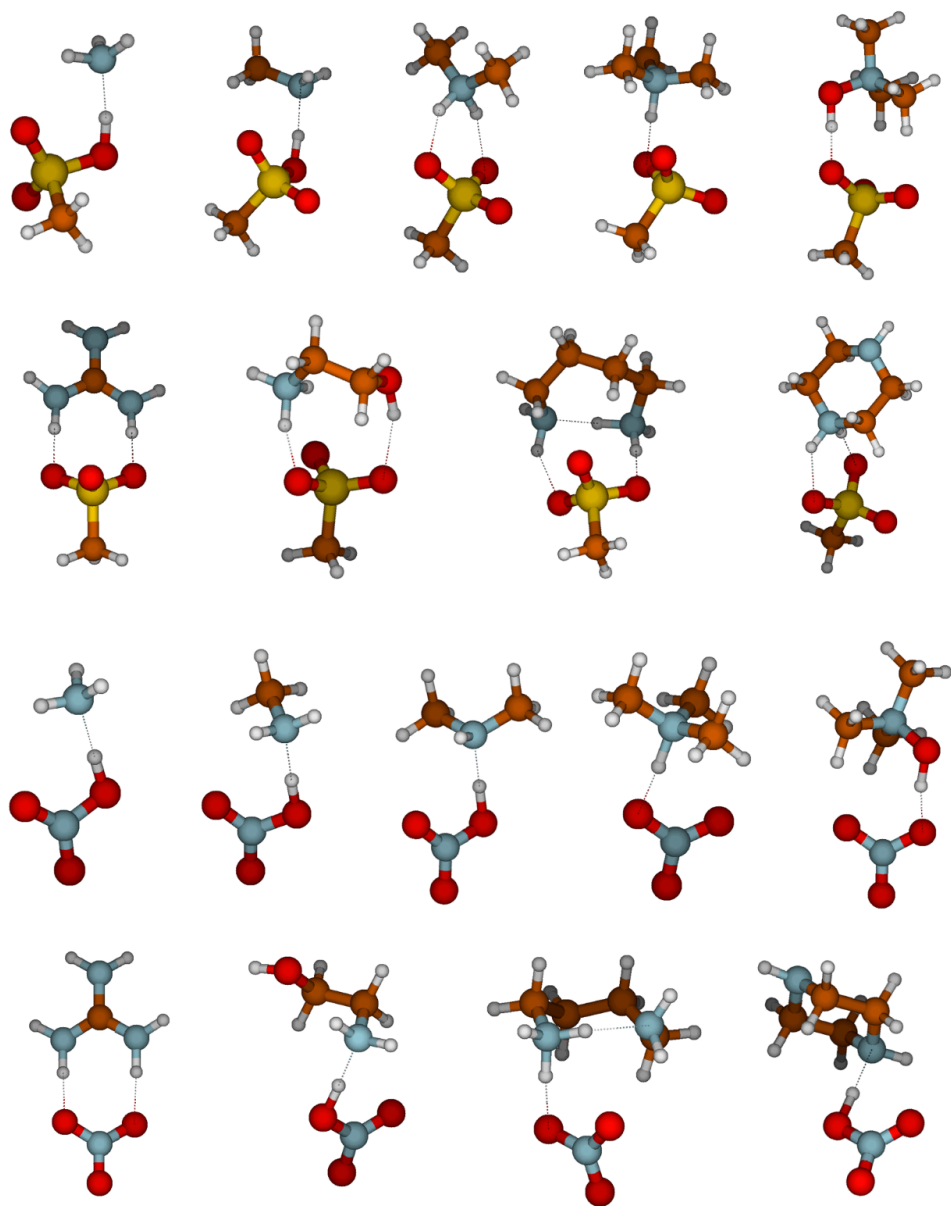


Figure C.2: Heterodimers of methanesulfonic acid (top) and nitric acid (bottom) with ammonia, methylamine, dimethylamine, trimethylamine, trimethylamine oxide, guanidine, monoethanolamine, putrescine and piperazine.

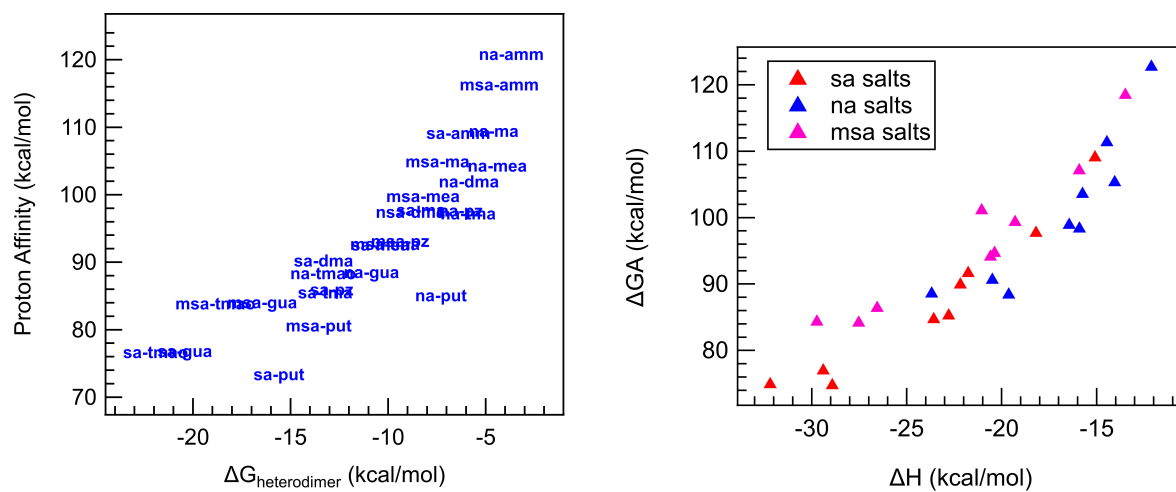


Figure C.3: ΔPA plotted against $\Delta G_{\text{heterodimer}}$ (left) and ΔGA plotted against $\Delta H_{\text{heterodimer}}$ (right).

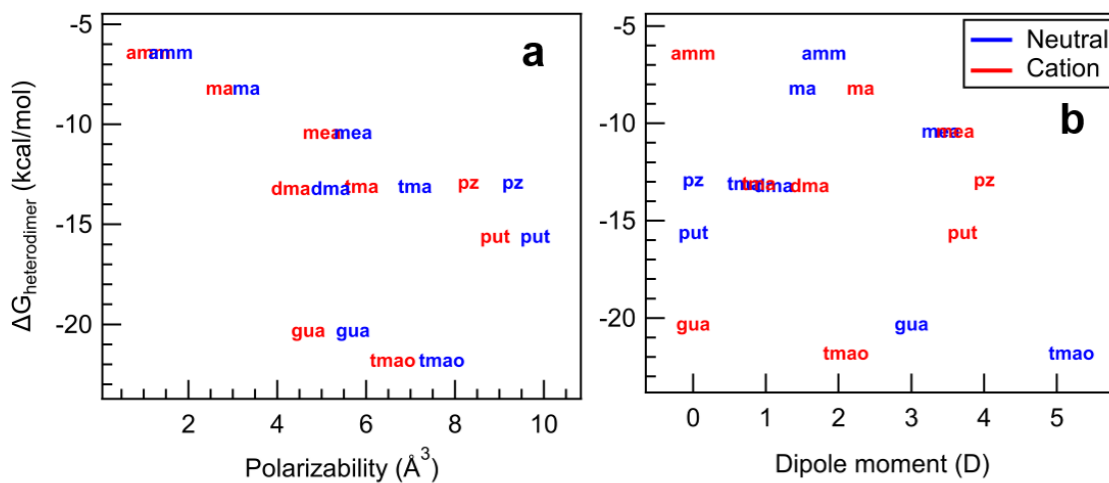


Figure C.4: $\Delta G_{\text{heterodimer}}$ for sa-base salts plotted against base a) polarizability and b) dipole moment. Lack of correlation is seen in both plots, as also observed for base vapor pressure.

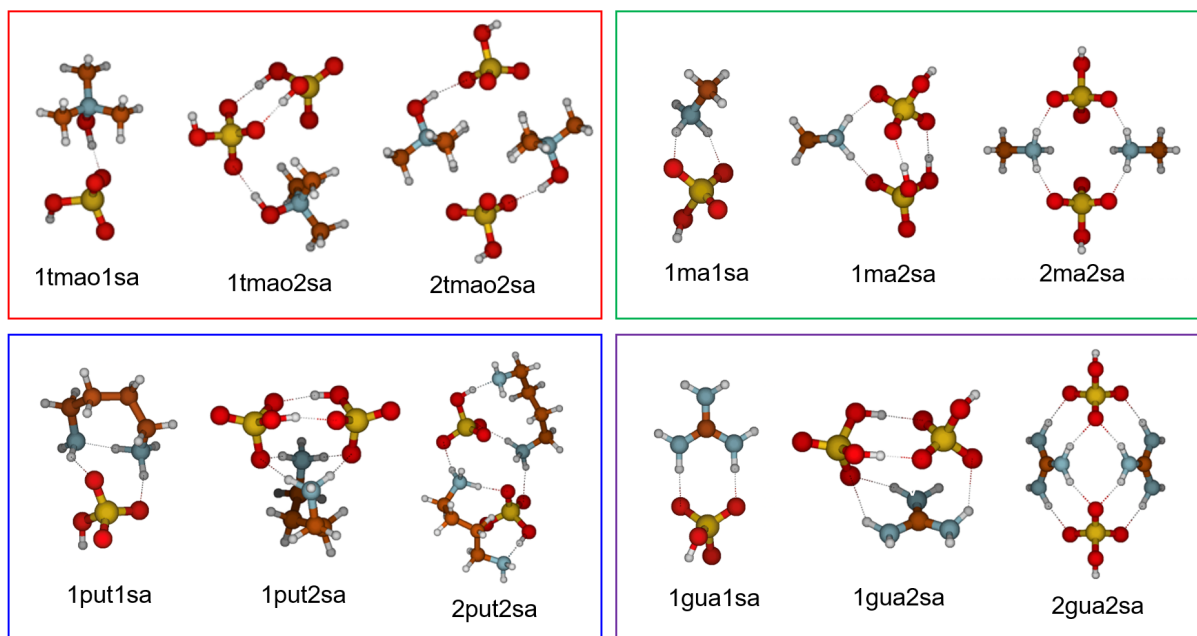


Figure C.5: Molecular structures showing the H-bond rearrangement in 1base1acid, 1base2acid and 2base2acid clusters. Note that putrescine is doubly protonated in 1put2sa.

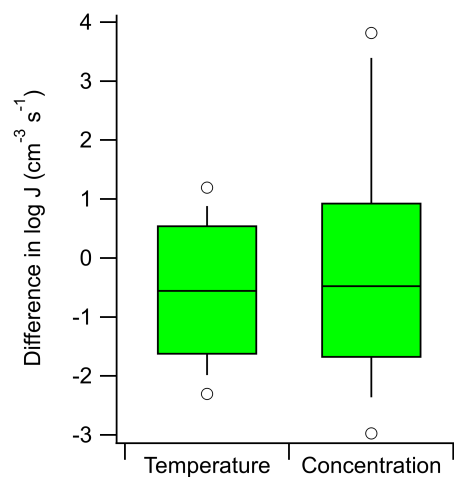


Figure C.6: Differences between predicted and experimentally measured CLOUD $J_{1.7}$ values using either the temperature or concentration trend lines in Figure 10. Difference was defined to be $J_{\text{predicted}} - J_{\text{experimental}}$, with the box showing 75th percentiles, whiskers showing 95th percentiles, and open circles showing outlier data points.